## ABSTRACT

MAJUMDAR, RUDRODIP. A Study of the Flow Patterns of Expanding Impurity Aerosol Following a Disruption Event in a Fusion Reactor (Under the direction of Dr. Mohamed A. Bourham and Dr. John G. Gilligan).

The current study focuses on the adiabatic expansion of aerosol impurity in the post-disruption and thermal quench scenario inside the vacuum chamber of a fusion reactor. A pulsed electrothermal plasma (ET) capillary source has been used as a source term simulating the surface ablation of the divertor or other interior critical components of a tokamak fusion reactor under hard disruption-like conditions. The capillary source generates particulates from wall evaporation by depositing transient radiant high heat flux onto the inner liner of the capillary. The particulates form a plasma jet moving towards the capillary exit at high speed and high pressure. The first chapter discusses briefly the relevance of the study pertaining to the impurities in a fusion reactor based on the work available in the form of published literature. The second chapter discusses briefly the operating principle of a pulsed electrothermal plasma source (PEPS), the virtual integration of PEPS with 1-D electrothermal plasma flow solver ETFLOW and the use of capillary plasma sources in various industrial applications. The third chapter discusses about primitive computational work, backed by the data from actual electrothermal source experiments from the in-house facility "PIPE" (Plasma Interactions with Propellants Experiment), that shows the supersonic bulk flow patterns for the temperature, density, pressure, bulk velocity and the flow Mach number of the impurity particulates as they get ejected as a high-pressure, high-temperature and hyper-velocity jet from the simulated source term. It also shows the uniform steady-state subsonic expansion of bulk aerosol inside the expansion chamber. The fourth chapter discusses scaling laws in 1-D for the aforesaid bulk plasma parameters for ranges of axial length traversed by the flow, so that one can retrieve the flow parameters at some preferred locations. The fifth chapter discusses the effect of temperature and the non–linearity of the adiabatic compressibility index on the supersonic flow patterns for ablated polycarbonate plasma, where the study shows significant changes in flow parameter values in the extreme limits of suggested non-linearities. The sixth chapter discusses the temperature-dependent flow patterns for high-density metal vapor plasmas, and the study brings out finer aspects like agglomeration and recombination in the dense bulk plasma as it undergoes isentropic

expansion. The last chapter presents analytical expressions for the 2-D steady-state spatial evolution of polycarbonate ablated plasma utilizing the 1-D scaling laws that were developed and discussed in the fourth chapter and the modeling is expected to enable us in predicting the spatial distribution of the debris from the plasma facing components (PFC) or the migrated dust in an efficient manner.

# A Study of the Flow Patterns of Expanding Impurity Aerosol Following a Disruption Event in a Fusion Reactor

by
Rudrodip Majumdar

A dissertation submitted to the Graduate Faculty of
North Carolina State University
in partial fulfillment of the
requirements for the Degree of
Doctor of Philosophy

Nuclear Engineering

Raleigh, North Carolina
2015

APPROVED BY:

| | |
|---|---|
| Dr. Mohamed A. Bourham<br>(Co- Chair) | Dr. John G. Gilligan<br>(Co- Chair) |
| Dr. K. Linga Murty<br>(member) | Dr. Alexei Saveliev<br>(member) |

# DEDICATION

To my mentors, my grandparents, my parents and my sister.

# BIOGRAPHY

Rudrodip Majumdar was born and brought up in the city of joy Kolkata in India. He was educated in various schools of West Bengal. He graduated in 2009 with a Bachelors of Technology in Electronics and Communication Engineering. After completing his undergraduate studies, Rudrodip pursued his graduate research work in Indian Institute of Technology Kanpur in the Nuclear Engineering and Technology Program and eventually obtained the Master of Technology degree in Nuclear Engineering in 2011 with extensive research experiences in computational plasma physics and fusion plasmas. After the completion of his M.Tech. in June of 2011, Rudrodip began his doctoral research work in North Carolina State University, on the study of supersonic flow patterns of expanding impurity aerosol following the current quench and surface disruption event in a real-life fusion reactor. He is expected to graduate in the Fall Semester of 2015.

# ACKNOWLEDGMENTS

A doctoral research life, in my esteem is not only a phase of academic growth, but is also of a total personal growth. I am very lucky that I got the opportunity to work closely under the mentorship of two wonderful professors of the Nuclear Engineering department at North Carolina State University. I would like to express my deepest gratitude to my advisors, Dr. Mohamed A. Bourham and Dr. John G. Gilligan, for their extreme patience, excellent guidance and providing me with an excellent atmosphere where I could work with almost an absolute independence knowing that two pairs of eyes were always keenly monitoring my progress. Both of them made sure that my confidence always remained high.

I would like to pay my sincere and warm thanks to my committee member and the director of the graduate program in nuclear engineering, Dr. K.L. Murty for his continuous backing and encouragement. Personal interactions with him have always touched my heart and have kept me motivated.

I would like to pay sincere thanks to my Ph.D. committee member Dr. A. Saveliev for his support and invaluable comments and inputs from time to time. I would like to thank Dr. John Mattingly, Dr. Steve Shannon and Dr. Dmitri Anistratov for all the advices and help they have extended to me during the coursework.

Amongst all the busy schedules, I was fortunate enough to be able to forge some really memorable friendships. Moments spent with Tirtha, Debraj, Sabrina, Saswata, Rajarshi, Anand and Nouf will be fondly remembered and cherished. Thanks to all the seniors, contemporaries and juniors who stood by me through thick and thin.

I am grateful to my good old friend Pallav, close friend Subhashis da, Swarnali di, Shibaji da and Tapasi di for giving me uplifting pep-talks from time to time.

I will remain always indebted my mentor, friend, philosopher and guide Dr. M.S. Kalra and I am specially thankful to Dr. Prabhat Munshi and Dr. Om Pal Singh for all the advices they have provided me with.

I am grateful to a large extent to the Indian musical geniuses Pt. Shri Bhimsen Joshi, Pt. Shri Shiv Kumar Sharma, Shri Kishore Kumar Ganguly and Shri Rahul Dev Burman for inspiring me through their sheer creativity and quality of work.

I am grateful to my grandparents for providing me with wonderful parents.

If I have ever achieved anything in my life that is because of the sacrifices my parents made for me. Thanking them would be actually an act of belittling them. I am and will remain indebted to them all through my life. My existence at all the levels is owed to them.

My best and closest friend, my sister is the source of all the joy in my life. Life would not have been complete without an awesome sibling like her. There is no point in thanking her formally, she is a part of my soul and will remain so.

I am grateful to my first teacher Smt. Bharati Banerjee and my Guru Shri R.N. Neogi, because they gave me the confidence for the first time in my life that I have the ability to rise above the average.

Finally, I would like to thank Almighty for providing me with strength, stamina, sound health and will power.

## TABLE OF CONTENTS

## List of Tables

## List of Figures

# 1

# Introduction

One of the major problems in future large Tokamak fusion reactors is the particle and energy transport near the vacuum vessel edge and the formation and expansion of aerosol following hard disruption events.. Cross-field fluxes that originate in the region of confined plasma carry outwards significant amounts of energy, thus featuring very high risk of damaging the first wall, divertor target armors, limiter and other Plasma Facing Components (PFCs), some of which can be Carbon Fiber Components (CFCs). The inner and outer divertor targets are the most highly loaded components of ITER machine. In present-day machines of the size of JET, TFTR and JT-60U, disruptions are more than a nuisance and they are potent enough to cause serious damages. Forces of the order of $2MN/m^2$ have caused deformation of structures, melting and erosion of PFCs and short circuits in external supplies **[1, 2].** The situation may worsen in the bigger fusion devices like ITER, where a hard disruption event may impart a high heat flux of the order of 50-60 $GW/m^2$ or higher on the Tokamak first wall, divertor and other PFCs resulting in a large amount of impurity aerosol being produced and transmitted through the boundary region. The fusion rate may decrease considerably due to dilution of the fuel by the presence of the impurities. Moreover, the density of impurities relate to the effective ion charge ($Z_{eff}$) which has been found to greatly influence ion and electron transport. Thus accurate characterization of the impurities in the Tokamak plasma is although very complex, yet an important task.

## 1.1 Generation of dust particles in fusion reactors

The impurities, i.e. the carbon and metal dust particles are generated by a number of processes, such as desorption, arcing, sputtering, evaporation and sublimation of thermally-loaded wall material. From the experiments it has been verified that in case of Carbon Fiber Components or graphite wall components, in addition to the C atoms, a significant amount of carbon clusters are liberated. The other mechanisms for the formation of impurities are the spallation and flaking of thin films of redeposited material or of films which were grown

intentionally for wall-conditioning purposes. The films from wall-conditioning having a thickness of few 100 nm are the potential source of thin flakes. The redeposited layers from Tokamak operation may have thicknesses up to several 100μm. They may have a stratified structure due to superposition of consecutive discharge events. The layers tend to be mechanically unstable for thicknesses exceeding a few μm and become prone to spallation.

When considering a fusion reactor with D-T (1:1) fuel, additional processes such as formation of Helium-3 due to decay of tritium (T), formation of Helium-4 due to neutron induced spallation reactions of low- Z wall material, the ejection of dust particles due to alpha particle induced embrittlement of the near-surface region etc. may become very important in producing the hazardous dust particles [3].

### 1.2 Survey of dust formed in experimental test Tokamaks

Dust is an integral part of plasmas especially those residing in the confinement of man-made devices. Dust is composed of a range of elements depending on the environment, and it may well be hydrocarbons and tungsten compounds in Tokamaks. In the fusion context the term 'dust' denotes all erosion products resulting from plasma–wall interaction processes and covers a range of particle dimensions from a few nanometers to millimeters. As dust in plasma is usually charged, its presence in large quantities will significantly alter the plasma parameters by localizing large amounts of charge in the dust grain volume. Dust in Tokamaks probably has the least information documented and published. This is probably due to the fact that analysis of the plasma facing components is only possible when the Tokamak has not been operated for a while. Dust was collected from JET's MkIIa divertor approximately 2000 shots after its installation [4]. The divertor materials were Inconel and CFC, with the main chamber also containing beryllium. Loose dust was collected by a cyclone vacuum cleaner, the finer particles wiped of the plates afterwards with a cloth. The median diameter of these particles was 27 μm. Flakes of redeposited material were also collected from areas shielded from the plasma flux. The amount of loose dust collected was too little to support a meaningful analysis, but the cloth samples and flakes showed that the majority of material present was carbon. The smears were 97% carbon, 1% beryllium and 2% metals by weight. The samples were radioactive, containing tritium and 7Be. The flakes

contained 99% carbon and 0.5% beryllium, rest being the traces of the metals. A significant amount of tritium was also found, with most being in the flakes. Approximately 3-3.3 mg of tritium was found per gram of flakes. This highlights the fact that tritium retention in dust and flakes is a serious problem for a fusion reactor [18].

Dust formation in carbon-wall machines (e.g. TEXTOR) is mainly related to sputtering and chemical erosion of carbon by fuel species followed by long-range migration and re-deposition of hydrogenated carbonaceous species (CxHyDz) in the form of co-deposited layers on plasma-facing components (PFC) [5-7] and is in remote areas with no direct line-of-sight to the plasma [8]. Such layers often flake and peel-off from the substrate, thus forming dust agglomerates [5-7, 9-10]. There is no critical layer thickness when such a process starts. Dust release also occurs due to arcing; the effect has frequently been observed during the start-up phase [6]. Another mechanism of carbon dust production may be related to brittle destruction of carbon under localized high power loads [10, 11]. Melting, melt layer motion and eventually splashing of droplets would be the main mechanism for the formation of metal dust [10, 12- 13]. The formation and accumulation of dust may have a serious impact on the economy and safety in operation of a reactor-class device [5, 14–17]. The primary concern is related to consequences of oxygen and/or water contact with hot dust in the case of air and/or water leak during the plasma operation giving a high risk of pressure rise and explosion. A water leak or presence of moisture would lead to the gasification of carbon by the water–gas shift reaction (H2 and CO as products) and, in the case of metal dust, hydrogen release, e.g. $Be + H_2O \rightarrow BeO + H_2$. A risk of mobilization and release of radioactively contaminated (neutron-activated and tritiated) products by explosion is also taken into account in fusion safety assessments.

### 1.3 Comparison of main chamber erosion with dust collected in the divertor in experimental reactor chamber

The divertor was installed inside JET chamber way back in 1994, and since then it has been operated as an all carbon machine. In JET all the surfaces with direct interaction with the confined plasma were made from carbon, either as graphite or latterly carbon fiber composite (CFC). Just over half of the vessel was covered in carbon tiles and the remaining

uncovered area was the Inconel vacuum vessel. In 2010 JET was converted to an all metal device such that all surfaces interacting with the plasma are now beryllium and tungsten. This new configuration is known as the ITER-like Wall (ILW) since it is designed to demonstrate the differences in transport and hydrogen isotope retention between the two scenarios and to help predict the behaviors of ITER in these important aspects. In order to complete the transition from an all carbon to all metal wall all CFC tiles were removed and replaced with Be, Be-coated Inconel or tungsten coated CFC tiles in the main chamber and tungsten-coated CFC with one row of solid W tiles in the divertor. As with other JET interventions a set of tiles removed from the vessel have been made available for analysis. The complete refurbishment also provided a unique opportunity to collect dust and flakes found in the divertor as all the divertor carriers were removed from the vessel. Profiler measurements and cross section microscopy on tiles that were removed in the 2009 were used to evaluate the net erosion in the main chamber and net deposition in the divertor. In addition the mass of dust and flakes collected from the JET divertor during the same intervention is also reported and included as part of the global balance for carbon in JET. It should be noted that although a strong interaction between the limiters and the plasma during the limiter phase is expected the total amount of erosion attributed to the limiter phase (i.e. assumed to equal the net deposition on the limiters) is only 20 - 30% of the total erosion found on the limiters for the entire operating period (i.e. limiter and X-point phases). In order to determine the main chamber carbon source during the X-point phase from the spectroscopy signal the whole plasma area of 139 m2 was used, giving ~2000 g of eroded carbon. During the X-point phase this mass of carbon migrated from the main chamber into the divertor. This migrating mass of carbon is a factor of 2-3 times higher than the net deposition observed in the divertor and the mass of dust/flakes collected was 533 g and 300 g, respectively [18,19].

## 1.4 Studies of the Erosion and Deposition of Wall Material

Investigations were made with the Axially Symmetric Divertor Experiment Upgrade (ASDEX-Upgrade), a medium-sized Tokamak at IPP in Garching, Germany, which was equipped with tungsten divertor plates. For an experiment running for about 800 shots, the main chamber components showed a constant low tungsten contamination level. Peak values of tungsten re-deposition, up to 40 times larger than in the main chamber, occurred in the divertor. The positions of the maximum re-deposition coincide well with the overall peak values of deuterium flow for the whole experimental campaign. By comparison, the amounts of Fe, from steel components, and Cu redeposited in the same region were more than an order of magnitude higher. Surface analysis of the tungsten plates revealed only a 2% to 25% concentration of tungsten, with large amounts of boron, carbon and oxygen present. This is a result of various chemical reactions between components, the plasma, and the air in which the components are stored. Up to 60% of the deuterium inventory was found in the divertor, thought to be co-deposited with the low-Z material.

In another investigation, the JET mark I divertor was analyzed after around 3500 shots. It was constructed of carbon tiles, with the vessel walls being made of Inconel 600 (75% Ni, 15.5% Cr, 8% Fe) conditioned with beryllium, and limiters made of CFC. A typical JET shot starts with circular plasma controlled by limiters for around 10 s, followed by 10-15 s in a divertor configuration, and finally back to the limiter configuration before switching off. For analysis, sections of tiles in each area of the Tokamak were cut. Considerable erosion of metals from the inner wall and beryllium from the outer wall were measured, as well as carbon from the limiters. Re-deposition of carbon was significant in all areas apart from the inner wall whereas much less re-deposition was observed for beryllium and metals in these areas [18].

In a recent effort made at North Carolina State University, the experimental electrothermal launcher devices SIRENS and PIPE have been investigated by NC State University team with a view to measuring the erosion of material surfaces subjected to high-heat flux from a high-density, low-temperature plasma (1-3 eV) with a strong applied magnetic field. High-heat flux erosion studies have been performed on Lexan, graphite, copper, brass, stainless steel, and aluminum samples. Initial analysis of the samples indicates

strong axial erosion dependence for metallic surfaces as opposed to uniform ablation for insulators [20-23]. Surface conditioning through multiple exposures to repetitive discharges showed a decrease in the rate of ablation for a Lexan insulator and an increasing erosion rate for metallic surfaces [23].

### 1.5 Role of impurities in triggering disruption events

Large particles falling into fusion plasma can induce a disruption. Narihara et al studied the influence of the small carbon particles with diameters less than 2 μm, on the performance of Tokamak discharges using Thomson scattering set up in JIIP-2U. The dusts were dropped from the top of the machine and the investigators found that an amount of impurity containing about 106 particles of 2 μm diameter do not affect fully developed discharges, but such impurities existing in the main volume before start-up of the plasma lead to increased impurity concentrations. The intense impurity radiation often observed during the start-up phase of Tokamak plasmas may be due to levitated dust. Dust particles work as a sink for the electrons. For large concentrations of dust particles, a serious change in balance may take place between the electrons and the fuel ions in the edge plasmas. This may result in a different sheath potential and heat transmission factor, and in a different dynamics of the edge plasma [24]. Thus it is very important to track the bulk flow of the ablated mass that forms the impurity aerosol, as the bulk enters the core plasma. In the current work supersonic flow patterns of the impurity particulates generated due to possible disruption events in magnetic fusion devices have been conceptualized and the evolution of the impurity jet has been modelled assuming azimuthal symmetry, i.e. no particular directional flow bias. Adequate insight has been given to some of the bulk flow parameters like plasma bulk temperature, density, pressure and velocity. The changes in Mach number of the bulk flow has also been tracked, with a view to defining the flow regimes and this is important because the steady state impurity flow properties of a fully developed discharge is indeed dependent on the bulk flow parameters.

## 1.6 Electrothermal plasma source as disruption simulator

In the current research work a pulsed electrothermal plasma source operating in controlled-arc regime has been used as the simulated source of impurity, where the melting and removal of the material from the wall of the ablative capillary and subsequent decomposition and ionization of the ablated bulk leads to the generation of a test impurity plasma jet that opens up into a large vacuum chamber [21]. All the disruption affected locations of a large fusion reactor chamber have been conceptually lumped into the capillary plasma source. Pulsed electrothermal plasma sources being operated by a burst of current pulse having a width of few hundred microseconds on the time axis enable us to have a good approximation of the instantaneous disruption events in the fusion reactor chamber [21-23]. High particulate density, high pressure, high jet velocity and moderately high jet temperature at the capillary exit makes the PEPS a very good simulator for the impurity aerosol that expands into the reactor vessel following a fusion disruption event [22].

The design –oriented conceptual similarity between the affected PFCs opening into the fusion chamber and a PEPS being added to a cylindrical vacuum vessel as the source of test impurities has been shown here in Figures 1.1 and 1.2.

As the radiant heat flux deposited on the plasma facing components is considerably high, thus there is some possibility that a fraction of the impurity bulk flowing coming out the of vessel wall of the fusion reactor would be at the sonic speed. Thus they would expand supersonically for a brief time until they reach the maximum radial stretch. Capillary Plasma Sources generally offer a subsonic condition at the capillary exit. Thus to facilitate the supersonic flow a virtual converging-diverging nozzle has been introduced at the capillary exit, which opens into a large chamber. It has been assumed that the large chamber back pressure (PB) or in other words, the ambient pressure in the large space is low enough to provide supersonic acceleration to the evolving ablated mass. PB is less than the pressure at sonic throat (P*) so that the flow is accelerated supersonically till the diverging exit and over-expanded flow enters the large chamber, but PB is sufficiently greater than the diverging exit pressure (PDE), so that the flow suffers from successive shocks due to pressure mismatch at the entry of the large chamber and becomes subsonic.

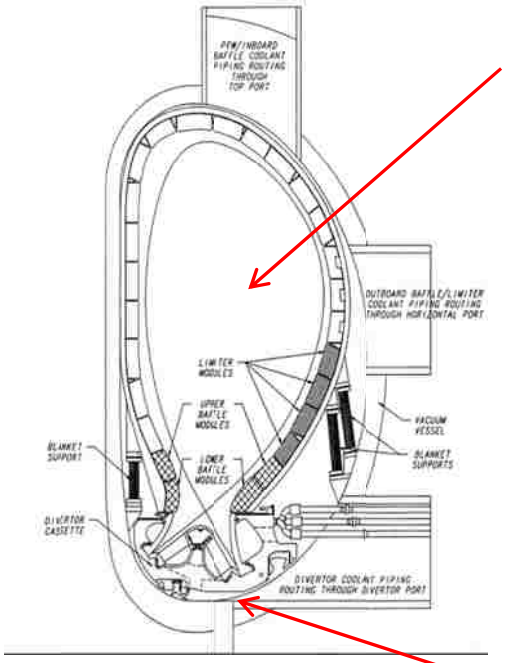


**Fig 1.1** ITER cross-section, A.R. Raffray, et al, Fusion Engineering & Design, 39-40, 323-331 (1998)

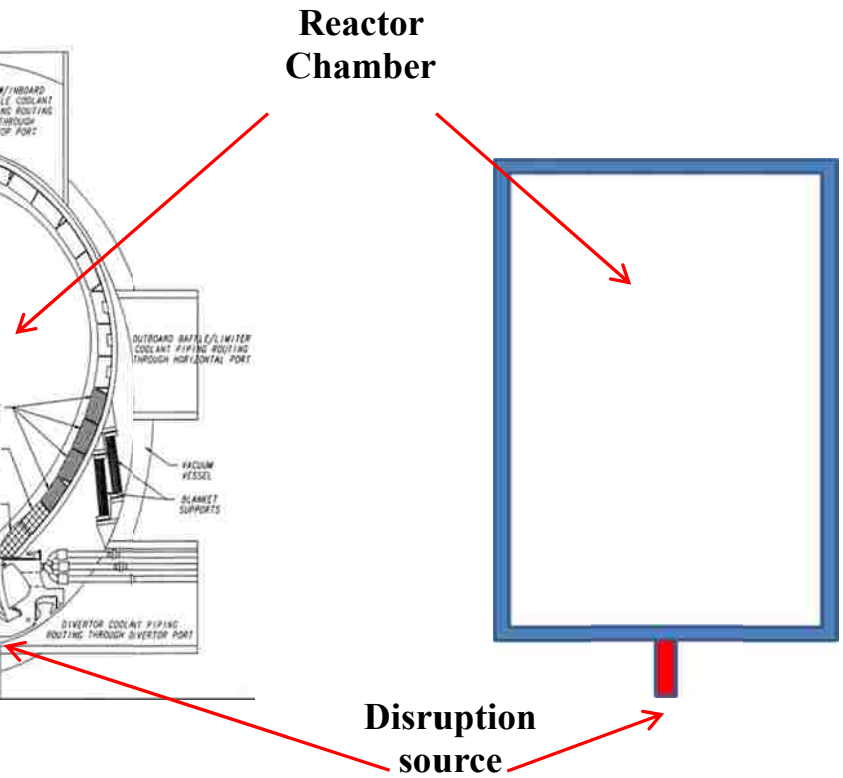


**Fig 1.2** PEPS attached to a cylindrical vacuum chamber simulating the fusion reactor disruption situation

## 1.7 References


[1] Schuller F.C., 'Disruptions in tokamaks', Plasma Phys. Control. Fusion , Vol.31 , pp. A135-Al62, 1995 (Printed in the UK).

[2] Pitts R.A. et al, 'Material erosion and migration in tokamaks', Plasma Phys. Control. Fusion , Vol. 47, pp. B303–B322, 2005.

[3] Shukla P.K., Mamun A.A., 'Introduction to Dusty Plasma Physics', IOP Publishing Ltd., 2002.

[4] Peacock A. T. et al., 'Dust and flakes in the JET MkIIa divertor, analysis and results', Journal of Nuclear Materials, 266:423, 1999.

[5] Winter J., 'Dust in fusion devices - experimental evidence, possible sources and consequences', Plasma Phys. Control. Fusion, Vol. 40, pp.1201–1210, 1998.

[6] Rubela M., Cecconelloa M. et al., 'Dust particles in controlled fusion devices: morphology, observations in the plasma and influence on the plasma performance', Nuclear Fusion, Vol. 41, No. 8, pp. 1087-1099, 2001.

[7] Federicia G., Skinner C.H. et al. , 'Plasma–material interactions in current tokamaks and their implications for next step fusion reactors', Nuclear Fusion, Vol. 41, No. 12R , pp.1967-2137, 2001 .

[8] Coad J.P. et al. ,'Erosion/Deposition issues at JET', Journal of Nuclear Materials, Vol. 290-293, pp. 224-230, 2001.

[9] Rubel M. et al., 'Thick Co-Deposits and Dust in Controlled Fusion Devices with Carbon Walls: Fuel Inventory and Growth Rate of Co-Deposited Layers', Physica Scripta, Vol. T 103, pp. 20–24, 2003.

[10] Linke J. et al., "Carbon particles emission, brittle destruction and co-deposit formation: Experience from electron beam experiments and controlled fusion devices", Physica Scripta, T91, pp. 36-42, 2001.

[11] Bolt H. et al., 'Emission of Solid Particles from Carbon Materials under Pulsed Surface Heat Loads', Physica Scripta, Vol. T 81, pp. 94-97, 1999.

[12] Hassanein A. et al., 'Modeling and simulation of melt-layer erosion during a plasma disruption', Journal of Nuclear Materials, Vol. 214-243, pp. 288-293, 1997.

[13] Sergienko G. et al., 'Erosion of a tungsten limiter under high heat flux in TEXTOR', Journal of Nuclear Materials, Vol. 363-365, pp. 96-100, 2007.

[14] Roth J. et al., 'Recent analysis of key plasma wall interactions issues for ITER', Journal of Nuclear Materials, Vol. 390-391, pp. 1-9, 2009.

[15] Grisolia C. et al., 'Treatment of ITER plasma facing components: Current status and remaining open issues before ITER implementation', Fusion Engineering and Design, Vol. 82, Issues 15–24, pp. 2390–2398, October 2007.

[16] Rosanvallon S. et al., 'Dust control in tokamak environment', Fusion Engineering and Design, Vol. 83, Issues 10-12, pp. 1701-1705, December 2008.

[17] Rosanvallon S. et al., 'Dust limit management strategy in tokamaks', Journal of Nuclear Materials, Vol. 390-391, pp. 57-60, 2009.

[18] Martin J.D., 'Theory and Simulation of Dust in Tokamak Plasmas', Plasma Physics Group, The Blackett Laboratory , Imperial College London, July 2006.

[19] Widdowson A. et al., 'Comparison of JET main chamber erosion with dust collected in the divertor', Journal of Nuclear Materials, Vol.438, Supplement, July 2013, p.S827-S832; Proceedings of the 20th International Conference on Plasma-Surface Interactions in Controlled Fusion Devices.

[20] M. Bourham, O. Hankins, J. Gilligan, J. Hurley and W. Eddy, 'Performance of graphites and tungsten during xxposure to pulsed plasmas, Fusion Technology, Vol.21, No.3, 1852-1857 (1992).

[21] J. Gilligan and M. Bourham, 'The use of an electrothermal plasma gun to simulate the extremely high heat flux conditions of a tokamak disruption', J. Fusion Energy, Vol.12, No.3, pp. 311-316, 1993.

[22] J.P. Sharpe, B.J. Merrill, D.A. Petti, M.A. Bourham and J.G. Gilligan, 'Modeling of particulate production in the SIRENS plasma disruption simulator', J. Nuclear Materials, Vol. 290, pp.1128-1133, 3, March 2001.

[23] Dale G.E. , Bourham M.A., 'Pulse power system characterization of the plasma interactions with propellants experiment (PIPE) electrothermal plasma gun', IEEE Trans. Plasma Science, Vol.30, Issue No. 5, pp. 1852 – 1857, October 2002.

[24] Nakamura Y., Yokota T. and Shukla P.K. , 'Frontiers in Dusty Plasmas', 1st Edition, Elsevier, 2000.

# 2

# Basics of Pulsed Electrothermal Plasma Source (PEPS)

## 2.1 Brief description of PEPS

PEPS is essentially a high current, temperature, velocity and high pressure dense electrothermal plasma discharge. Typical capillary electrothermal plasma sources having ablative sleeve of 4 mm diameter and 9-12 cm length, working in the ablation-controlled arc regime, are capable of producing exit pressures in the range of 100-400 MPa, kinetic temperatures 1-5 eV, number density of $10^{24}$-$10^{28}$/$m^3$and radiant heat fluxes in the range of 50-60 GW/$m^2$ over a 100 μs discharge period, with the plasma jets out of the capillary at velocities 1-6 km/s **[1, 3].**

Capillary discharges generally consist of a long tubular ablating sleeve of a non-conductive material (usually high density polyethylene or thermoplastic polycarbonate like Lexan). However the sleeve material of the capillary can be fabricated from any material or compound in tubular shape to fit inside the capillary. There are a number of reasons behind Lexan emerging out as a choice of material for the capillary discharge sleeve for the pulsed electrothermal plasma sources. First of all, Lexan exhibits exceptionally high impact strength over a wide temperature range and its good flame retardancy makes it a reliable candidate for high current microsecond discharge applications. Lexan 9030 sheet can be cut, sawn, drilled, milled and bent easily using standard workshop equipment without the risk of cracking and breakage. For an electrically conductive sleeve material, the sleeve must have two insulator end-pieces to isolate it from the cathode and the anode to prevent short-circuiting the discharge and to force the creation of an arc to induce surface ablation via the arc radiant heat flux.

## 2.2 Working Principle of PEPS

In the present case the cathode is inserted into one end of the capillary, while the anode is a hollow cylinder surrounding the capillary. In some high pressure applications capillary discharges are ignited by creating a pre-discharge plasma throughout the capillary using ignition source (such as an exploding wire). In the present case, upon closing the switch of PFN (Pulse Forming Network), the charged capacitive energy source, that is connected across the electrodes, discharges and forms the arc. The discharge current heats the plasma Ohmically to high temperatures and radiation heat transport to the wall becomes the dominant heat transfer mechanism causing ablation of the wall material. The ablated wall material, therefore, forms the plasma via dissociation followed by ionization, and the plasma flows out the open end of the capillary to the expansion chamber. The arc energy is principally dissipated in ablation, heating, dissociation, ionization, and acceleration of the ablated material **[2].**

## 2.3 How does PEPS virtually integrate with ETFLOW code?

Electrothermal plasma sources operating in the confined controlled-arc regime are characterized by the magnitude and shape of the discharge current. The desired plasma parameters at the source exit, especially the pressure and heat flux, are highly dependent on the arc due to the effect of the arc radiant energy that ablates the inner wall of the source **[3].** The ETFLOW is a 1-D, time dependent code that models plasma formation and flow in electrothermal capillary discharges. The system of governing equations is solved self-consistently to obtain the plasma parameters such as the plasma temperature and density, kinetic pressure, plasma velocity, total ablated mass, and plasma conductivity. The code is written in FORTRAN and runs in a VBA environment. A circuit module has been developed and incorporated in the code to generate desired current shapes and magnitudes. The basic equations are the conservation of mass, momentum, and energy with the detailed plasma models, Saha equation, and the equation of state, ionization, viscosity and electrical conductivity with both ideal and nonideal formalism. Full details of the complete set of equations are given in some of the previously published literature **[4, 5].** ETFLOW

capillary code models the plasma generation and flow inside the capillary discharges and determines the plasma parameters. The input file to the code is the discharge current density providing the Joule heating in the energy equation. The code runs to give various bulk flow properties of interest like pressure, temperature, density, total ablated mass, bulk velocity etc. at different axial nodes, and the values at the last node (exit node) serve as the source parameters for the test impurity jet of interest or simulation of aerosol flow patterns.

In a recent improvement on the modelling of electrothermal plasma source with radiation transport as prescribed by *Zaghloul* **[6],** the plasma column was modelled as a grey gas the emissivity of which is calculated using an effective beam length. The radiative heat flux escaping the surface of the grey plasma column was used to calculate the rate of the ablated mass which improved the temporal behaviour of the calculated plasma parameters. The ablation process was dealt with greater care than before and the evaluation of the average specific energy (or the heat of sublimation) of the ablated material was determined iteratively for each shot to produce total ablated mass matching the measured one to the experimental uncertainty. Computational results of the evolution and flow of the heated nonideal plasma in the capillary of an ET plasma source showed subsonic condition at the capillary source exit for discharge conditions considered in that study, which goes against the prior assumption of choked-flow at the bore exit, as excessively used in the literature.

Winfrey et al showed **[7]** that faster or longer or extended flat-top pulses can also be generated to satisfy various applications of ET sources. Calculations for non-ideal and ideal plasma models showed that extended flat-top pulses produce more ablated mass, which scales linearly with increased pulse length, while other parameters remaining almost constant.

Recently a new configuration of the PIPE source has been proposed in order to investigate the formation of plasmas from mixed materials. The electrothermal segmented plasma source can be used for studies related to surface coatings, surface modification, ion implantation, material synthesis, and the physics of complex mixed plasmas. This source is a capillary discharge where the ablation liner is made from segments of different materials instead of a single sleeve. An ablation-free capillary discharge computer code has been

developed to model plasma flow and acceleration of pellets for fusion fueling in magnetic fusion reactors. Case studies with and without ablation, including different source configurations have been performed. Velocities necessary for fusion fueling have been achieved **[7].**

### 2.4 Some of the applications of PEPS

The use of electrothermal plasmas has been extended to cover a wide range of applications in fusion as drivers for pellet injectors and as high heat flux sources for fusion materials studies. The high-pressure high heat flux flow is also of application in mass accelerators and launch technology systems **[8-12].**

Application of ET technology to surface coating was initially investigated by Shcolnikov et al. **[13]** in which a theoretical study was proposed using the ET plasma to accelerate powder particles with a view to producing coatings with strong adhesion and low porosity for the target substrates. Similarly, Zoler et al. **[14]** developed a model for the study of powder particle acceleration in an ablative capillary system to simultaneously obtain needed plasma parameters and the acceleration of powder particles. Shcolnikov et al. **[15- 17]** extended their research on powder acceleration by including an additional cylindrical cavity filled with micro particles in the structure of the ET plasma accelerator to be accelerated towards the exit where the heated micro particles in the plasma stream impinge on a target to provide surface coating. Thermal plasma sprayers, also plasma torches, utilize high density plasmas to spray ceramic powders on tools and mechanical parts to ensure higher durability **[18].** Recently, sprays containing mixed powders of structured amorphous metals have been used on surfaces of high-level nuclear waste packages to provide protective barrier **[19].**

Winfrey and Bourham proposed and computationally studied the concept of segmented electrothermal plasma source **[20]** with a view to exploring the possibility of using it in material synthesis technique for surface coating applications. A study of the plasma source with a single metal capillary liner was performed, which showed that production of singly and doubly ionized ions is at high number density sufficient for ionic mixing for deposition on targets and implantation on substrates for surface coating and hardening.

## 2.5 References


[1] R. Majumdar, J.G. Gilligan, A.L. Winfrey and M.A. Bourham, Supersonic flow patterns from electrothermal plasma source for simulated ablation and aerosol expansion following a fusion disruption, J. Fusion Energy, **33**(1), 25-31 (2014).

[2] Mofreh R. Zaghloul, Mohamed A. Bourham and J. Michael Doster, "Semi-analytical modelling and simulation of the evolution and flow of Ohmically-heated non-ideal plasmas in electrothermal guns", J. Phys. D: Appl. Phys., 34 , 772–786 (2001).

[3] M.A. Abd Al-Halim and M.A. Bourham, "Characterization of Short Intense Pulsed Electrothermal Plasma Capillaries for Use as Fusion and Launchers Heat Flux Sources", J. Fusion Energy, 33 (3), 258-263 (2014).

[4] J.D. Hurley, M.A. Bourham, J.G. Gilligan, "Numerical simulation and experiment of plasma flow in the electrothermal launcher SIRENS", IEEE Trans. Magn., 31, 616 (1995).

[5] A.L. Winfrey, M. Abd Al-Halim, A.V. Saveliev, J.G. Gilligan, M.A. Bourham, "A study of plasma parameters in a capillary discharge with calculations using ideal and non-ideal plasma models for comparison with experiment", IEEE Trans. Plasma Sci., 40, 843 (2012).

[6] Mofreh R. Zaghloul, "Improved modelling of electrothermal plasma source with radiation transport", J. Phys. D: Appl. Phys. 41 (2008) 225206.

[7] A. Leigh Winfrey, "A Numerical Study of the Non-Ideal Behavior, Parameters, and Novel Applications of an Electrothermal Plasma Source", Ph.D. Dissertation, North Carolina State University (2010).

[8] R.W. Kincaid, M.A. Bourham, "Electrothermal plasma gun as a pellet injector. J. Fusion Technol., vol.26, pp.637-641, Nov. 1994.

[9] A.L. Winfrey, J.G. Gilligan, M.A. Bourham, "Computational study of a capillary discharge pellet accelerator concept for magnetic fusion fueling," J. Fusion Energy, vol. 32, pp.227-234, April 2013.

[10] J. Gilligan and M. Bourham, "The use of an electrothermal plasma gun to simulate the extremely high heat flux conditions of a tokamak disruption," J. Fusion Energy, vol.12, pp.311-316, Sept. 1993.

[11] T. Edamitsu and H. Tahara, “Experimental and numerical study of an electrothermal pulsed plasma thruster for small satellites,” Vacuum, vol.80, pp. 1223-1228, Sept. 2006.

[12] A.L. Winfrey, M. Abd-Al Halim, A.V. Saveliev, J.G. Gilligan, M.A. Bourham, “Enhanced performance of electrothermal plasma sources as fusion pellet injection drivers and space based mini-thrusters via extension of a flattop discharge current,” J. Fusion Energy, vol.32, pp.371-377, June 2013.

[13] E. Shcolnikov, A. Chebotarev, A. Ignatovitch, I. Kolensky, Yu. Kulikov, A. Melnik and S. Volkov , “Acceleration of powder materials in an electrothermal launcher,” IEEE Trans. Magnetics, vol.31, pp.758–763, Jan. 1995.

[14] D. Zolery, Z. Kaplan and J. Ashkenazy, “Analysis of powder particle acceleration and heating processes in a discharge capillary ablative pipe device,” Plasma Sources Sci. Technol., vol. 5, pp. 588-601, 1996.

[15] E. Shcolnikov, M. Guzeyev, S. Maslennikov, A. Melnlk, A. Chebotarev, “Flow dynamics and microparticles acceleration in the electrothermal launcher,” IEEE Trans. Magnetics, vol. 35, pp. 240– 244, January 1999.

[16] E. Shcolnikov, M. Guzeyev, S. Maslennikov, N. Netchaev, A. Chebotarev, “Acceleration of microparticles in electrothermal launcher with multigap scheme of discharge unit,” IEEE Trans. Magnetics, vol. 37, pp. 188–193, Jan. 2001.

[17] E. Shcolnikov, S. Maslennikov, N. Netchaev, V. Nevolin, L. Sukhanova, “Electrothermal technology of coating,” IEEE Trans. Plasma Sc., vol.39, pp. 314-318, Jan. 2003.

[18] P. Chagnon and P. Fauchais, "Thermal spraying of ceramics," Ceramics International, vol. 10, pp.119- 131, 1984.

[19] J. Blink, J. Farmer, J. Choi, C. Saw, "Applications in the nuclear industry for thermal spray amorphous metal and ceramic coatings," Metallurgical and Materials Trans. A, vol. 40A, pp.1344-1354, 2009.

[20] A.L. Winfrey and M.A. Bourham , “A computational study of a segmented electrothermal plasma source”, 19th Pulsed Power Conference, San Francisco, 2013, DOI: 10.1109/PPC.2013.6627443.

# 3

# Study of 1-D supersonic bulk flow patterns from PEPS for simulated ablation and aerosol expansion following a fusion disruption

*Published in J. Fusion Energy: "Supersonic Flow Patterns from Electrothermal Plasma Source for Simulated Ablation and Aerosol Expansion Following a Fusion Disruption", Rudrodip Majumdar, John G. Gilligan, A. Leigh Winfrey and Mohamed A. Bourham, J. Fusion Energy, Vol.33 (1), pp. 25-31, February 2014. DOI: 10.1007/s10894-013-9635-8.*

A pulsed electrothermal plasma source (PEPS) of a capillary discharge operating in the confined controlled arc regime is investigated to simulate the source term for ablation-induced regime of fusion reactor following hard disruption, in which ablation of diverter surface produces large aerosol transporting into the vacuum vessel. The source is attached to a converging-diverging micro-nozzle transition region to allow for the plasma flow and expansion into a large volume simulating large chamber of fusion reactor aerosol expansion to facilitate modeling of the plasma transport. This transition region connects to a 4mm diameter capillary source and has a 3.33 mm converging section with a $2^o$ converging angle, followed by a 146.7 mm diverging section with a $60^o$ diverging angle, thus making an overall transition length of ~150mm. The diverging section has an exit diameter of 50.82 cm to open into a large volume of the same exit diameter and a length of 1m. Preliminary computation results indicate about 21 Mach number at the diverging exit and drops down to 0.7 Mach number after suffering from multiple shocks in the large uniform expansion volume. The plasma parameters entering the large chamber are maintained constant along the axis of the chamber for a simulated 1-D condition.

## 3.1 Introduction

The present work investigates pulsed electrothermal plasma source (PEPS), which is essentially a high current, temperature, velocity and high-pressure dense electrothermal

discharge coupled to a supersonic nozzle to investigate the expansion of aerosol particulates into the vacuum chamber of fusion reactors following a hard disruption event. Disruption events expected in fusion large tokamaks can deposit localized heat fluxes up to 100 $GW/m^2$ over a short period of about 100-1000μs, resulting in evaporation of interior critical components, especially the diverter, and causing particulates spreading into the reactor vacuum vessel [1-2]. Electrothermal plasma sources are good experimental and computational simulators for disruption studies [1-2]. Typical electrothermal plasma sources of 4mm diameter, 9-12cm long, working in the ablative capillary regime, produce pressures in the range of 100 – 400Mpa, with kinetic temperatures 1-4eV, dense plasmas of $10^{24}$-$10^{28}/m^3$ and heat fluxes in the range of 50-60$GW/m^2$ over a 100μs discharge period [3-7].

Considerable effort has been put in the study of problems similar to the capillary discharge, such as the ablation-stabilized arcs, confined electrothermal discharges, electrothermal-chemical propulsion, and high-density coaxial plasma sprayers. Both computational and experimental research were conducted for these devices with computational work ranging from 0-D, steady- state scenarios, to 1-D, time dependent modeling, and a recent 2-D, time-dependent capillary plasma modeling. Experimental work utilized pulse-forming network for pulse shaping for high-voltage, high-current operation. Computational calculations are also coupled to both the pulse-forming networks and the interior-ballistic models of the ablative flow or the working fluid.

A schematic of an ablative capillary plasma source is shown in Figure 1. The pulse power system is typically a high energy density capacitor with pulse forming network (PFN). An arc is created inside the capillary upon discharging the capacitor, and the arc radiates heat to the inner wall of the ablating sleeve. Radiation heat flux ablates sleeve material, dissociates and ionizes the ablated species to form dense plasma. The ablative capillary discharge can be described as a three-layer system in which the outermost layer is a solid wall, the middle is material from the evaporated wall, and the innermost layer is the plasma core. The plasma pressure ejects the plasma species out of the source into either free space or into a transition nozzle depending on the desired application. Ohmic heating is the primary source responsible for wall heating, ablation, dissociation and ionization. For the case of

open-end source, as shown in Figure 3.1, a subsonic condition (Ma < 1) exists at the exit of the capillary.

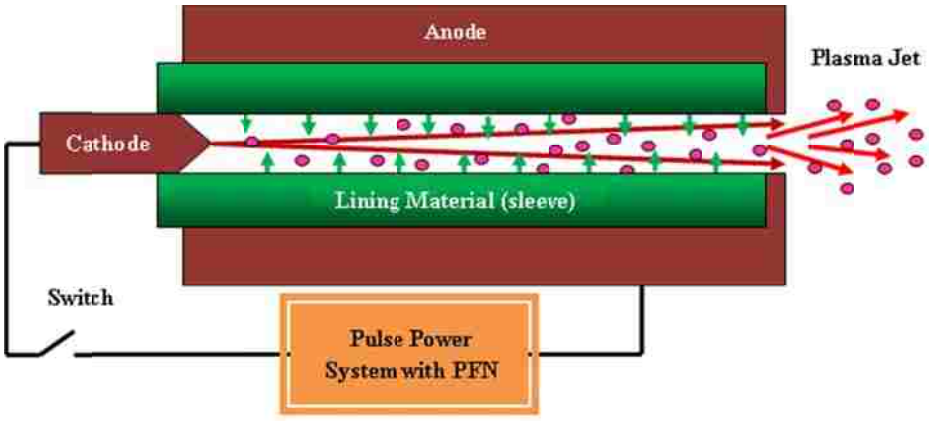


**Fig. 3.1** Schematic diagram of a capillary discharge

In a previous modeling, a small diverging transition region was allowed between the electrothermal source and the chamber with a linear expansion to facilitate the numerical technique for the sudden expansion [**1-2**]. Here in the current research to simulate plasma flow and expansion following a disruption event, a conversing-diverging nozzle is attached to the source exit to allow for the plasma expansion through a transition region into a large volume. This attachment allows for the simplicity of computational simulation of aerosol expansion following a plasma disruption in tokamak fusion reactors, where disruption induces evaporation/ablation of the reactor's plasma facing components (PFC), especially the diverter. The addition of this converging-diverging nozzle is essential to provide the smooth transition from the source exit into a large chamber without choking the flow. As illustrated in Figure 3.2, a small 3.3mm long converging section with an inlet diameter of 4mm, exactly the same as the source exit diameter) followed by 146.7 mm long diverging section with 508.2 mm diameter makes the transitional region with a total length of 150 mm. The diverging section connects to a 1000mm long chamber with same diameter (508.2 mm) to simulate opening the source into a large volume simulating a fusion reactor vacuum vessel.

In the present study, the variations of plasma density, pressure, velocity and temperature, as function of the axial distance traversed from the micro-nozzle outlet are

investigated. The capillary source is capable of exhibiting pressures in the range of 100–400 MPa, temperatures of the order of 1–5 eV and heat fluxes up to 50-60 GW/m$^2$ over a 100μs.

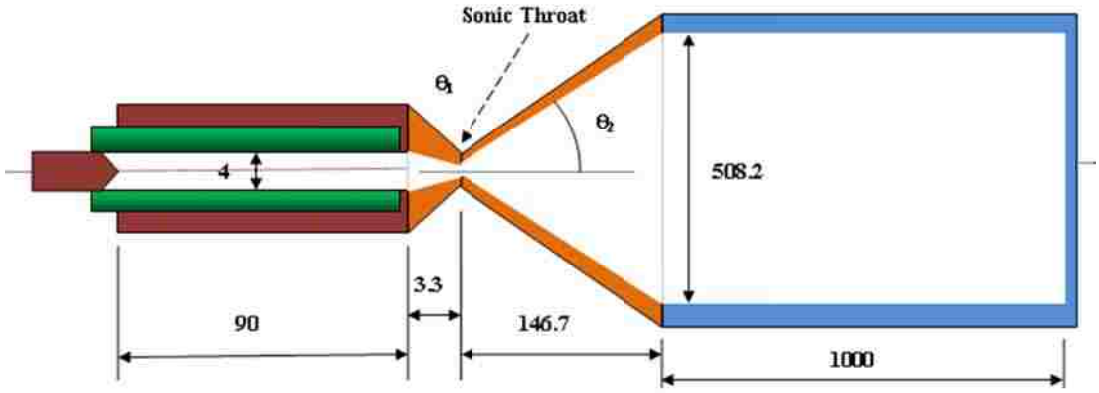


**Figure 3.2** Schematic diagram of the capillary discharge with the attached transition and expansion regions, $\theta_1=2^o$ and $\theta_2=60^o$, dimensions in mm (not to scale)

## 3.2 Computational Modeling of Capillary Extended Nozzle

### *3.2.1 Governing Equations and Assumptions*

In this study it is assumed that there is only axial variation in the parameters of interest, the parameters inside of the capillary are radially-uniform. The parameters in the converging-diverging section and inside of the large chamber are investigated only on axis; however, a 2-D model is under development for further investigation of the radial distributions. Also only axial flow is considered in the large chamber with no changes in the magnitude of the parameters as plasma enters the chamber, however, this is only for the purpose of the 1-D model.

The study considers subsonic flow in the converging section of the transition region, which eventually becomes sonic at the sonic throat, then the flow becomes supersonic In the diverging section, the plasma bulk velocity increases and the Mach number steadily increases with the increase in the cross-section along the length of this section. In the expansion chamber, the supersonic flow undergoes oblique / normal shocks until it becomes subsonic.

The shock wave comes into play, when the flow area for a supersonic fluid flow is suddenly reduced.

It is essential to determine the cross-sectional area of the sonic throat to establish a mathematical relationship between the Mach number and the flow cross-sectional area; which in turn establishes a relationship between the Mach number and the distance from the capillary exit into the transition region. The electrothermal source dimensions are fixed to 4mm exit diameter and 9cm source length, and the exit parameter is exactly equal to the inlet diameter of the converging section. The cross-sectional area of the sonic throat $A^*$ can be related to that of the inlet to the converging section $A$, which is the area of the capillary exit, by the following equation well known in literature [8, 9]:

$$A^* = A\, M_a \left[ \left(1 + 0.5(\gamma - 1) M_a^2\right) / 0.5(\gamma + 1) \right]^{-(\gamma+1)/2(\gamma-1)} \tag{3.1}$$

Where $M_a$ is the capillary exit Mach number and $\gamma = C_p / C_v$ is the specific heat ratio.

Using the value of $A^*$ from Eq. 3.1, it is possible to establish a mathematical relationship describing the Mach number $M_a'$ of the transition region as a function of the cross-sectional area ($A'$) at any location along the length of the transition region, i.e. the dynamic cross-sectional area $A'$ moving from the source exit into the throat and beyond.

In the converging section, where the flow is subsonic, the expression of the Mach number $M_a'$ is given the standard subsonic fluid flow equations for the limits of the values of $\left(A' / A^*\right)$ ratio as described in literature [8, 9]:

$$\left.\begin{aligned} M_a' &= \frac{1 + 0.27\left(A' / A^*\right)^{-2}}{1.728\left(A' / A^*\right)} \quad , \quad 1.34 < \left(A' / A^*\right) < \infty \\ M_a' &= 1 - 0.88\left[\ln\left(A'/ A^*\right)\right]^{0.45} \quad , \quad 1.0 < \left(A' / A^*\right) < 1.34 \end{aligned}\right\}, \tag{3.2}$$

whereas, in the diverging section, where the flow is supersonic, the expression of the Mach number is given by the standard supersonic fluid flow equations for the limits of the values of $\left(A^{'}/A^{*}\right)$ ratio as described in literature [8, 9]:

$$\left.\begin{aligned} M_a^{'} &= 1+1.2\left[\left(A'/A^{*}\right)-1\right]^{0.5} \quad , \quad 1.0<\left(A^{'}/A^{*}\right)<2.9 \\ M_a^{'} &= \left[216\left(A'/A^{*}\right)-254\left(A'/A^{*}\right)^{2/3}\right]^{1/5} \quad , \quad 2.9<\left(A^{'}/A^{*}\right)<\infty \end{aligned}\right\} \tag{3.3}$$

The plasma parameters, density $\rho'$, pressure $P'$, plasma temperature $T'$ and bulk velocity $v'$, can be calculated at any position in the converging-diverging transition region utilizing the Mach number values obtained from the above equations [8, 9], and are expressed as follows:

$$\left.\begin{aligned} \rho^{'} &= \rho\left[1+0.5\left(\gamma-1\right)\left(M_a\right)^2\right]^{\frac{1}{\gamma-1}} / \left[1+0.5\left(\gamma-1\right)\left(M_a^{'}\right)^2\right]^{\frac{1}{\gamma-1}} \\ P^{'} &= P\left[1+0.5\left(\gamma-1\right)\left(M_a\right)^2\right]^{\frac{\gamma}{\gamma-1}} / \left[1+0.5\left(\gamma-1\right)\left(M_a^{'}\right)^2\right]^{\frac{\gamma}{\gamma-1}} \\ T^{'} &= T\left[1+0.5\left(\gamma-1\right)\left(M_a\right)^2\right] / \left[1+0.5\left(\gamma-1\right)\left(M_a^{'}\right)^2\right] \\ v^{'} &= M_a^{'}\left(\gamma P^{'}/\rho^{'}\right)^{1/2} \end{aligned}\right\} \tag{3.4}$$

These equations can be used to compute the plasma pressure, plasma bulk velocity, temperature and the density at the exit of the diverging section, where these values will constitute the input parameters for the shock model inside the uniform expansion chamber. The plasma temperature, density, pressure and velocity at the ET source exit, entering into the transition region, are taken from the data of an experimental ET system [7, 10]. Table 3.1 lists the plasma parameters for four selected shots [10] and their analysis by the ETFLOW code [7]. Shot P213 is the one with the lowest discharge current (9.4 kA), which has a radiative heat flux of 8.62 GW/m$^2$ over a 100 μs. Shot P206 has a discharge energy of 6.01kJ with current of 42.81kA over a 100μs pulse length, producing a heat flux of 48.63 GW/m$^2$. The heat fluxes of these shots are, very relevant to expected heat fluxes in ITER during a disruption event [**1**]. The exit peak temperature of the ET source for shot P206 is 2.63eV, with plasma density of 8.601 kg/m$^3$, exit pressure of 386MPa at an exit velocity of 6.16km/s

[7]. These parameters are used as the input parameters in the calculation of the plasma parameters in the converging-diverging transition region.

**Table 3.1** Plasma parameters at the ET source exit as input to the converging-diverging section

| | P213 | P191 | P197 | P206 |
|---|---|---|---|---|
| I (kA) peak discharge current | 9.4 | 17.7 | 29.61 | 42.81 |
| E (kJ) net input energuy | 1.09 | 2.41 | 4.60 | 6.01 |
| $M_{total}$ (mg) total ablated mass | 8.89 | 17.51 | 28.36 | 40.18 |
| q" ($GW/m^2$) radiation heat flux | 8.62 | 17.17 | 31.20 | 48.63 |
| T (eV) peak plasma temperature | 1.706 | 2.024 | 2.352 | 2.627 |
| P (MPa) peak exit pressure | 52.5 | 120 | 235 | 386 |
| ρ ($kg/m^3$) plasma density | 0.409 | 3.618 | 5.955 | 8.601 |
| v (km/s) peak exit velocity | 4.74 | 5.25 | 5.75 | 6.16 |

Once the Mach number $M_{a1}$, pressure $P_1$, temperature $T_1$, density $\rho_1$ and the bulk velocity $v_1$ at the exit of the diverging section are determined (i.e. just before the shock wave comes into play); the standard well-defined mathematical expressions that describe the normal and oblique shocks as described in Ref. 8 and 9 can be used to calculate post shock plasma parameters $M_{a2}$, $P_2$, $T_2$, $\rho_2$ and $v_2$.

The flow suffers from shocks when the supersonic flow coming out of the diverging section suddenly enters the closed large cylindrical expansion chamber. Flows with very high Mach numbers undergo oblique shock, and when the Mach number is quite small, normal shock occurs. Roughly it is reasonable to indicate that as the Mach number decreases, the shock angle increases.

In case of normal shock, the plasma parameters can be given by the following expressions as described in Ref. 8 and 9:

$$\left.\begin{aligned} M_{a2} &= \left[\left[(\gamma-1)M_{a1}^2+2\right]/\left[2\gamma M_{a1}^2-(\gamma-1)\right]\right]^{1/2} \\ T_2 &= T_1\left[1+0.5(\gamma-1)M_{a1}^2\right]\left[\left(2\gamma M_{a1}^2/(\gamma-1)\right)-1\right]/\left[(\gamma+1)^2 M_{a1}^2/0.5(\gamma-1)\right] \\ \rho_2 &= \rho_1\left[(\gamma+1)M_{a1}^2\right]/\left[(\gamma-1)M_{a1}^2+2\right] \\ P_2 &= P_1\left[2\gamma M_{a1}^2-(\gamma-1)\right]/(\gamma+1) \end{aligned}\right\} \quad (3.5)$$

When oblique shock occurs, the equations are modified to include the sinusoid of the shock angle $\theta$ and hence the oblique shock equations for the plasma parameters, as listed in Ref. 9, are used, and $\delta$ is the deviation angle:

$$\left.\begin{aligned} M_{a2} &= \left[\left[(\gamma-1)M_{a1}^2 Sin^2\theta + 2\right] / \left[2\gamma M_{a1}^2 Sin^2\theta - (\gamma-1)\right]\left[Sin^2(\theta-\delta)\right]\right]^{1/2} \\ \delta &= Cot^{-1}\left(\left[(\gamma+1)M_{a1}^2 / \left[2M_{a1}^2 Sin^2\theta - 1\right] - 1\right]\tan\theta\right) \\ T_2 &= T_1\left[2\gamma M_{a1}^2 Sin^2\theta - (\gamma-1)\right]\left[M_{a1}^2(\gamma-1)Sin^2\theta + 2\right] / \left[(\gamma+1)^2 M_{a1}^2 Sin^2\theta\right] \\ P_2 &= P_1\left[2\gamma M_{a1}^2 Sin^2\theta - (\gamma-1)\right] / (\gamma+1) \\ \rho_2 &= \rho_1\left[(\gamma+1)M_{a1}^2 Sin^2\theta\right] / \left[(\gamma-1)M_{a1}^2 Sin^2\theta + 2\right] \\ v_2 &= M_{a2}(\gamma P_2 / \rho_2)^{1/2} \end{aligned}\right\} . \quad (3.6)$$

Using the above set of well-known formulae that are related to shocks, the values of the parameters of interest after successive shocks can be computed.

### *3.2.2 Solution Strategy and Assumptions*

In the computational analysis the shock angle θ for certain Mach number ranges were defined as shown in Table 3.2; however, these angles may be verified through experimental data.

**Table 3.2** Shock angle $\theta$ defined for ranges of Mach number (*Ma)*

| Mach Number *Ma* Range | Shock angle $\theta^o$ |
|---|---|
| Ma <0.8 | No shock, Mach # unchanged |
| 0.8 ≤ Ma <1.2 | 90 (Normal Shock) 1.5708 |
| 1.2 ≤ Ma < 3 | 85 (Near Normal Shock) 1.4835 |
| 3 ≤ Ma < 5.5 | 75 (Oblique Shock) 1.3090 |
| 5.5 ≤ Ma < 9 | 65 (Oblique Shock) 1.1345 |
| 9 ≤ Ma <12 | 55 (Oblique Shock) 0.9599 |
| 12 ≤ Ma <16 | 42 (Oblique Shock) 0.7330 |
| 16 ≤ Ma < 20 | 36 (Oblique Shock) 0.6283 |
| 20 ≤ Ma | 30 (Oblique Shock) 0.5236 |

Additionally, scaling laws based on the magnitude of the shock angle $\theta$ for the Mach number ranges were established with two different fit equations. The shock angle $\theta$ (in radian) versus the Mach number *Ma* can be expressed by the following fit relations

$$\left.\begin{aligned}\theta_{radians} &= 0.0021M_a^2 - 0.0963M_a + 1.6202\\ \theta_{radians} &= 1.587e^{-0.058M_a}\end{aligned}\right\} \quad (3.7)$$

These are the best fits and turns close results, however the quadratic fit was used in the calculations of the deviation angle $\delta$ and the plasma parameters for the oblique shock.

A stand-alone routine has been created to simulate the shock. The Mach number, temperature, pressure and density at the diverging exit of the transition region are used as the input to the shock routine. The routine checks the Mach number and decides whether to use the normal shock or the oblique shock based on the criteria given in Table 3.2. In case of an oblique shock the angle is estimated using the quadratic fit scaling law, and the deviation angle is calculated subsequently. The plasma parameters are calculated again along with plasma velocity for each value of Mach number at each spatial step. The shock routine re-checks the Mach number for the subsequent iteration and continues to modify the flow parameters until the flow become subsonic. In this work, as the expansion chamber has been assumed to be of uniform cross-section, so the values of the plasma parameters reach a steady state once the flow becomes subsonic.

### 3.3 Results and Discussion

The variation of the plasma parameters as a function of the length of the transition converging-diverging region and along the length of the expansion chamber is calculated. Figure 3.3 illustrates the change in the Mach number over the length of the transition and chamber regions. At L=0, it indicates the Mach number at the electrothermal source exit, which is 0.54, then the Mach number slightly increases to 0.87 inside the converging section. The Mach number suddenly increases in the diverging section and reaches its peak of 21.02 at the end of this section. It is quite expected because the flow eventually has to become supersonic at the diverging exit, after starting as subsonic flow at the capillary exit. This increase to 21.02 Mach number is at the interface between the exit of the diverging section

and the entry to the chamber where the Mach number drops fast due to the expansion and stays at 0.707 over the entire length of the chamber.

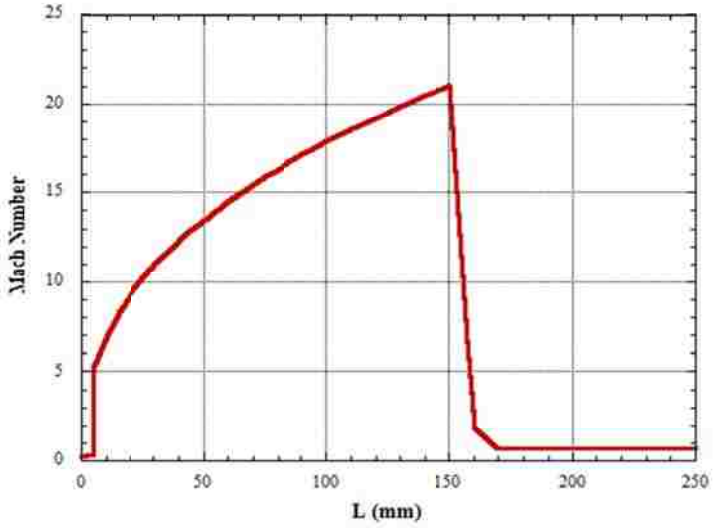


**Figure 3.3** Change in the Mach number over the length of the transition and chamber regions

The plasma kinetic temperature on the axis of the transition and the chamber regions is shown in Figure 3.4 for the 4 cases of study, shots P213, 191, 197 and 206. Temperatures at L=0 are the peak temperatures at the PEPS exit as listed in Table 1. The temperature drops to 1.8eV inside the converging section, and drops further in the diverging section for all cases, which is quite expected because of the expansion assuming the whole process to be isentropic ($\Delta s = 0$). As plasma leaves the diverging section to enter the chamber the temperature rises back to 1.41, 1.67, 1.94 and 2.17eV for shots P213, 191, 197 and 206, respectively; and remains constant along the axis of the chamber.

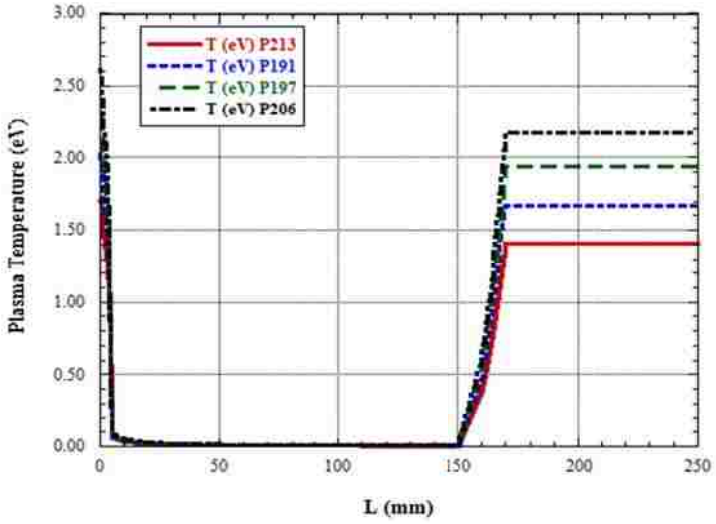


**Figure 3.4** Change in plasma temperature over the length of the transition and chamber regions

The plasma density on the axis of the transition and the chamber regions for the test shots is shown in Figure 3.5, where the density at L=0 is the peak density at the PEPS exit as listed in Table 1. The density drops inside the converging section, and drops further to at the entry of the diverging section, then rises at the chamber's entry to reach 0.114, 1.008, 1,66 and 2.4 kg/m$^3$ for shots P213, 191, 197 and 206, respectively; and remains constant along the axis of the chamber. This density changes will also affect the kinetic pressure causing similar behavior in the converging-diverging section and at the entry and through the chamber. Figure 3.5 is plotted with a log scale to show the details of the density changes along the axis of the converging-diverging section.

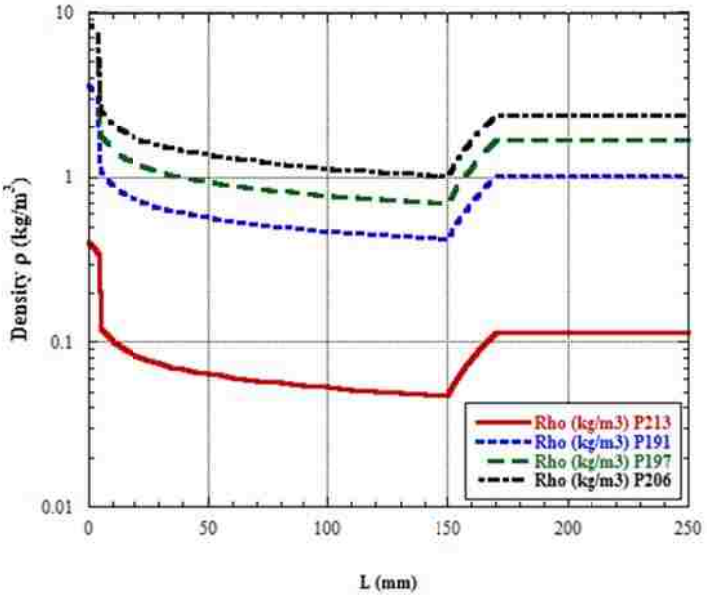


**Figure 3.5** Change in plasma density over the length of the transition and chamber regions

The plasma pressure on the axis of the transition and the chamber regions is shown in Figure 3.6, All values shown at L=0 are the peak pressure values at the PEPS exit as listed in Table 3.1. As previously mentioned, the pressure should have behavior similar to that of the density. The pressure drops from its peak value as plasma flows inside the converging section, and drops further as it enters the diverging section, continues to drop towards the end of the diverging section then rises at the entry to the chamber. The pressure rises to 12.08, 27.6, 54.05 and 88.79MPa for shots P213, 191, 197 and 206, respectively; and remains constant along the axis of the chamber. The change in the magnitude of the pressure along the axis of the diverging-converging section and the chamber is associated with the density and temperature changes. . Figure 3.6 is also plotted with a log scale to show the details of the density changes along the axis of the converging-diverging section.

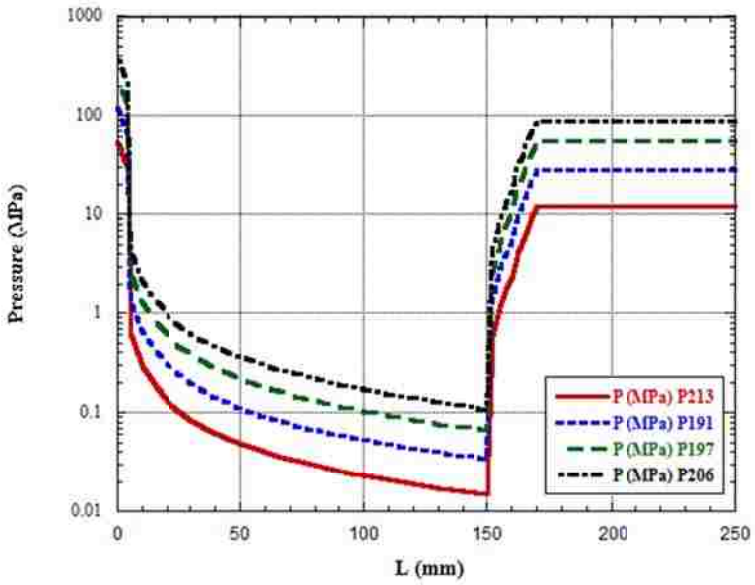


**Figure 3.6** Change in plasma pressure over the length of the transition and chamber regions

The plasma bulk velocity on the axis of the transition and the chamber regions is shown for all test cases in Figure 3.7 along with the Mach number. The plasma velocity at L=0 is the peak exit velocity at the capillary exit as tabulated in Table 3.1. The velocity increases inside the converging section as the Mach number is also increasing, continues to increase towards the end of the diverging section. The velocity reaches 9.02, 9.99, 10.94 and 11.72 km/s for shots P213, 191, 197 and 206, respectively until the flow approaches the entry to the chamber then drops to constant values along the axis of the chamber. At the entry and into the chamber these constant velocity values are 5.64, 6.25, 6.85 and 7.33 km/s for the tested shots P213, 191, 197 and 206, respectively.

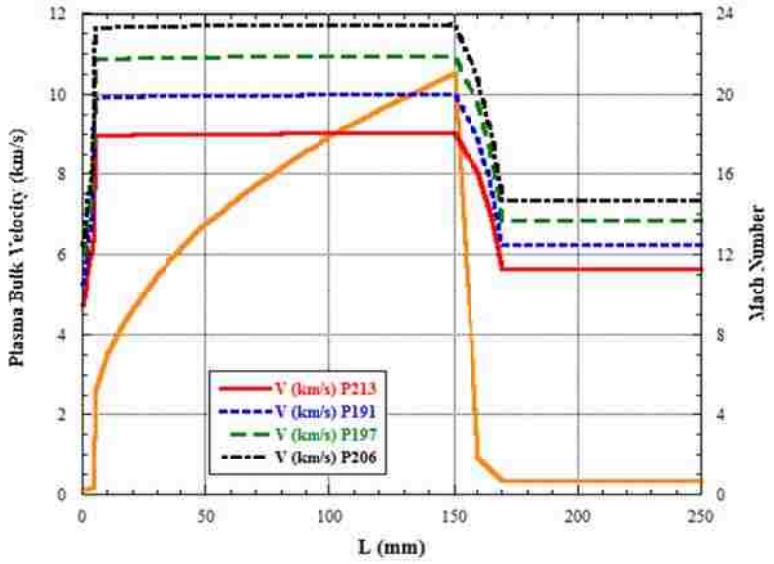


**Figure 3.7** Change in plasma velocity, compared to the change in Mach number, over the length of the transition and chamber regions

The velocity follows the change in the Mach number as seen from the figure 3.7. The speed, as found at the diverging section exit and the corresponding Mach number, shows that after leaving the capillary the flow can become hypersonic. When this hypersonic flow is suddenly flowing through a uniform cross section chamber, then there is a restriction in the flow area and shock waves are generated in the flow. Across a shock wave, the plasma pressure, plasma temperature, and plasma density increases almost instantaneously, whereas the Mach number associated with the flow and plasma bulk velocity decreases.

Table 3.3 summarizes the axial plasma parameters at the chamber's entry, which indicates that a 100μs disruption event with heat fluxes ranging from 8.62 to 48.63 GW/m$^2$ would impart about 9 to 40 mg of ablated mass into the chamber at velocities in the range of 6-7 km/s. While these calculations are only on axis, however, introduction of such ablated mass will increase the impurities into the reactor chamber and allows for spreading dust and nucleation of evolved aerosol particulates [11-13]. The amount of ablation in this study is from the electrothermal PEPS inner surface of 1.131 x 10$^{-3}$ m$^2$, which is a minute fraction of an expected >10 m$^2$ affected surface areas in tokamak fusion reactor like ITER. Hence, the ablation of 40.18mg in the PEPS inner surface area for a 48.63GW/m$^2$ over 100μs will scale

up to ~ 355 grams in a single equivalent disruption event for a $10m^2$ tokamak affected area at the heat flux level.

**Table 3.3** Axial Plasma parameters at the entry of the chamber with a 0.7073 Mach number

| | P213 | P191 | P197 | P206 |
|---|---|---|---|---|
| $M_{total}$ (mg) total mass entry into chamber | 8.89 | 17.51 | 28.36 | 40.18 |
| T (eV) peak plasma temperature on axis | 1.41 | 1.67 | 1.94 | 2.17 |
| P (MPa) peak pressure into chamber | 12.08 | 27.60 | 54.05 | 88.79 |
| ρ ($kg/m^3$) plasma density into chamber | 0.114 | 1.008 | 1.66 | 2.40 |
| v (km/s) peak plasma velocity on axis | 5.64 | 6.25 | 6.85 | 7.33 |

## 3.4 Conclusions

Study of the evolution of plasma from a pulsed electrothermal plasma source (PEPS) as a simulator to the source term for diverter ablation during tokamak disruption has been conducted, in which the source opens into a large chamber as a model for the vacuum vessel. Attaching the source to the chamber was modeled using a converging-diverging transition section. Plasma parameters along the axis of the source, the transition region, and the chamber were obtained using subsonic and supersonic flow models. Data from four actual electrothermal source shots were used to determine the inlet parameters to the diverging-converging section. These data are taken as the peak data at the source exit.

The Mach number increases slightly in the converging section then sharply increases in the diverging section and drops towards the entry to the chamber then stays constant as the plasma expands into the chamber. The velocity follows the profile of the Mach number and stays constant as the plasma travels and expands into the chamber as a result of only using a 1-D model along the axis. Plasma kinetic temperature, density and pressure experience drop into the transition region followed by increases into the chamber. As the flow is restricted in the transition section, shock waves can be generated and thus sudden drops in the plasma parameters are expected while the plasma velocity is increasing.

The study shows that the expansion into the chamber's entry is at steady conditions for the main parameters, temperature, density and pressure, suggesting uniform distribution of the plasma particulates, and hence the aerosol expansion in the chamber following the disruption

would be uniform inside the vacuum vessel. The study shows that the amount of material ablation when scaled up to the size of a tokamak reactor like ITER would ablate ~ 355 grams from a $10m^2$ disruption-affected area at the heat flux of 48.63 $GW/m^2$ over 100 μs used in the simulation. An extension of the work to a 2-D model will provide detailed information on the axial and radial distributions of the aerosol.

## 3.5 References


[1] K.A. McCarthy, D.A. Petti, W.J. Carmack and G.R. Smolik, "The safety implications of tokamak dust size and surface area", Fusion Engineering & Design, Vol.42, issue 1-4, pp.45-52, Sept. 1998.

[2] J.P. Sharpe, B.J. Merrill, D.A. Petti, M.A. Bourham and J.G. Gilligan, "Modeling of particulate production in the SIRENS plasma disruption simulator", J. Nuclear Materials, Vol. 290, pp.1128-1133, March 2001.

[3] J.D. Powell and A.E. Zielinski, "Capillary discharge in the electrothermal gun," IEEE Transactions on Magnetics, Vol. 29, No. 1, pp. 591–596, 1993.

[4] J.D. Hurley, M.A. Bourham and J.G. Gilligan, "Numerical simulation and experiment of plasma flow in the electrothermal launcher SIRENS", IEEE Trans. Magnetics, Vol. 31, pp.616-621, January 1995.

[5] T. Edamitsu and H. Tahara, "Experimental and numerical study of an electrothermal pulsed plasma thruster for small satellites," Vacuum, Vol. 80, No. 11/12, pp. 1223–1228, 2006.

[6] L. Pekker, 'Zero-dimensional time-dependent model of high-pressure ablative capillary discharge for plasma Thrusters", J. Propulsion and Power, Vol. 24, No.4, pp. 958-969, 2009.

[7] L. Winfrey, J. Gilligan, A. Saveliev, M. Abd Al-Halim and M. Bourham, "A study of plasma parameters in a capillary discharge with calculations using ideal and non-ideal plasma models for comparison with experiment, IEEE Trans. Plasma Science, Vol.40, No.3, pp.843-852, March 2012.

[8] J. E. A. John and T. G. Keith, *Gas Dynamics,* 3rd Edition, Pearson Education, Upper Saddle River, NJ, 2005.

[9] Robert D. Zucker and Oscar Biblarz, Fundamentals of Gas Dynamics, 2nd Edition, John Wiley & Sons, Inc., 2002.

[10] G.E. Dale and M.A. Bourham, "Pulse power system characterization of the plasma interactions with propellants experiment (PIPE) electrothermal plasma gun", *IEEE Trans. Plasma Sc*., Vol. 30, No. 5, pp. 1852-1857, October 2002.

[11] J.P. Sharpe, M.A. Bourham and J.G. Gilligan, "Preliminary Investigation Into Aerosol Mobilization Resulting From Fusion Reactor Disruption", *Fusion Technology*, Vol. 30, pp.1424-1428, November 1996.

[12] J.P. Sharpe, M.A. Bourham and J.G. Gilligan, “Experimental Investigation of Disruption-Induced Aerosol Mobilization in Accident Scenarios of ITER”, Proc. 17th IEEE NPSS Symposium on Fusion Engineering, San Diego, CA, 6-10 October 1997, Vol.1, pp.153-156, 1997.

[13] W.J Carmack, R.A Anderl, R.J Pawelko, G.R Smolik and K.A McCarthy, “Characterization and Analysis of Dusts Produced in Three Experimental Tokamaks: TFTR, DIII-D, and Alcator C-Mod”, Fusion Engineering and Design, Vol. 51–52, pp. 477-484, November 2000.

# 4

# Development of 1-D scaling laws for supersonic bulk flow parameters from PEPS for Lexan ablated plasma jet

*Published in J. Fusion Energy: "Scaling Laws of Bulk Plasma Parameters for a 1-D Flow through a Capillary with Extended Converging-Diverging Nozzle for Simulated Expansion into Fusion Reactor Chamber", Rudrodip Majumdar, John G. Gilligan, A. Leigh Winfrey and Mohamed A. Bourham, Vol.34 (4), pp. 905- 910 , August 2015, DOI:10.1007/s10894-015-9899-2.*

A capillary-extended converging–diverging transition region was previously proposed to allow for the flow and expansion of plasma into a large volume simulating aerosol expansion and particle transport in the active volume of a fusion reactor. It has been shown that the pulsed electrothermal plasma source (PEPS) was adequate for the simulation, and the expansion into the chamber is at steady conditions for the main plasma parameters indicating a uniform expansion of the aerosol following a disruption event. These parameters are the bulk temperature, density, pressure, plasma bulk velocity and Mach number for the same system geometrical configuration. Scaling laws in 1-D for bulk plasma parameters have been developed for ranges of axial length traversed by the flow to predict these parameters along the axis of the expansion chamber.

## 4.1 Introduction

Expansion of aerosol particulates into the vacuum chamber of a fusion reactor following a hard disruption event was previously investigated using a supersonic nozzle on the exit of an electrothermal capillary discharge to allow for the transition between the source and the chamber's large volume [1]. A schematic of the capillary discharge with the attached expansion is shown in Fig. 4.1 in which a subsonic to supersonic transition region is inserted between the electrothermal source and the expansion chamber [1].

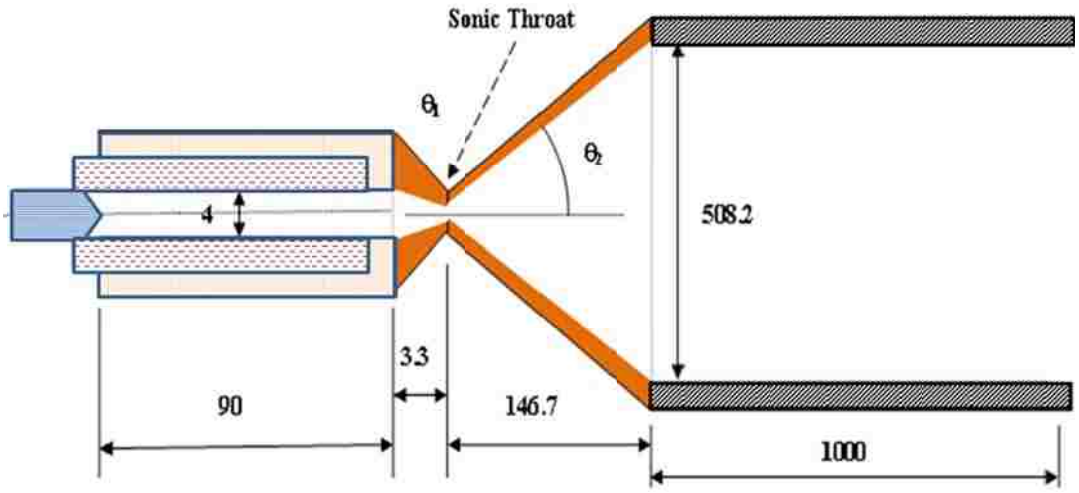


**Figure 4.1** Supersonic throat transition between the capillary and the expansion regions, $\theta_1=2^o$ and $\theta_2=60^o$, dimensions in mm (not to scale) [1]

The capillary source simulates hard disruption events by depositing transient radiant high heat flux onto the inner liner of the capillary, which in turn generates particulates from wall evaporation [2, 3]. The particulates form a plasma jet, which moves towards the capillary exit at high speed and high pressure. The capillary serves as a source term simulating surface erosion of the divertor of a tokamak fusion reactor under hard disruption-like conditions [4, 5]. The plasma jet expands into the vacuum vessel, which is simulated herein by the expansion large chamber. The nozzle, converging-diverging, is a method to allow for the computational transition between the capillary exit and the entry of the expansion chamber [1]. The capillary has an inner diameter of 4.0 mm diameter and 12 cm in length with 3.0 cm occupied by the discharge cathode. The discharge time is in the range of 100–200 μs and can be extended to few milliseconds. The produced plasma jet has typical temperature of up to 5 eV, an exit peak pressure of up to 400 MPa and imparts a radiant heat flux up to 60 GW/m$^2$ [3].

In the previous work, it has been shown that the Mach number at the diverging exit drops from 21 to 0.7 after suffering from multiple shocks in the large expansion volume, and

that the plasma parameters are almost constant along the axis of the simulated expansion chamber [1]. It was also shown that the Mach number is a function of the ratio $\left(A^{'} / A^{*}\right)$, where $A^{'}$ is the cross-sectional area along the length of the transition region at any location and $A^{*}$ is the sonic throat cross-sectional area. Thus, the variation of *Mach* number along the axis of the transition region, as well as inside the expansion chamber, does not depend on the values of the exit parameters of the capillary source. It has also been observed that two shocks successively take place as soon as the supersonic flow enters into the uniform cross section expansion chamber and brings the flow into sub-sonic steady state. The shock waves result from the sudden restriction in the cross-sectional area through which the plasma flows when the diverging section of the transition region opens into the expansion chamber. The present work introduces a mathematical formalism of a shock pitch length $Z_{sp}$, which is the spatial separation between successive shocks. It is an intuitively chosen variable, which if measured in an actual capillary discharge, can be used to produce the actual profile of the plasma bulk temperature, density, pressure and velocity.

### 4.2 Discretization Technique and Mathematical Formulation

As previously shown in the previous work, the relation between then cross-sectional area of the sonic throat $A^{*}$ and inlet cross section to the converging section *A,* is given by the well-known equation, which was used to establish the relationship between the plasma parameters and the Mach number along the cross-sectional area ($A'$) at any location along the length of the transition region [1, 6, 7]:

$$A^{*} = A\, M_{a} \left[ \frac{1 + \left( \frac{\gamma - 1}{2} \right) M_{a}^{2}}{\left( \frac{\gamma + 1}{2} \right)} \right]^{-\frac{(\gamma+1)}{2(\gamma-1)}} \tag{4.1}$$

Where $M_a$ is the Mach number at the capillary exit and $\gamma = C_p / C_v$ is the specific heat ratio. The plasma parameters at any axial location inside the transition nozzle are given by the following set of equations [1, 4, 5]:

$$\left.\begin{aligned} \rho' &= \rho \frac{\left[1+0.5(\gamma-1)(M_a)^2\right]^{\frac{1}{\gamma-1}}}{\left[1+0.5(\gamma-1)(M_a')^2\right]^{\frac{1}{\gamma-1}}}, \qquad P' = P \frac{\left[1+0.5(\gamma-1)(M_a)^2\right]^{\frac{\gamma}{\gamma-1}}}{\left[1+0.5(\gamma-1)(M_a')^2\right]^{\frac{\gamma}{\gamma-1}}} \\ T' &= T \frac{1+0.5(\gamma-1)(M_a)^2}{1+0.5(\gamma-1)(M_a')^2}, \qquad v' = M_a' \left(\frac{\gamma P'}{\rho'}\right)^{1/2} \end{aligned}\right\} \quad (4.2)$$

The units for the plasma parameters are in eV for the temperature, kg/m$^3$ for the density, MPa for the pressure and m/s for the velocity.

To obtain scaling laws for the converging-diverging transition nozzle and beyond, all equations have been discretized in one dimensional space along the axial direction so that one can retrieve the flow parameters at some preferred locations.

In this 1-D approach, it is assumed that there is no radial variation in the parameters and only axial grids are considered. The length of the converging, diverging and the expansion chamber are 0.33, 14.67 and 100 cm, respectively, hence the grid-size is not uniform. Grid-size has been varied in the three separate sections to reflect the changes in the parameters in each section.

In the converging section the successive nodes are separated by a distance of 0.2 mm, whereas in the diverging section the successive nodes are separated by a distance of 5 mm. So essentially there are roughly 16 nodes in the converging section and 29 nodes in the diverging section. In the diverging section more number of nodes has been incorporated because this section deals with the actual supersonic flow. On the other hand, in the 100cm long expansion chamber, the grid is much coarser as the successive nodes are separated by a distance equal to shock pitch length $z_{sp}$. For computational purposes it was assumed that $z_{sp}$=1cm, so this region essentially has 100 nodes. This also means that the successive shocks are separated by 1cm at the entry of the expansion chamber, which is the grid scale length. This assumed length approximately emulates the shape of the parameter profiles, but actual

scale lengths can be determined using proper sensing and imaging techniques in different sections of the experimental setup. Nevertheless, in this work the relative dimensions, or in other words the aspect ratios have been chosen realistically, pertinent to disruption events associated with divertor in a practical fusion reactor, e.g. ITER.

In our previous work, a stand-alone routine had been created to simulate the shock [1]. The Mach number, temperature, pressure and density at the diverging exit of the transition region were used there as the input to the shock routine. The routine checks the Mach number and decides whether to use the normal shock or the oblique shock. In case of the oblique shock the shock angle is estimated using one of the scaling laws prescribed in that work. In the present formalism, equations were established describing flow parameters only as a function of axial position with respect to the micro-nozzle exit.

For each of the flow parameters, namely plasma bulk velocity ($V_p$), plasma temperature ($T$), plasma bulk density ($\rho$), plasma pressure ($P$); linear fit was used in the region $0 \le Z \le 0.004\ meter$ (where $Z$ is a variable that represents the axial length traversed by the flow); whereas power-law fit was used for the region $0.004 \le Z \le 0.15\ meter$ and this power law fit takes care of the non-linearity in the respective parameter profiles as the flow becomes supersonic.

As the flow enters the expansion chamber of uniform cross section, it suffers from shock. It has been assumed that the changes in respective parameter values due to shock takes place over a small scale length, which in this case is the shock pitch length. This enables the tracking of the abrupt changes in the values of the flow parameters due to the shock in a reasonably gradual manner without changing the major profile features, giving the observer an opportunity to represent the parameter profiles as smooth functions of the axial length inside the expansion chamber in the steady-state subsonic condition.

For all the flow parameters, an easy to implement approach has been used to model the respective profiles inside the expansion chamber. Using the parameter values at the diverging exit and the values obtained right after the first shock, a linear fit equation was established, which predicts the variation of the profile parameters in the region $0.15 < Z \le (0.15 + Z_{sp})\ meter$ , where $Z_{sp}$ is the shock pitch length. A quadratic fit was used for the region for the region $(0.15 + Z_{sp}) \le Z \le (0.15 + 2Z_{sp})\ meter$ **,** using the parameter values at the

diverging exit and the values obtained at the end of each of the two shocks. It is to be noted that capillary exit dataset corresponding to shot # P 206 has been taken as the standard while formulating these scaling laws [3].

The flow parameters at the micro-nozzle outlet have been defined as $P(0)=P_e$ (in MPa), $T(0)=T_e$ (in eV), $\rho(0)=\rho_e$ (in kg/m$^3$), $v_p(0)=v_{pe}$ (in m/s) and Ma(0)=Ma$_e$.

The scaling laws for each zone are as follows:

Scaling laws for the axial length range $0 \le z \le 0.004$ *meter*

$$\left.\begin{aligned} T_z &= T_e\left(1-93.68z\right) \\ \rho_z &= \rho_e\left(1-37.23z\right) \\ P_z &= P_e\left(1-120z\right) \\ Ma_z &= Ma_e\left(1+142.5z\right) \\ v_{\mathrm{p},z} &= v_{pe}(1+85.17z) \end{aligned}\right\} . \qquad (4.3)$$

Scaling laws for the axial length range $0.004 < z \le 0.15$ *meter*

$$\left.\begin{aligned} T_z &= 5.33\times10^{-4}\ T_e\ z^{-0.8} \\ \rho_z &= 0.07\ \rho_e\ z^{-0.27} \\ P_z &= 3.58\times10^{-5}\ P_e\ z^{-1.09} \\ Ma_z &= 45.32\ z^{0.404} \\ v_{p,z} &= 1.91\ v_{pe}\ z^{0.0024} \end{aligned}\right\} . \qquad (4.4)$$

Scaling laws for the axial length range $0.15 < z \le (0.15+z_{sp})$ *meter*

$$\left.\begin{aligned} T_z &= m_T\left(z-0.15\right)+T_{DE} \\ \rho_z\left(\mathrm{Z}\right) &= m_\rho\left(z-0.15\right)+\rho_{DE} \\ P_z\left(\mathrm{Z}\right) &= m_P\left(z-0.15\right)+P_{DE} \\ Ma_z(Z) &= m_{Ma}\left(Z-0.15\right)+Ma_{DE} \\ v_{p,z} &= m_v\left(z-0.15\right)+v_{DE} \end{aligned}\right\} \qquad (4.5)$$

Where $m_X=(X_{s1}-X_{DE})/z_{sp}$ , $X_{DE}=X\left(z=0.15m\right)$, and $X\ is \equiv T,\rho,P,v_p,Ma$ .

Scaling laws for the range $\left(0.15+z_{sp}\right)m < z \le (0.15+2z_{sp})$ *meter*

$$\left.\begin{aligned} T_z &= A_T z^2 + B_T z + C_T \\ \rho_z &= A_\rho z^2 + B_\rho z + C_\rho \\ P_z &= A_p z^2 + B_p z + C_p \\ v_{p,z} &= A_v z^2 + B_v z + C_v \\ Ma_z &= A_{Ma} z + B_{Ma} \end{aligned}\right\}, \qquad (4.6)$$

Where $A_X = \left(X_{s2} - 2X_{s1} + X_{DE}\right)/2z_{sp}^2$,

$$B_X = \left[2z_{sp}\left(X_{s2} - X_{s1}\right) - 3\left(X_{s2} - 2X_{s1} + X_{DE}\right)\left(0.1 + z_{sp}\right)\right]/2z_{sp}^2,$$

$$C_X = X_{DE} - 0.0225\, A_X - 0.15\, B_X \text{ and } X \; is \equiv T, \rho, P, v_p$$

$$A_{Ma} = (Ma_{s2} - Ma_{s1})/z_{sp},\; B_{Ma} = Ma_{s1} - \left(z_{sp} + 0.15\right)A_{Ma}.$$

Scaling laws for the range $z > (0.15 + 2z_{sp})$ *meter*

$$\left.\begin{aligned} T_z &= T_{s2} = 0.825\; T_e \\ \rho_z &= \rho_{s2} = 0.28\; \rho_e \\ P_z &= P_{s2} = 0.23\; P_e \\ Ma_z &= Ma_{s2} = 0.7073 \\ v_{p,z} &= v_{s2} = 11.9\; v_{Pe} \end{aligned}\right\}, \qquad (4.7)$$

And $T_{s1} = 0.23T_e, \rho_{s1} = 0.195\rho_e, P_{s1} = 0.045P_e, v_{s1} = 1.7v_{pe}, Ma_{s1} = 1.9$.

The parameters $T_{s1}, \rho_{s1}, P_{s1}, v_{s1}, Ma_{s1}$ are the plasma temperature, pressure, bulk density, bulk velocity and Mach number, respectively, just after the first shock. The parameters $T_{s2}, \rho_{s2}, P_{s2}, v_{s2}, Ma_{s2}$ are the steady state values of plasma temperature, pressure, bulk density, bulk velocity and Mach number, respectively, of sub-sonic flow inside the expansion chamber.

One important aspect, that needs to be addressed while making the scaling formulae, is the continuity in the parameter profiles. The virtual regions created for computational convenience should merge smoothly, without exhibiting any anomaly, abrupt change or discontinuous graphical behavior.

## 4.3 Results and Discussion

It was previously mentioned that shot P206 has been taken as the standard while formulating the scaling laws, which has peak discharge current of $I_{p\ (P206)}$ =42.81kA . Four more peak discharge currents were chosen for the calculations based on this discharge current value. They are a factor of 0.5, 0.67, 1.5 and 2.0 of the P206 ($I_{p\ (P206)}$ =42.81kA), which makes all in comparison with P206. The ETFLOW code [3, 8, 9] was run for all these current values to obtain the respective capillary exit parameters. The capillary exit parameters for each value of the peak discharge current are show in Table 4.1 as given by the results of the ETFLOW code [3]. The calculated plasma parameters at the source exit are consistent with reported values [10, 11].

**Table 4.1:** Capillary exit parameters for the chosen values of discharge current

| Peak current (kA) | $I_p / I_{p\ (P206)}$ | $\rho$ (kg/m$^3$) | *P (MPa)* | *T (eV)* | $v_{bulk}$ *(m/s)* | Mach number (*Ma*) |
|---|---|---|---|---|---|---|
| 21.405 | 0.50 | 5.81880 | 153.23 | 2.152 | 5443.46 | 0.5442 |
| 28.540 | 0.67 | 7.77400 | 226.39 | 2.345 | 5733.19 | 0.5450 |
| 42.810 | 1.00 | 8.60100 | 386.00 | 2.627 | 6160.00 | 0.5397 |
| 64.215 | 1.50 | 17.9588 | 703.93 | 2.976 | 6598.97 | 0.5407 |
| 85.620 | 2.00 | 24.0853 | 1060.08 | 3.265 | 6994.07 | 0.5408 |

As can be seen from Table 4.1, the Mach number of the plasma bulk at the exit of the pulsed electrothermal plasma source (PEPS) is almost independent of the magnitude of the peak discharge current. This Mach number at the source exit is the input into the converging-diverging nozzle where the Mach number will be a function of the geometry.

Figure 4.2 shows the Mach number along the axis with respect to the geometry of the transition region and expansion chamber, and it is the same for all discharge current values. It is changing along the axial direction increasing up to a very high-hypersonic value ~21 at the diverging exit, then after the first shock it comes down to 1.9 and the second shock brings the

bulk plasma flow to a steady-state sub-sonic condition of Mach number ~ 0.707 inside the expansion chamber. The Mach number at the source exit is typical to the calculated values in similar systems and the pattern in the expansion is also similar to that expected in thrusters with diverging nozzles [11]. The pattern and the values of the Mach number into the expansion chamber are also consistent with recent 2-D modeling results and are in good correlation to experiment [12].

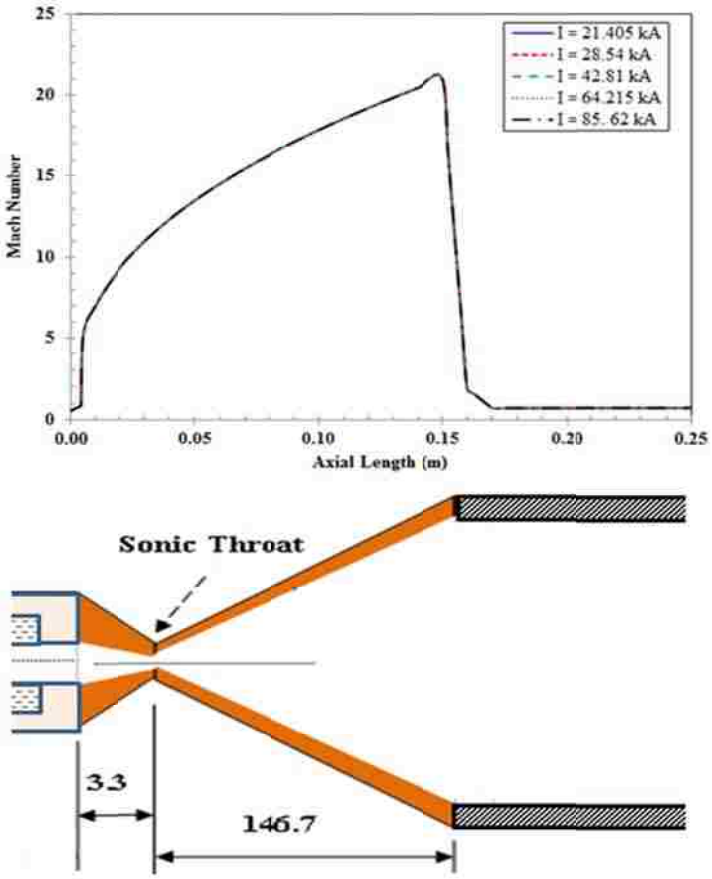


**Fig. 4.2** Mach number with respect to the geometry of the transition and expansion chamber

The plasma bulk density at the source exit increases with the increase in the magnitude of the discharge current [3]. This is also seen in Table 4.1 where the density increases from 5.8188 to 24.0853 kg/m$^3$ for peak currents of 21.405 to 85.62 kA, respectively. As the flow moves into the converging-diverging nozzle and the Mach number

increases, the bulk density drops down as seen in Fig. 4.3. The newly developed scaling law predicts 0.6837 to 2.82 kg/m$^3$ at the diverging exit for peak currents of 21.405 to 85.62 kA, respectively. As the flow suffers from shock and becomes sub-sonic inside the expansion chamber, the bulk density tends to increase. However the steady-state subsonic flow bulk densities are lower in magnitude compared to those estimated at the capillary exit. The scaling law predicts sub-sonic flow bulk densities of 1.6216 to 6.712 kg/m$^3$ for peak currents of 21.405 to 85.62 kA, respectively.

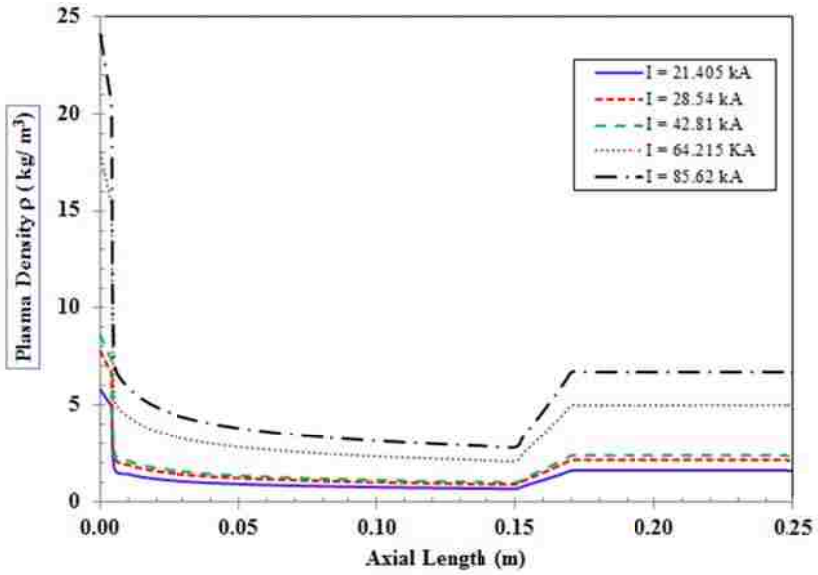


**Fig. 4.3** Plasma density versus the length of the transition and chamber regions

Because plasma pressure is directly proportional to the plasma bulk density, the pressure must increase with the increase in the magnitude of the discharge current [2, 3]. The source exit pressure as calculated by ETFLOW ranges from 153.23 to 1060.08 MPa for the tested range of the peak discharge currents. Figure 4.4 illustrates the plasma pressure along the axial length of the transition region and the expansion chamber. The pressure drops drastically in the converging-diverging nozzle as the Mach number increases. The scaling law predicts 43.3 to 299.9kPa at the diverging exit over the tested range of the discharge current. The flow becomes sub-sonic inside the expansion chamber and rises to reach steady-state at 35.25 to 243.83 MPa for the tested range of the discharge current. This behavior is also consistent with other reported studies [11-13].

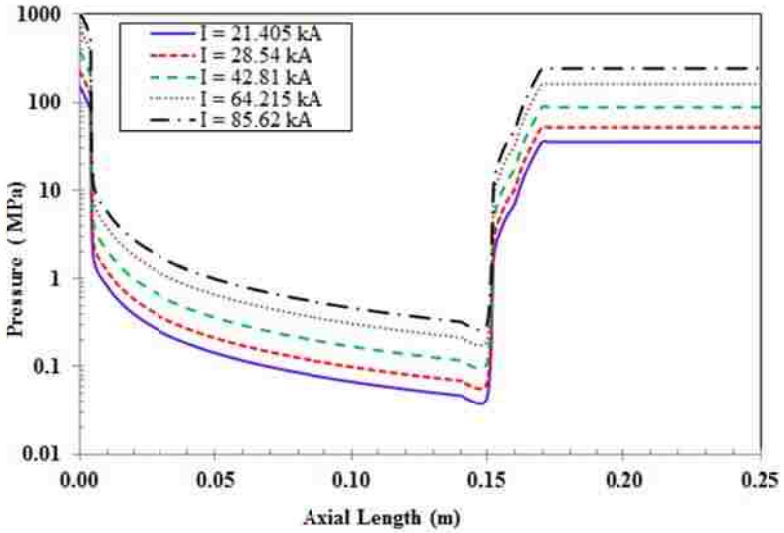


**Fig. 4.4** Plasma pressure versus the length of the transition and chamber regions

The plasma bulk velocity at the source exit as calculated by the ETFLOW code ranges between 5.443 to 6.994 km/s for the tested range of the discharge current, where all the values are consistent with reported values [3, 8-13], and the measured value of 5.333 km/s using a high speed camera on the an experimental electrothermal facility [14]. Figure 4.5 shows the plasma bulk velocity versus the length of the transition and chamber regions. The plasma bulk velocity increases rapidly inside the converging-diverging nozzle and then saturates to almost a steady-state value inside the expansion chamber. The scaling law predicts plasma bulk velocity between 10.36 to 13.31 km/s for the tested range of discharge current at the diverging exit, then drops inside the expansion chamber to 6.48 – 8.33 km/s for the same range of the discharge current,

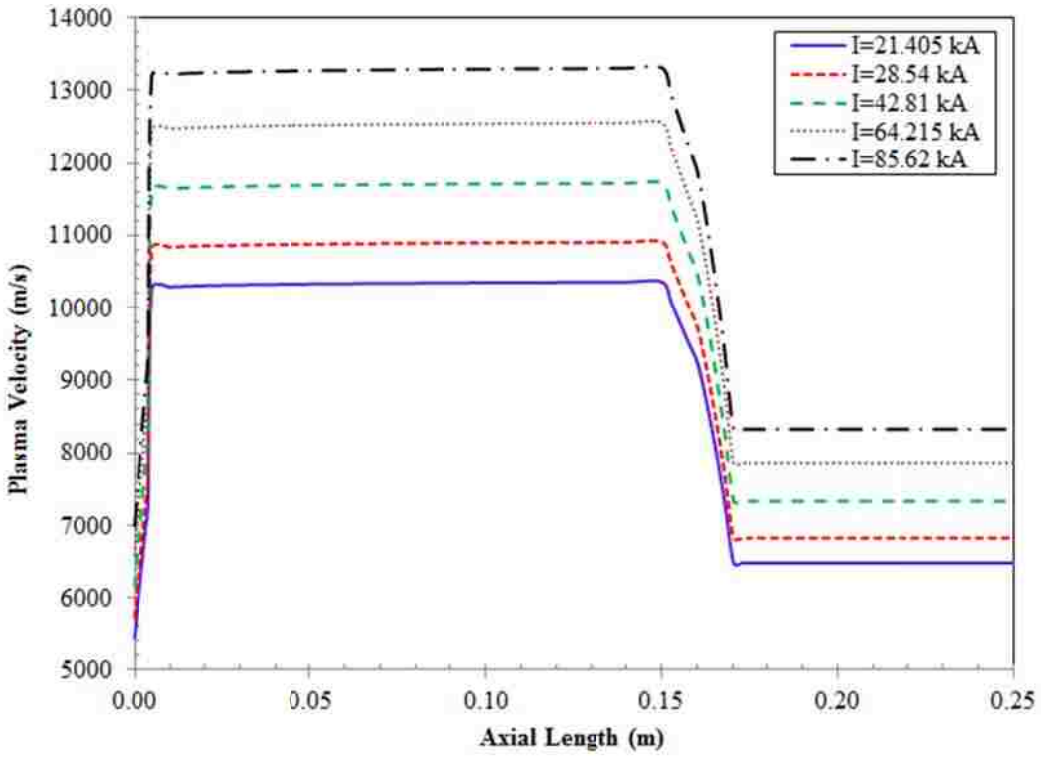


**Fig. 4.5** Plasma velocity versus the length of the transition and chamber regions

The plasma temperature at the source exit, as calculated by the ETFLOW code, ranges between 2.15 to 3.27 eV for the tested range of the discharge current, which is consistent with reported values [3, 8-13], and the measured value via optical emission spectroscopy [14]. Figure 6 shows the plasma temperature along the axis of the transition and chamber regions. Plasma bulk temperature follows a profile that is very similar to that of pressure and bulk density. Plasma temperature rapidly decreases inside the converging-diverging nozzle down to about 0.0053 to 0.008 eV at the diverging exit for the tested range of discharge current, then rises inside the expansion chamber to 1.78 -2.69 eV for the same range of the discharge current and remains almost constant.

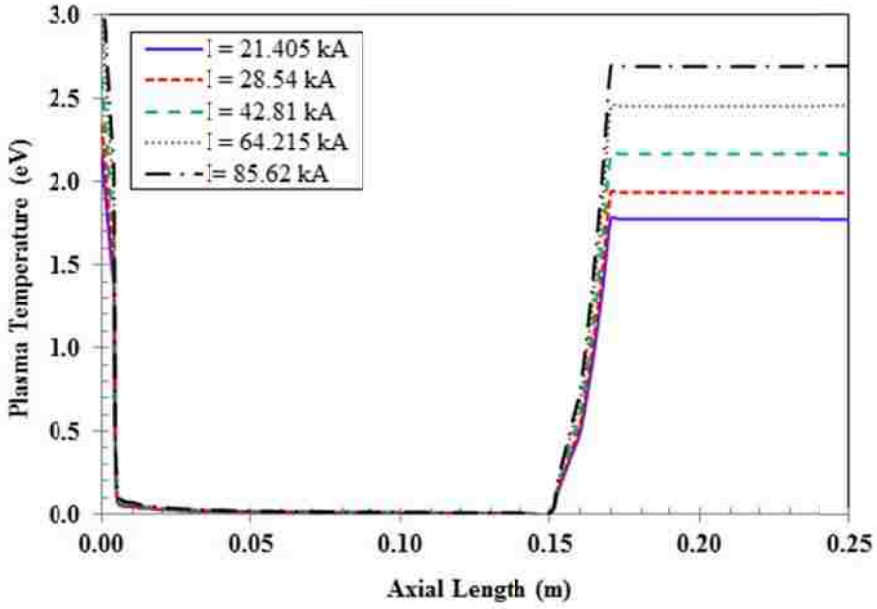


**Fig. 4.6** Plasma temperature versus the length of the transition and chamber regions

## 4.4 Conclusions

The developed scaling laws proposed in this work for fixed dimensions of the converging-diverging nozzle attached to an electrothermal plasma capillary source have shown efficient predictions of the plasma parameters over a tested range of discharge current from 21.405 to 85.62 kA. A change in the geometry and dimensions of the converging-diverging transition region will require adjustment to the power law in the supersonic region and subsequent changes in the scaling of post-shock as well as the steady-state subsonic flow parameters must also be taken care of. The predicted plasma parameters and the flow pattern are similar to reported results. Plasma temperature and velocity are consistent with values measured on an electrothermal facility, and are within reasonable correlation to published computational values. The plasma parameters suffer from drastic changes in the converging-diverging nozzle with increase in the Mach number and bulk velocity, and decrease in plasma density, pressure and temperature. However, all parameters converge to steady-state values inside the expansion chamber.

## 4.5 References


[1] R. Majumdar, J.G. Gilligan, A.L. Winfrey and M.A. Bourham, Supersonic flow patterns from electrothermal plasma source for simulated ablation and aerosol expansion following a fusion disruption, J. Fusion Energy, **33**(1), 25-31 (2014).

[2] J.D. Powell and A.E. Zielinski, Capillary discharge in the electrothermal gun, IEEE Trans. Magnetics, **29**(1), 591–596 (1993).

[3] L. Winfrey, J. Gilligan, A. Saveliev, M. Abd Al-Halim and M. Bourham, A study of plasma parameters in a capillary discharge with calculations using ideal and non-ideal plasma models for comparison with experiment, IEEE Trans. Plasma Science, **40**(3), 843-852 (2012).

[4] J. Gilligan and M. Bourham, The use of an electrothermal plasma gun to simulate the extremely high heat flux conditions of a tokamak disruption, J. Fusion Energy, **12** (3), 311-316 (1993).

[5] J.P. Sharpe, B.J. Merrill, D.A. Petti, M.A. Bourham and J.G. Gilligan, Modeling of particulate production in the SIRENS plasma disruption simulator, J. Nuclear Materials, **290**, 1128-1133 (2001).

[6] J.E.A. John and T.G. Keith, *Gas Dynamics,* 3rd Edition, Pearson Education, Upper Saddle River, NJ, 2005.

[7] R.D. Zucker and O. Biblarz, Fundamentals of Gas Dynamics, 2nd Edition, John Wiley & Sons, Inc., 2002.

[8] M.A. Abd Al-Halim and M.A. Bourham, Characterization of short intense pulsed electrothermal plasma capillaries for use as fusion and launchers heat flux sources, J. Fusion Energy, **33**(3), 258-263 (2014).

[9] J.R. Echols and A.L. Winfrey, Ablation of fusion materials exposed to high heat flux in an electrothermal plasma discharge as a simulation for hard disruption, J. Fusion Energy **33**(1), 60-67 (2014).

[10] K. Kim, Time-dependent one-dimensional modeling of pulsed plasma discharge in a capillary plasma device, IEEE Trans. Plasma Sc., **31**(4), 729-735 (2003).

[11] T. Edamitsu and H. Tahar, Experimental and numerical study of an electrothermal pulsed plasma thruster for small satellites, Vacuum, **80**, 1223–1228 (2006).

[12] M.J. Esmond and A.L. Winfrey, Inspection of the flow characteristics of electrothermal plasma discharges using a two-dimensional fluid model, 21st Topical Meeting on the Technology of Fusion Energy (TOFE), Anaheim, CA, 9-13 November 2014.

[13] K. Kim and D. Peterson, A low aspect ratio electrothermal gun for metal plasma vapor discharge and ceramic nanopowder production, J. Mech. Sc. & Technol. **22**, 1408-1416 (2008).

[14] M.H. Hamer, Design of optical measurements for electrothermal plasma discharges, MS Thesis, Virginia Polytechnic Institute and State University, 2014.

# 5

# Effect of Temperature and Nonlinearity of Adiabatic Compressibility Index on 1-D Supersonic bulk flow of the polycarbonate plasma

*Published in J. Fusion Energy: "*Effect of Plasma Temperature and Nonlinearity of the Adiabatic Compressibility Index on Flow Parameters for Hypersonic Aerosol Expansion Following a Plasma Disruption*", Rudrodip Majumdar and Mohamed A. Bourham, J. Fusion Energy, Published online 27 June 2015, DOI:* 10.1007/s10894-015-9960-1.

Future fusion reactors are expected to experience hard current disruptions that quench the confined plasma and deposit the energy on the plasma facing materials, thus causing surface ablation and the evolving aerosol expands into the reactor chamber. The plasma flow following a disruption event can be simulated experimentally and computationally using confined capillary discharges, which generate heat fluxes (up to ~80 GW/m$^2$) typical to those expected in fusion reactors during a disruption. Computational technique to investigate the effect of plasma temperature on the adiabatic compressibility index has been investigated using a pulsed disruptive capillary electrothermal plasma source with a converging-diverging transition nozzle at the exit attached to the expansion regions. The plasma is formed in the capillary due to thermal decomposition of the ablating inner wall followed by subsequent ionization of the decomposed material. This work is particular to the cases where the ejected particulates coming out from a heat-load affected surface or arc-triggered plasma source orifice are at the sonic speed. The converging section in the nozzle provides a transition from the capillary exit subsonic condition to sonic state, which allows for observing the effect of temperature on the supersonic isentropic expansion. Mathematical model has been developed for effective atomic number ($Z_{eff}$) as function of the plasma temperature and has been used to model the adiabatic compressibility index ($\gamma_p$) of the plasma. Plasma parameters along the axial direction of the flow in the transition and the expansion regions are obtained.

## 5.1 Introduction

Pulsed electrothermal (ET) plasma devices have significant experimental impact over a range of power levels and various important applications such as launch devices [1,2], pellet accelerators for fusion fueling [3,4], source of high heat flux for material studies [5-7 ], space propulsion and thrusters [8-10], and as systems for surface deposition and coatings [11-13]. The ET devices are often described as attractive low-power thrusters due to their small dimensions, simplicity, and ability to provide high specific impulses at low power levels **[**14,15**].**

Although considerable amount of research effort has been put in the study of problems related to the capillary discharges, the effect of temperature on the bulk flow parameters, for plasma jets opening into larger volume of free space has not been thoroughly investigated. Development of mathematical model that represents adiabatic compressibility index ($\gamma_p$) of the plasma jetting out a capillary discharge as a function of the plasma bulk temperature is needed in order to perform computational study on the effect of temperature on the flow parameters associated with a supersonic micro-jet expanding to a much larger volume. It is important to consider other attributes, such as some typical electron impact dissociation energies as well as a mathematical model for $Z_{eff}$ for the capillary wall material due to the fact that the mathematical formulation is not necessarily very straightforward. The effective atomic number for the bulk plasma generated from the ablation of the capillary sleeve material is a function of the plasma temperature.

In this work a mathematical model has been prescribed for effective atomic number and has been utilized to modify the specific heat ratio of the arc ablated plasma as the plasma temperature changes. The work is specific to Lexan polycarbonate ($C_{16}H_{14}O_3$) as the sleeve material, which has 254.3 g/mol average molecular weight of repeat unit, 1.2g/cm$^3$ specific gravity, and 73.1 eV mean excitation energy [16]. The generated plasma is carbon-hydrogen-oxygen plasma when fully dissociated and a combination of molecular forms of the constituents when partially dissociated. The current investigation uses the same system configuration that has been used, as shown in Fig. 5.1 and previously described in detail in our earlier work **[**17,18**].**

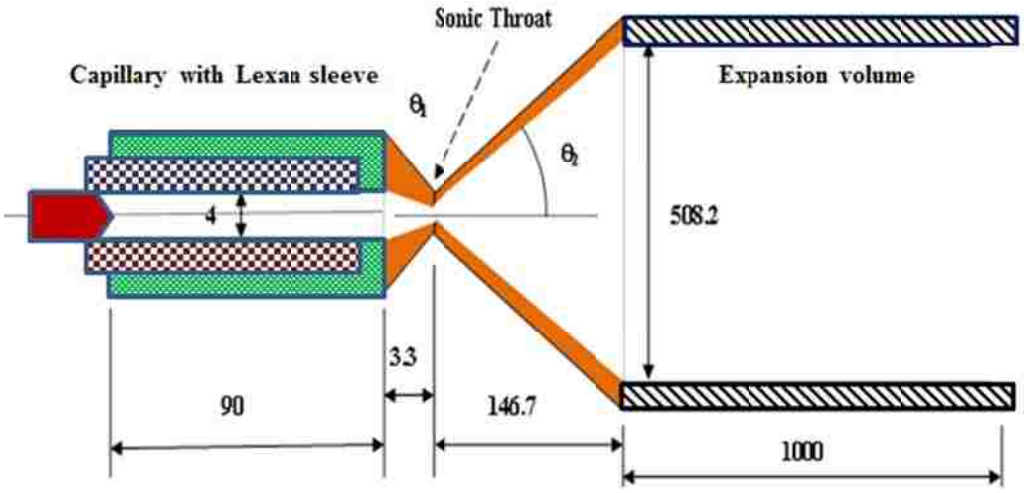


**Fig. 5.1** Configuration of the pulsed capillary source with supersonic throat transition to an expansion volume (not to scale) [17,18]

## 5.2 Computational Modeling of $Z_{eff}$ and $\gamma_p$

In order to develop a mathematical model for $Z_{eff}$ as a function of the plasma jet bulk temperature for polycarbonate material, it was essential to investigate the range of $Z_{eff}$ available from the literature, as there is scarcity of information on the effective atomic number of Lexan as a function of temperature. To obtain a reasonable value for Lexan, it was reasonable to first look at the average values for some plastic resins from published data. Acrylic ($C_5H_8O_2$) has a value of 6.47, polymethylpentene (*PMP* – $C_6H_{12}(CH_2)$ is *5.44 and* polystyrene ($C_8H_8$) is 5.69; all are true $Z_{eff}$ values and close enough to the average measured values [19]. An average value for Lexan polycarbonate ($C_{16}H_{14}O_3$) is an average of $6.48 \pm 1.38$ for conventional polycarbonate resin, based on calculations and measurements of similar polymer resins. In modeling $Z_{eff}$ one utilizes the fact that as the bulk temperature rises, the outer electrons are knocked off, resulting in lesser amount of shielding as seen by an electron approaching towards the ion/radical. Thus with increasing temperature, the effective atomic number of an ablated polycarbonate chunk/radical should increase in the lower energy range up to several eV. The study performed by Singh in 2002 on $Z_{eff}$ of body tissues and amino acids with composition like $C_5H_9NO_2$, $C_6H_{12}N_2O_4S4$ and $C_{11}H_{12}N_2O_2$, similar to polymeric compounds, has shown that

$Z_{eff}$ will increase with the increase in the energy from photoelectric effect [20]. The study of the effective atomic numbers for some low-z materials has shown $Z_{eff} = 5.374$ for polycarbonate at lower energies, which is close to the value of 6.48 previously mentioned [21]. Hence, it is with confidence to consider the value $6.48 \pm 1.38$ as an average $Z_{eff}$ for conventional polycarbonate resin. It should be noted that $Z_{eff}$ drops with increased energies in the 0.01-0.1 MeV range and stays almost constant for higher energies above several MeV [21].

Although Lexan polycarbonate decomposes at lower temperatures than that of electrothermal plasma in a capillary discharge, however, the individual effective atomic numbers for the products formed due to the decomposition of the polycarbonate material is not considered in this work but a lumped form of $Z_{eff}$ has been used which assumed inclusion of all possible major aspects. The typical graphical profile of $Z_{eff}$ for traditional gases has been embedded in the model as plasma in the capillary discharge is essentially a hot partially ionized gas. Usually for common gases $Z_{eff}$ remains fairly constant at low temperatures, which is followed by a steep rise within a certain temperature range, and exhibits a trend of saturation at very high temperatures [21]. Numerical values of $Z_{eff}$ as a function of plasma temperature are tabulated in Table 5.1, and is also plotted in Fig. 5.2 with additional power fit $Z_{eff} = 6.65\, T_p^{0.0825}$ covering the temperature range ($0.03\text{eV} \leq T_p \leq 10\text{ eV}$). This power fit has been used to model the adiabatic compressibility index with the limits $Z_{eff}$ ($T_p$<0.03eV) = $Z_{eff}$ (at $T_p$=0.03 eV) and $Z_{eff}$ ($T_p$ >10 eV) = $Z_{eff}$ (at $T_p$=10eV)

**Table 5.1** $Z_{eff}$ as a function of plasma temperature for the lower temperatures 0.03-10eV

| **Plasma Temperature $T_p$** (eV) | ≤ 0.03 | 0.05 | 0.20 | 0.40 | 0.60 | 0.80 | 1.0 |
|---|---|---|---|---|---|---|---|
| $Z_{eff}$ | 5.25 | 5.40 | 5.65 | 5.85 | 5.95 | 6.10 | 6.48 |
| **Plasma Temperature $T_p$** (eV) | 1.30 | 1.80 | 3.50 | 6.50 | 8.50 | ≥ 10 | |
| $Z_{eff}$ | 6.96 | 7.23 | 7.58 | 7.86 | 8.08 | 8.2 | |

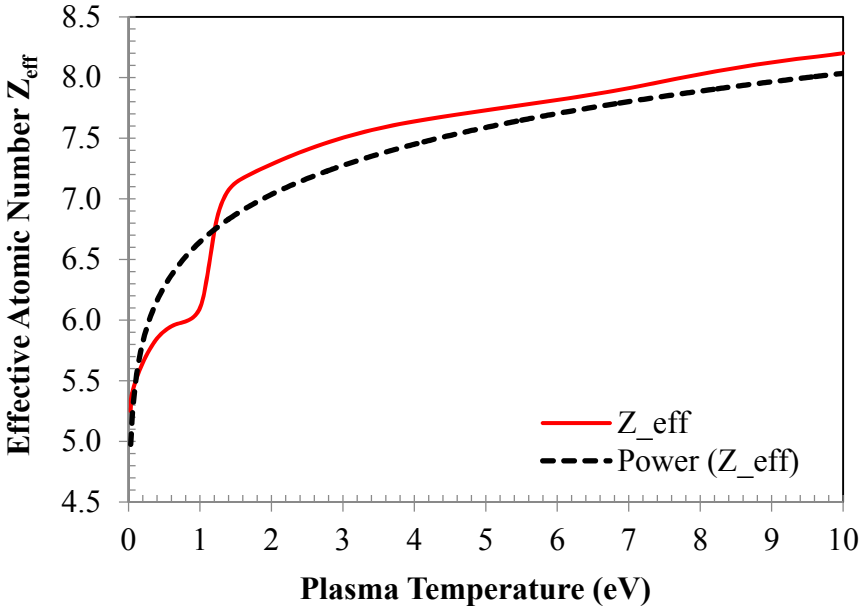


**Fig. 5.2** Calculated and power-fitted effective atomic number versus plasma temperature

Two quite similar but different mathematical models for plasma adiabatic compressibility index ($\boldsymbol{\gamma_p}$) are proposed herein. In the formulation of $\boldsymbol{\gamma_p}$, the electron-impact dissociation energies have been used for C-H and C=O bonds (both CO and $CO_2$ gases have been considered , as both of them are dominant products in the bulk plasma following the bond dissociation phase). This is along with some parametric constants, which essentially adds non-linearity to the model. When the ablated material in the capillary forms plasma from thermal dissociation and ionization of the polycarbonate sleeve cools down in the expansion region (transition region) then a major fraction of ions and free radicals are expected to recombine and essentially the cooled down gas mixture can be expected to be composed principally of CO and $CO_2$ gases. Consequently, the adiabatic compressibility index ($\boldsymbol{\gamma_p}$) will be dependent on these two gaseous forms. For the supersonic ultra-cold state, using a linear approximation, the specific heat ratio can roughly be estimated as $\boldsymbol{\gamma_p} \approx (\gamma_{CO} + \gamma_{CO_2})/2 = 1.35$. However, this is not perfect when nonlinearities are incorporated.

In general the adiabatic exponent or the specific heat ratio is expressed as the ratio of the isothermal compressibility to the isentropic compressibility. A few reported works has shown

that low–temperature, weakly ionized gas discharges predict very high adiabatic exponent at low temperatures and exhibits a decrease in the exponent as the plasma temperature rises [22]. Partially ionized very high density, high temperature, high pressure arc-ablated plasmas with different and distinct plasma flow regimes exhibit highly non-linear behavior. It is even more challenging in capillary sources as plasma exhibits isothermal behavior while the temperature is very high.

Adiabatic compressibility of a very dense fluid medium has been found to decrease with increasing density; and as the compressibility value decreases, $\boldsymbol{\gamma_p}$ increases. Dominant isothermal compressibility for high density, temperature and high pressure capillary plasmas leads to higher γ values. As the plasma enters the diverging section the isentropic adiabatic expansion happens, and the plasma temperature, density and pressure rapidly drop down. As the bulk density decreases, the adiabatic compressibility increases, resulting in a small value of $\boldsymbol{\gamma_p}$ in the supersonic expansion regime. Inside the expansion volume the bulk plasma flow reaches a subsonic steady-state condition after suffering from two successive shocks and another isothermal regime can be observed. The post shock temperature, density, pressure values rise to a considerably high value leading to a considerably high $\gamma_p$ value. While plasma fluid is still compressible in the expansion chamber but the flow reaches incompressible subsonic-steady state. Hence, the adiabatic exponent does not affect the steady-state flow pattern inside the expansion chamber. However, during the shocks the adiabatic exponent takes significant role in determining post-shock flow parameter values. At the temperature of interest, the $\gamma_p$ value will be dictated by the ions, free radicals and the traces of CO and $CO_2$ gas molecules dissociating from the ablated Lexan. The expression for the first model of $\gamma_p$ for the range $0.03\text{eV} \leq T_p \leq 10\text{ eV}$, and within the same limits $\gamma_p$ ($T_p$<0.03eV) = $\gamma_p$ (at $T_p$= 0.03 eV) and $\gamma_p$ ($T_p$ >10eV) = $\gamma_p$ (at $T_p$=10 eV), can be formulated with fractions of dissociated species based on their respective dissociation energy with respect to the plasma temperature, and can be written in the following form:

$$\gamma_p/(\gamma_p-1.35)=1.4+0.15\left[a_1\left(E_{CO_2}/T_p\right)^{a_2}+b_1\left(E_{CO}/T_p\right)^{b_2}+c_1\left(E_{C-H}/T_p\right)^{c_2}\right]/\left(1+Z_{eff}\right)^{d} \qquad (5.1)$$

where, $T_p$ is the plasma temperature in eV, $E_{C-H}$ is an approximation of average dissociation energy for C-H bond, $E_{CO_2}$ and $E_{CO}$ are the dissociation energies for C=O bonds of $CO_2$ and CO gas molecules (or free radicals), respectively, and $a_1, a_2, b_1, b_2, c_1, c_2, and\ d$ are parameters determined intuitively for each case as shown in Table 5.2 for four different study cases. This mathematical formulation for adiabatic compressibility index for arc-ablated polycarbonate plasma has been done with a reflection of the effect of plasma temperature and the non-linearity in the effective atomic number on the hypersonic expansion and bulk flow patterns. The non-linearity has been written on the right hand side of the equation in a way that the numerator contains the power-law terms that directly includes the bulk temperature, whereas the denominator contains the non-linearity in the effective atomic number. The available numerical values of the low-temperature electron impact bond dissociation energies for the relevant reactions that occur at a few electron volt plasma kinetic temperature are $E_{CO_2} = 5.451\ eV$, $E_{CO} = 11.109\ eV$ and $E_{C-H} = 4.48\ eV$ [23,24]. Figure 5.3 displays the variation of $\gamma$ with plasma temperature for Model-1, where the value can vary by as much as a factor of 3.12 relative to the minimum value ( Case 4).

**Table 5.2:** Non-linearity parameters for Model 1

| Non-linearity parameter | Case 1 | Case 2 | Case 3 | Case 4 |
|---|---|---|---|---|
| $a_1$ | 1.0 | 1.0 | 1.0 | 1.0 |
| $a_2$ | 0.1 | 0.3 | 0.9 | 1.0 |
| $b_1$ | 1.0 | 1.0 | 1.0 | 1.0 |
| $b_2$ | 0.1 | 0.3 | 0.9 | 1.0 |
| $c_1$ | 1.0 | 1.0 | 1.0 | 1.0 |
| $c_2$ | 0.1 | 0.3 | 0.9 | 1.0 |
| $d$ | 1.2 | 0.8 | 1.8 | 1.0 |

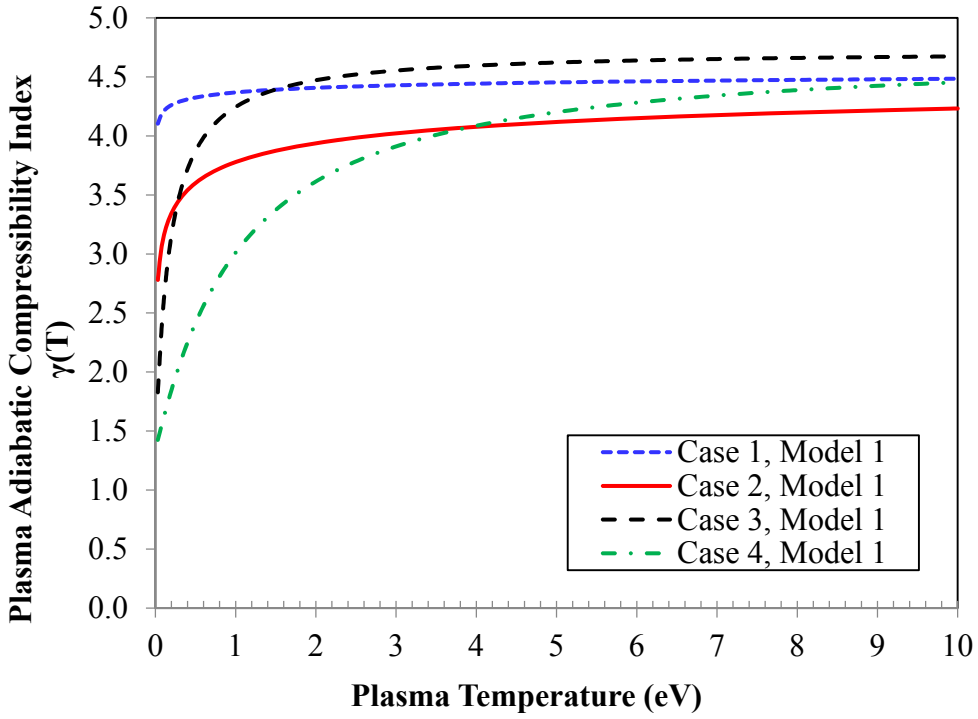


**Fig. 5.3** Change in plasma adiabatic compressibility index with change in plasma temperature (Model-1)

The second model of $\gamma_p$ is quite similar but parametrically a little different. Model 1 contains an exponent on the expression that contains $Z_{eff}$. The value of $\gamma_p$ depends more on a polynomial of $Z_{eff}$ for higher values of the parameter d; whereas Model 2 deals with a single degree of $Z_{eff}$ in the denominator of the expression. This essentially differentiates the two models in terms of the extent of non-linearity as well as non-ideality incorporated into each of them. The second model has been formulated within the temperature range ( 0.03 eV $\leq T_p \leq$ 10 eV), and within the same limits previously used for Model-1 $\gamma_p^*(T_p < 0.03\ eV) = \gamma_p^*(T_p = 0.03\ eV)$ and $\gamma_p^*(T_p > 10\ eV) = \gamma_p^*(T_p = 10\ eV)$ and can be written in the following form of Eq. 5.2 :

$$\gamma_p^* / (\gamma_p^* - 1.35) = 1.3 + 0.6\left[a_1\left(E_{CO_2}/T_p\right)^{a_2} + b_1\left(E_{CO}/T_p\right)^{b_2} + c_1\left(E_{C-H}/T_p\right)^{c_2}\right] / \left(1 + d_1 Z_{eff}^{d_2}\right) \quad (5.2)$$

where, $T_p$ is the plasma temperature in eV, $E_{C-H}$ , $E_{CO_2}$ and $E_{CO}$ are the bond dissociation energies as previously mentioned, and $a_1, a_2, b_1, b_2, c_1, c_2, d_1$ *and* $d_2$ are the associated non-

linearity parameters. Four different study cases are also presented for Model-2 and the nonlinearity parameters are tabulated in Table 5.3 for each case. Figure 5.4 displays the variation of $\gamma$ with plasma temperature for Model-2 where the value can vary by as much as a factor of 3.29 relative to the minimum value (Case 4).

**Table 5.3:** Non-linearity parameters for Model 2

| Non-linearity parameter | Case 1 | Case 2 | Case 3 | Case 4 |
|---|---|---|---|---|
| $a_1$ | 1.0 | 1.0 | 1.00 | 1.0 |
| $a_2$ | 0.01 | 0.2 | 0.25 | 1.1 |
| $b_1$ | 1.0 | 1.0 | 1.00 | 1.0 |
| $b_2$ | 0.01 | 0.2 | 0.25 | 1.1 |
| $c_1$ | 1.0 | 1.0 | 1.00 | 1.0 |
| $c_2$ | 0.01 | 0.2 | 0.25 | 1.1 |
| $d_1$ | 4.0 | 3.0 | 4.00 | 4.0 |
| $d_2$ | 0.7 | 0.8 | 0.30 | 2.5 |

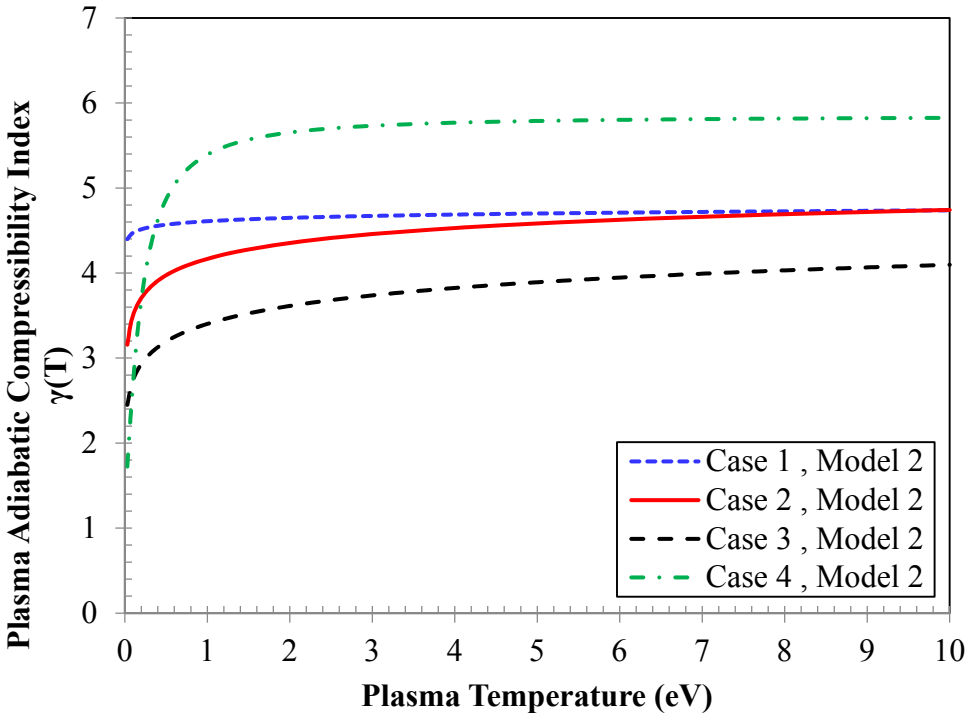


**Fig. 5.4** Change in plasma adiabatic compressibility index with change in plasma temperature (Model-2)

## 5.3 Formulation of Temperature-Dependent Governing Equations

It is important to determine the cross-section area of the sonic throat to establish a mathematical relationship between the Mach number and the flow area, which essentially establishes a relationship between the Mach number and the distance from the capillary exit into the transition region. The values of the parameters at the capillary exit are known, and the exit diameter of the capillary equals the inlet diameter of the converging section. Denoting $A$ as the area of cross-section at the capillary, $P$ the plasma pressure at exit, $V$ the plasma bulk velocity, $T_{exit}$ plasma temperature, $\rho$ the bulk density, $Ma$ capillary exit Mach number, $\gamma(T_{exit})$ the adiabatic compressibility index and $A^*$ the sonic throat area; a mathematical relationship between $A$ and $A^*$ can be written as follows:

$$A^* = A\, M_a \left[ \left\{ 1 + 0.5(\gamma_{T_{exit}} - 1) M_a^2 \right\} / \left\{ 0.5(\gamma_{T_{exit}} + 1) \right\} \right]^{-(\gamma_{T_{exit}}+1)/2(\gamma_{T_{exit}}-1)} \tag{5.3}$$

where $\gamma_{T_{exit}}$ can be estimated using either Model-1 or Model-2.

The value of $A^*$ can be used to generate mathematical formulae which describes Mach number as a function of the cross-section area ($A'$) of the transition region for the converging and diverging sections, taking care of subsonic and supersonic regimes separately [17]; enabling us to obtain the Mach number as a function of the distance from the capillary exit into the transition region [18]. Upon calculating the plasma temperature $T_p'$ using $T_p$ and the Mach number, the parameters at any position in the converging-diverging transition region can be computed. These parameters are shown in Eq. 5.4 below.

$$\left.\begin{aligned} T_p^{'} &= T_p \frac{1 + 0.5\left(\gamma_{T_p} - 1\right) Ma^2}{1 + 0.5\left(\gamma_{T_p} - 1\right) Ma^{'2}} \quad , \quad \rho^{'} = \rho \frac{\left(1 + 0.5\left(\gamma_{T_p} - 1\right) Ma^2\right)^{1/(\gamma_{T_p}-1)}}{\left(1 + 0.5\left(\gamma_{T_p}^{'} - 1\right) Ma^{'2}\right)^{1/(\gamma_{T_p}^{'}-1)}} \\ V^{'} &= Ma^{'} \left( \frac{\gamma_{T_p}^{'} P^{'}}{\rho^{'}} \right)^{1/2} \quad , \quad P^{'} = P \frac{\left(1 + 0.5\left(\gamma_{T_p} - 1\right) Ma^2\right)^{\gamma_{T_p}/(\gamma_{T_p}-1)}}{\left(1 + 0.5\left(\gamma_{T_p}^{'} - 1\right) Ma^{'2}\right)^{\gamma_{T_p}^{'}/(\gamma_{T_p}^{'}-1)}} \end{aligned}\right\} \tag{5.4}$$

where, $\gamma(T_p)$ is the adiabatic compressibility index as a function of plasma temperature. Using this set of equations one can compute the plasma pressure, plasma bulk velocity,

temperature and the density at the exit of the diverging section. In fact these values are also the input dataset for the shock model inside the uniform expansion volume. Upon obtaining the Mach number ($Ma_1$), pressure ($P_1$), density ($\rho_1$), velocity ($V_1$) and plasma temperature ($T_{p,1}$) at the exit of the diverging section, the mathematical expressions that describe normal and oblique shocks can be used to calculate post-shock plasma parameters such as Mach number ($Ma_2$), pressure ($P_2$), Temperature ($T_{p,2}$), density ($\rho_2$) and the bulk velocity ($V_2$). The flow will suffer a shock if the supersonic flow out of the diverging section suddenly enters a closed large volume, as the expansion chamber in this case. Flows with very high Mach numbers usually undergo oblique shock, and when the Mach number is quite small, normal shock occurs. Temperature correction has been incorporated into the specific heat ratio that goes into the shock equations. The mathematical expressions for the normal and oblique shocks are shown by equations (5.5) and (5.6), respectively.

For normal shocks:

$$\left.\begin{aligned} M_{a_2} &= \left[\left\{\left(\gamma_{T_{p,1}}-1\right)M_{a_1}^2+2\right\}/\left(2\gamma_{T_{p,1}}M_{a_1}^2-\gamma_{T_{p,1}}+1\right)\right]^{1/2} \\ T_{p,2} &= T_{p,1}\frac{\left[1+\ 0.5(\gamma_{T_{p,1}}-1)M_{a_1}^2\right]\left[\left\{2\gamma_{T_{p,1}}M_{a_1}^2/(\gamma_{T_{p,1}}-1)\right\}-1\right]}{M_{a_1}^2(\gamma_{T_{p,1}}+1)^2/2(\gamma_{T_{p,1}}-1)} \\ P_2 &= P_1\left[\frac{\gamma_{T_{p,1}}\left(2M_{a_1}^2-1\right)+1}{\left(\gamma_{T_{p,1}}+1\right)}\right] \\ \rho_2 &= \rho_1\left[\frac{\left(\gamma_{T_{p,1}}+1\right)M_{a_1}^2}{\left(\gamma_{T_{p,1}}-1\right)M_{a_1}^2+2}\right] \end{aligned}\right\} \qquad (5.5)$$

For oblique shocks:

$$\left.\begin{aligned} M_{a_2} &= \left[\frac{(\gamma_{T_{p,1}}-1)M_{a_1}^2 Sin^2\theta + 2}{2\gamma_{T_{p,1}}M_{a_1}^2 Sin^2\theta - \gamma_{T_{p,1}} + 1} Sin^{-2}(\theta-\delta)\right]^{1/2} \\ T_{p,2} &= T_{p,1}\frac{\left[2\gamma_{T_{p,1}}M_{a_1}^2 Sin^2\theta - \gamma_{T_{p,1}} + 1\right]\left[(\gamma_{T_{p,1}}-1)M_{a_1}^2 Sin^2\theta + 2\right]}{(\gamma_{T_{p,1}}+1)^2 M_{a_1}^2 Sin^2\theta} \\ P_2 &= P_1\frac{2\gamma_{T_{p,1}}M_{a_1}^2 Sin^2\theta - \gamma_{T_{p,1}} + 1}{\gamma_{T_{p,1}}+1} \\ \rho_2 &= \rho_1\frac{(\gamma_{T_{p,1}}+1)M_{a_1}^2 Sin^2\theta}{(\gamma_{T_{p,1}}-1)M_{a_1}^2 Sin^2\theta + 2} \\ V &= M_{a_2}\left(\frac{\gamma_{T_{p,2}}P_2}{\rho_2}\right)^{\frac{1}{2}} \end{aligned}\right\} \quad (5.6)$$

where, $\delta = Cot^{-1}\left[\left(\frac{\gamma_{T_{p,1}}+1}{2(M_{a_1}^2 Sin^2\theta - 1)}M_{a_1}^2 - 1\right)\tan\theta\right]$.

Here, $\theta$ is shock angle corresponding to bulk flow Mach number $Ma_1$ and $\delta$ is the subsequent deflection angle. Using the above set of formulae, that are related to shock, the values of the parameters of interest after successive shocks can be computed. The quadratic scaling law that expresses the shock angle as a function of Mach number, as prescribed in the previous work was utilized [17]. The deviation angle can be calculated by plugging the value of the shock angle $\theta$ into the $\delta$ expression.

## 5.4 Results and Discussion

The change in the Mach number along the length of the transition region is shown in Fig. 5.5, while the change into the length of the expansion chamber (expansion volume) is illustrated in Fig. 5.6. As seen from Fig. 5.5, Mach number at a certain location inside the converging-diverging nozzle is a strong function of the ratio of the area of cross-section of transition region at that location to the sonic throat area. As the sonic throat area is a function of the specific heat ratio, the Mach number profile may slightly vary for different cases of the models prescribed for $\gamma(T_p, Z_{eff})$. Figure 5.5 presents Mach number profiles for two cases of Model-2 that exhibit deviation from each other. Case 3 predicts a capillary exit subsonic condition with Mach number 0.478 and a supersonic condition at the diverging exit with Mach number 21.36, while these numbers in Case 4 are 0.385 and 21.69, respectively.

Although the deviation is quite small, yet it demonstrates the effect of temperature as well as non-linearities on the flow pattern.

After suffering from two successive shocks at the entry of the expansion chamber the flow becomes subsonic. It is found that for Model 2, the Mach numbers for the steady-state flow inside the expansion chamber for the four cases are 0.725, 0.697, 0.662 and 0.634, respectively. Although these values are close enough, still they bear the effect of temperature on the specific heat ratio. Figure 5.6 presents case 3 and case 4 to demonstrate the Mach number profiles inside the expansion chamber.

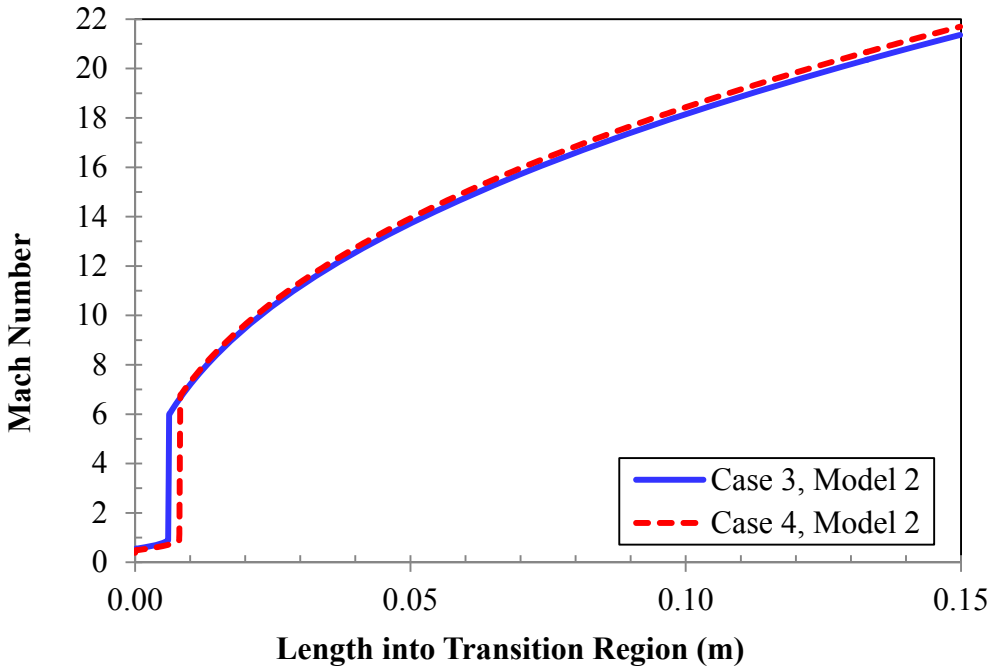


**Fig. 5.5** Change in the Mach number along the length of the transition region

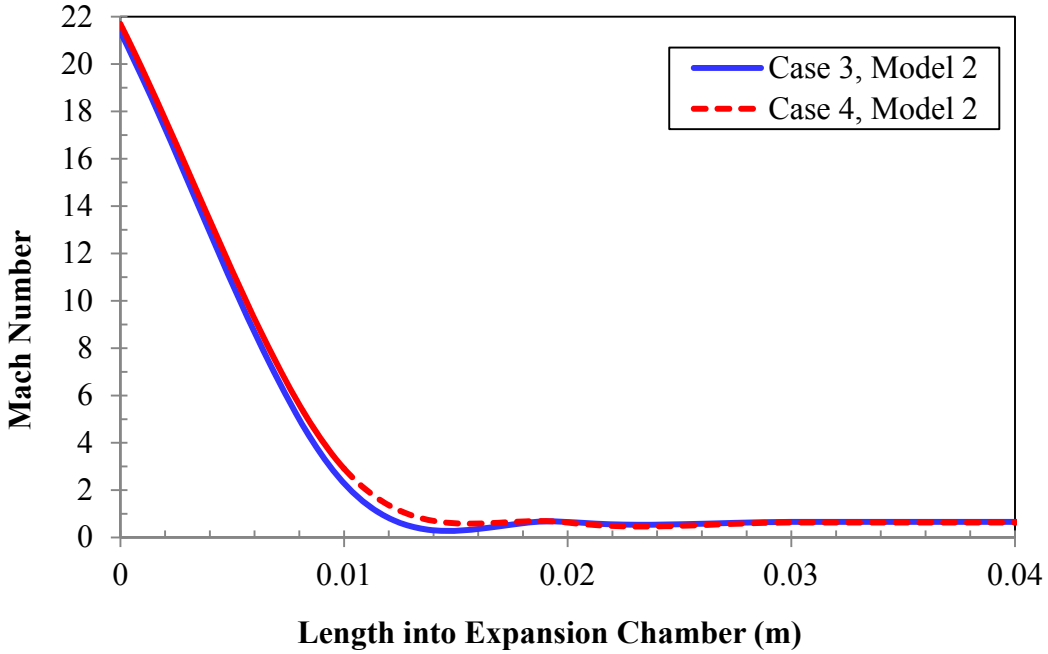


**Fig. 5.6** Change in the Mach number into the length of the expansion chamber

The bulk plasma temperature does not vary greatly at the diverging exit with the changes in the value of $\gamma$ as shown in Fig. 5.7 for the four cases with Model-2. The variation is solely due to the changes in the specific heat ratio brought in by the non-linear parameters. The steady-state bulk temperatures of the subsonic flow inside the expansion chamber for the four cases are 1.748 eV, 1.698 eV, 1.788 eV and 0.991 eV, respectively. It shows that the extreme case plasma temperatures differ by a factor of about 1.8 as seen from Fig. 5.8.

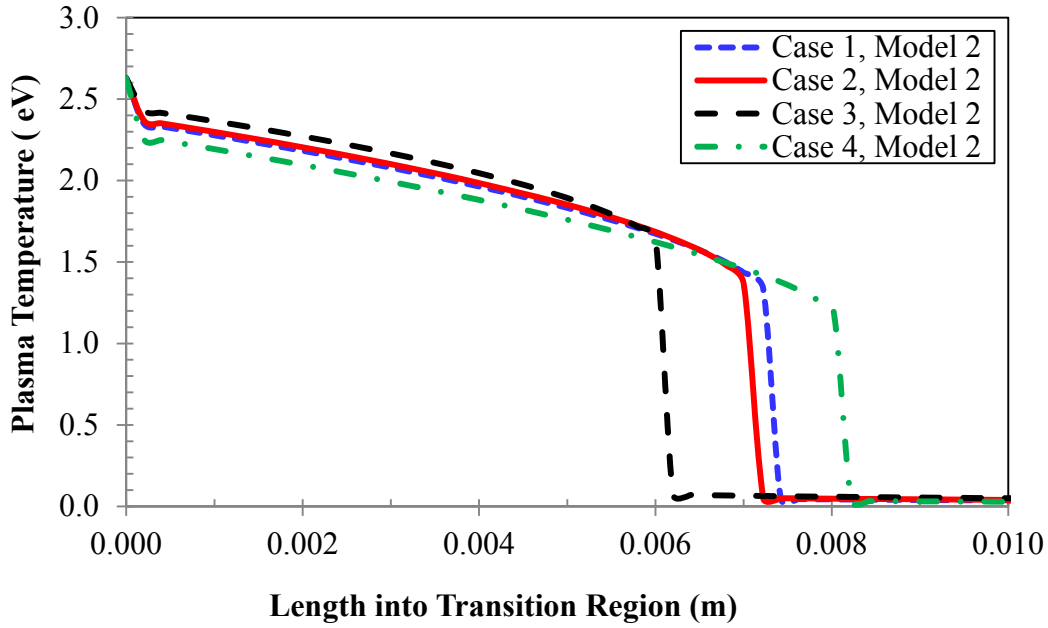


**Fig. 5.7** Change in plasma temperature along the length of the transition region

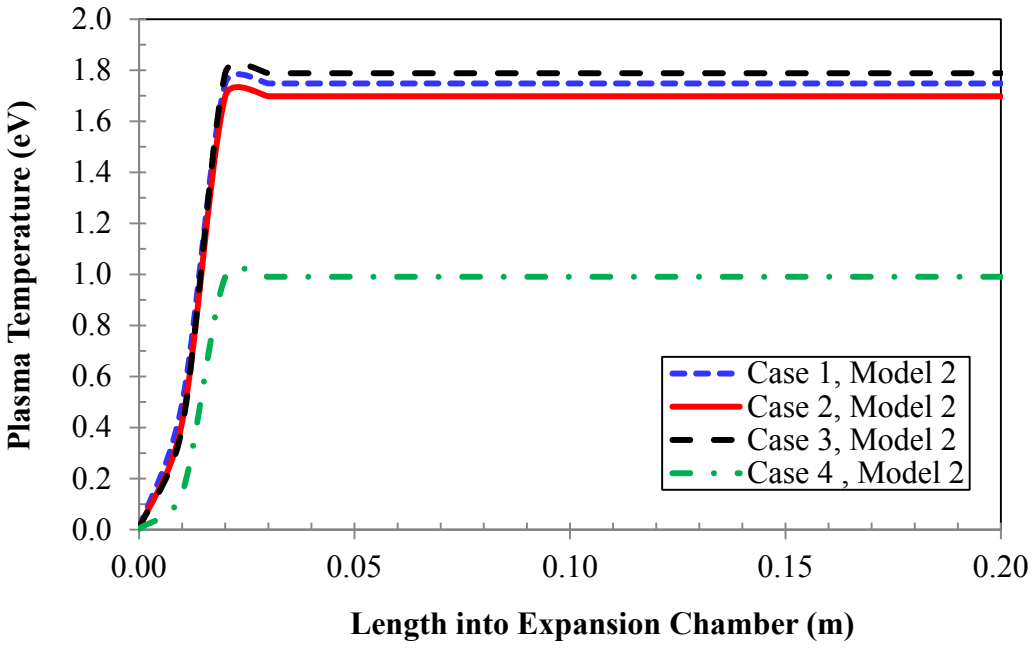


**Fig. 5.8** Change in plasma temperature into the length of the expansion chamber

Plasma bulk density is affected by the temperature-dependent changes in the value of $\gamma$. Figures 5.9 and 5.10 illustrate the features of the density profiles in the converging-diverging transition region and the expansion chamber, respectively. The bulk density values obtained at the diverging exit for the four cases are within small values, whereas the steady state bulk densities are at higher values as shown in Fig. 5.10. The bulk densities of the supersonic flow as well as the subsonic steady-state flow differ by at least an order of magnitude.

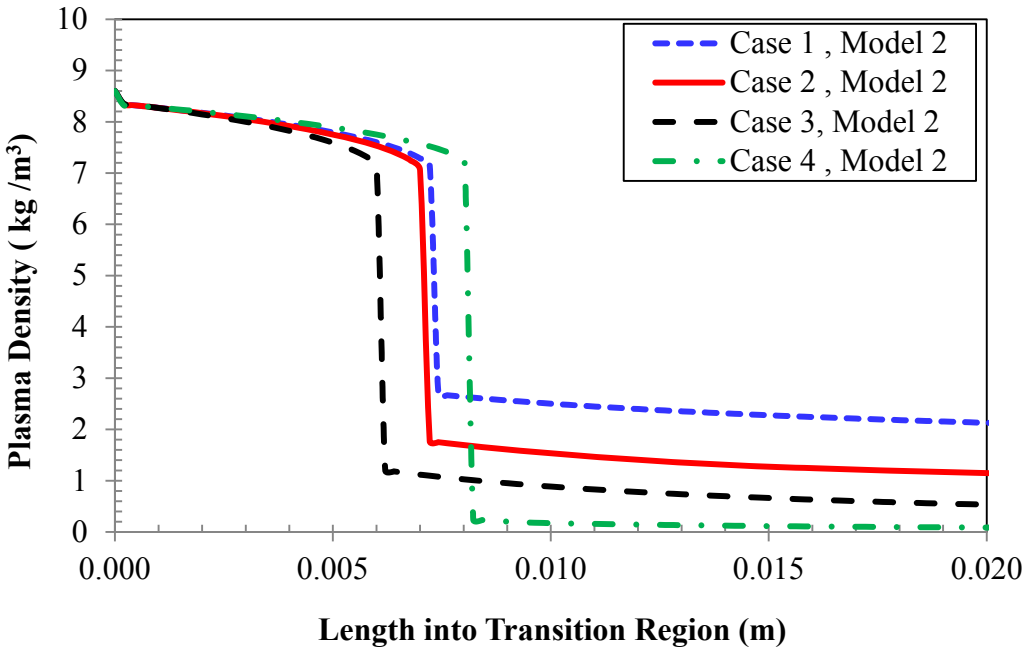


**Fig. 5.9** Change in plasma density along the length of the transition region

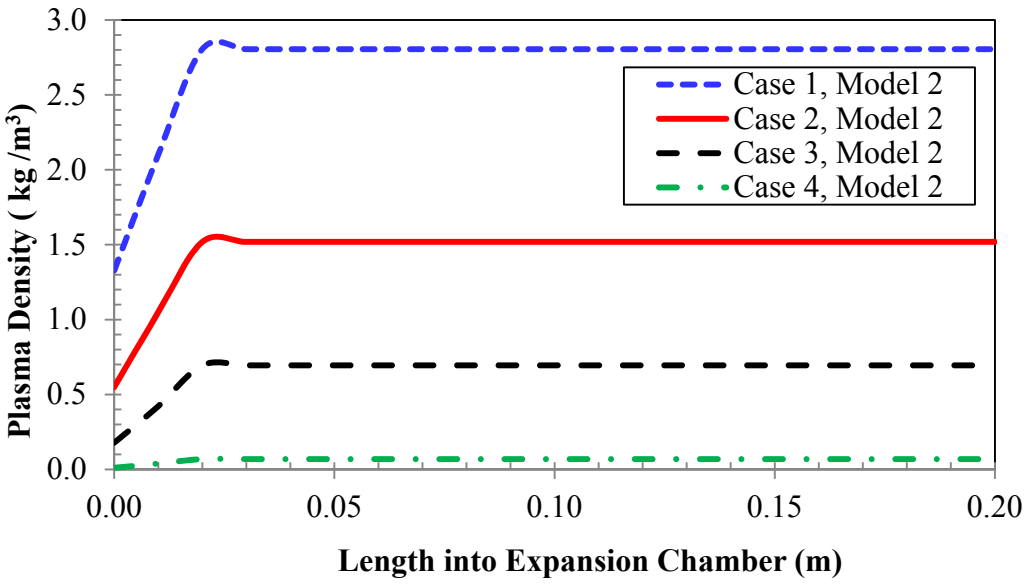


**Fig. 5.10** Change in plasma density into the length of the expansion chamber

Like plasma bulk density, the plasma pressure is also affected by the temperature-dependent changes in the value of $\gamma_p$. Figures 5.11 and 5.12 illustrate the features of the plasma pressure profiles in the converging-diverging transition region and the expansion chamber, respectively. The bulk pressure values at the diverging exit for the four cases are very low 0.099, 0.064, 0.031 and 0.0036 MPa, respectively, whereas the steady state plasma pressure of the subsonic flow are much higher as seen from Fig. 5.12 for the four cases showing 88.954, 66.280, 37.388 and 6.584 MPa, respectively. In the extreme cases the pressure of the bulk flow, both in hypersonic and the steady-state subsonic regime, differ by at least an order of magnitude.

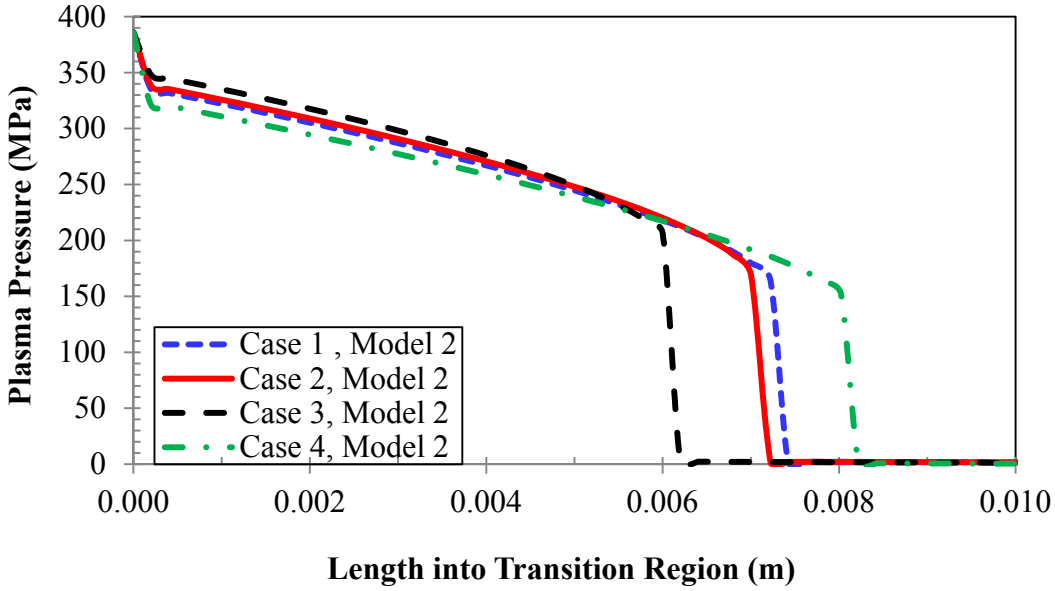


**Fig. 5.11** Change in plasma pressure along the length of the transition region

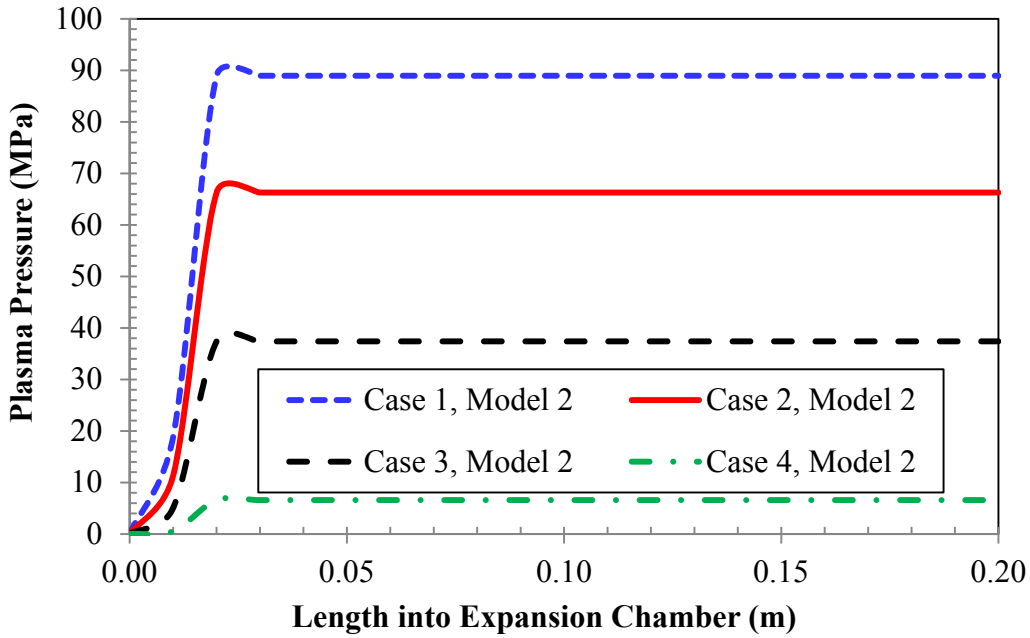


**Fig. 5.12** Change in plasma pressure into the length of the expansion chamber

Plasma bulk velocity is dependent on the sonic speed at a certain bulk plasma temperature and plasma pressure. Thus plasma bulk velocity profile depends on the specific heat ratio, bulk density and the bulk pressure. For Model-2, the bulk velocity is between

12419 and 16619 m/s for the four different cases at the diverging exit, as shown in Fig. 5.13. After the flow suffers from shock, the effect of non-linearity is obvious in case 4 where the bulk velocity jumps up to 19044m/s then drops to steady state value of 14378m/s, as seen from Fig. 5.14. For other three cases the steady-state subsonic flow speeds are 8801, 9564 and 9185m/s, respectively. Thus, it can be seen that in extreme cases the steady-state plasma bulk velocity can vary by as much as a factor of ~ 1.63 relative to the lower limit.

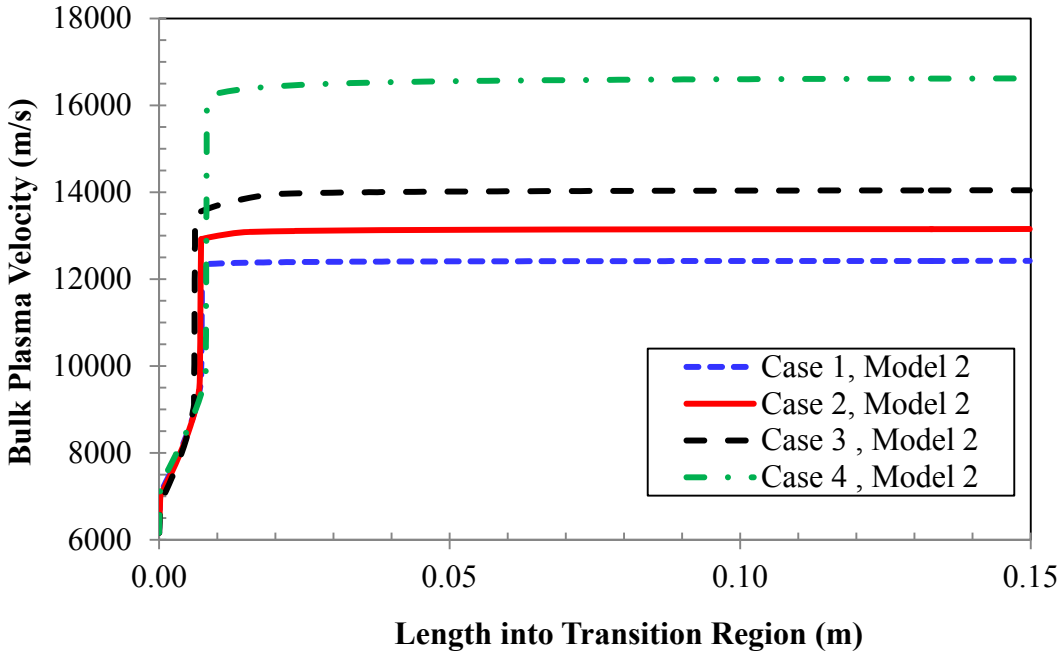


**Fig. 5.13** Change in bulk plasma velocity along the length of the transition region

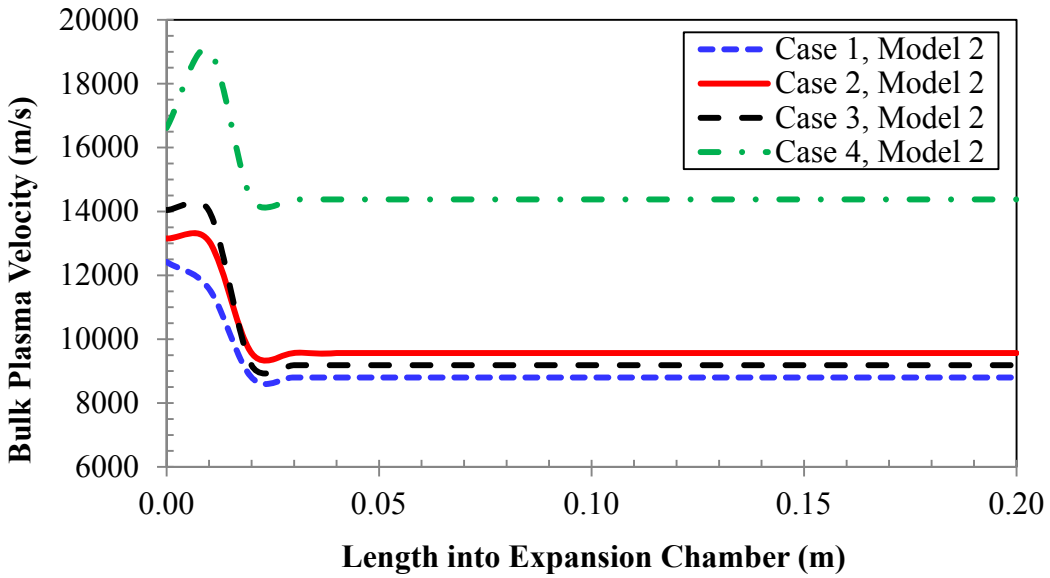


**Fig. 5.14** Change in bulk plasma velocity into the length of the expansion chamber

## 5.5 Conclusions

The effect of plasma temperature on the specific heat ratio has been investigated using a pulsed disruptive capillary electrothermal plasma source with a converging-diverging transition nozzle at the exit attached to an expansion volume. The converging section in the nozzle provides a transition from the capillary exit subsonic condition to sonic state, which allows for observing the effect of temperature on the supersonic isentropic expansion. Mathematical model has been developed for the effective atomic number ($Z_{eff}$) as a function of the plasma temperature, and was used to model the adiabatic compressibility index ($\gamma_p$) of the plasma. Profiles for plasma parameters were obtained, specifically for the pressure, density, temperature and plasma bulk velocity for temperature-dependent adiabatic compressibility index of the Lexan polycarbonate material used as ablator in the capillary plasma source. This allows a 1-D analysis of the flow parameters as a function of plasma temperature. By changing the fitting parameters it is possible to adjust the formulae to the profile corresponding to experimentally obtained dataset, which gives an opportunity to formulate case-specific correlations. Detailed information about various thermoplastics and resins can provide further information to more accurately model the effective atomic number. Further complexity can be added to the γ models by including detailed bond dissociation energies and ionization characteristics for known radicals.

## 5.6 References


[1] J. Dyvik, J. Herbig, R. Appleton, J. OReilly, and J. Shin, Recent activities in electro-thermal chemical launcher technologies at BAE systems, IEEE Trans. Magn., **43(1),** 303–307 (2007)

[2] D. Motes , J. Ellzey , S. Levinson , J. Parker, F. Stefani, and D. Wetz, A Study of electrothermal launcher efficiencies and gas dynamics, Proc. 14th Electromagnetic Launch Technology Symposium, Victoria, British Columbia, 1-6, 10-13 June 2008

[3] A.L. Winfrey, M.A. Abd Al-Halim, J.G. Gilligan, A.V. Saveliev, and M.A. Bourham, Modeling of an ablation-free electrothermal plasma pellet accelerator, Fusion Science and Technology, **60(2)**, 480-485 (2011)

[4] T.E. Gebhart, R.T. Holladay, M.J. Esmond, and A.L. Winfrey, Optimization of fusion pellet launch velocity in an electrothermal mass accelerator, J. Fusion Energy, **33(1)**, 32-29 (2014)

[5] J.R. Echols and A.L. Winfrey, Ablation of fusion materials exposed to high heat flux in an electrothermal plasma discharge as a simulation for hard disruption, Journal of Fusion Energy, **33(1)**, 60-67 (2014)

[6] N.M. AlMousa, A.L. Winfrey, J.G. Gilligan, and M.A. Bourham, Radiative heat transport through vapor plasma for fusion heat flux studies and electrothermal plasma sources applications, J. *Nucl. Ene. Sci. Power Generat.* Technol, **3:1**, 1-7 (2014)

[7] M.A. Abd Al-Halim and M.A. Bourham, Characterization of short intense pulsed electrothermal plasma capillaries for use as fusion and launchers heat flux sources, J. Fusion Energy, **33**, 258-263 (2014)

[8] E.Y. Choueiri, A critical history of electric propulsion: the First 50 years (1906–1956), J. Propulsion and Power, **20(2)**, 193–203 (2004)

[9] Y. Takao and K. Ono, A miniature electrothermal thruster using microwave-excited plasmas: a numerical design consideration, Plasma Sources Sci. Technol. **15**, 211–227 (2006)

[10] T. Edamitsu and H. Tahara, Experimental and numerical study of an electrothermal pulsed plasma thruster for small satellites, Vacuum, **80(11/12)**,1223–1228 (2006)

[11] E.Ya. Shcolnikov, M.Yu. Guzeyev, *S.*P. Maslennikov, A.V. Melnlk, and A.V. Chebotarev, Flow dynamics and microparticles acceleration in the electrothermal launcher, IEEE Trans. Magnetics, **35(1)**, 240-244 (1999)

[12] K. Kim and D.R. Peterson, A low aspect ratio electrothermal gun for metal plasma vapor discharge and ceramic nanopowder production, J. Mechanical Sc. And Technol., **22** 1408-1416 (2008)

[13] J.R. Echols, A.L. Winfrey, J.M. Nowak, and M.A. Bourham, Evaluation of materials deposited by a novel electrothermal plasma technique, Proc. 19th Pulsed Power Conference (PPC), San Francisco, CA, 1-6, 16-21 June 2013

[14] J. Cambier, M. Young, L. Pekker, and A. Pancotti, Capillary discharge based pulsed plasma thrusters, Technical Paper, Air Force Research Laboratory, AFRL-PR-ED-TP-2007-400, August 2007

[15] T.C. Lilly, A.D. Ketsdever, A.P. Pancotti, and M. Young, Development of a specific impulse balance for capillary discharge pulsed plasma thrusters, Technical Notes, J. Propulsion and Power, **25(3)**, 823-826 (2009)

[16] Volker Serini, Polycarbonates, Ullmann's Encyclopedia of Industrial Chemistry, Wiley Online Library, Published Online 15 JUN 2000, DOI: 10.1002/14356007.a21_207

[17] R. Majumdar, J.G. Gilligan, A.L. Winfrey, and M.A. Bourham, Supersonic flow patterns from electrothermal plasma source for simulated ablation and aerosol expansion following a fusion disruption, J. Fusion Energy, **33(1)**, 25-31 (2014)

[18] R. Majumdar, J.G. Gilligan, A.L. Winfrey, and M.A. Bourham, Scaling laws of bulk plasma parameters for a 1-D flow through a capillary with extended converging-diverging nozzle for simulated expansion into fusion reactor chamber, J. *Fusion Energy*, Published online 7 March 2015; DOI 10.1007/s10894-015-9899-2

[19] M M. Goodsitt, E. G. Christodoulou, and S. C. Larson, Accuracies of the synthesized monochromatic CT numbers and effective atomic numbers obtained with a rapid kVp switching dual energy CT scanner, Med. Phys. **38(4)**, 2222-2232 (2011)

[20] K. G. Sing, Effective atomic number studies in different body tissues and amino acids, Indian J. Pure & Applied Physics, **40**, 442-449 (2002)

[21] V. P. Singh, N. M. Badiger, and N. Kucuk, Determination of effective atomic numbers using different methods for some low-z materials, J. Nuclear Chemistry, Article ID 725629, 2014 (2014), http://dx.doi.org/10.1155/2014/725629

[22] Mishin G.I., 'Equation of state for a weakly ionized gas-discharge plasma', Tech. Phys. Letters 23(7), American Institute of Physics, July 1997.

[23] R. Locht, and M. Davister, "The dissociative electroionization of carbon dioxide by low-energy electron impact, the $C^+$, $O^+$ and $CO^+$ dissociation channels", International J. Mass Spectrometry and Ion Processes, **144**, 105-129 (1995)

[24] D. J. Goebbert, L. Velarde, D. Khuseynov, and A. Sanov, "C-H bond dissociation energy of malononitrile', J. Physical Chemistry Letters, **1**, 792-795 (2010)

# 6

# Temperature-Dependent Hypersonic Flow Patterns of Expanding High-Density Metal Vapor Plasma

*Published in J. Fusion Energy: "*Temperature-Dependent Hypersonic Flow Patterns of Expanding High-Density Metal Vapor Plasma from Capillary Source Simulating Plasma Flow Following a Fusion Disruption*", Rudrodip Majumdar and Mohamed A. Bourham, J. Fusion Energy, Published online 14 October 2015, DOI:* 10.1007/s10894-015-0027-0.

Capillary discharge devices generating electrothermal plasmas from ablation of a liner material exposed to high heat flux are adequate devices to simulate fusion disruptions. Expansion of capillary-generated plasma into large volume simulates the evolution of the aerosol and plasma particulates into the reactor vacuum vessel. Effect of non-linearity and plasma bulk temperature on the adiabatic compressibility index was previously investigated showing considerable effect on the bulk flow parameters of polycarbonate plasma formed by the ablation of the capillary inner wall. In a fusion reactor, metals in the plasma-facing components such as the divertor, limiter, and first wall, will experience evaporation and formation of metal-vapor plasmas. Mathematical models have been developed to investigate the adiabatic compressibility index of ionized bulk metal vapors taking into account atomic and cluster ionization of metals, in addition to the effect of plasma bulk temperature and other nonlinearities. An important aspect of this current work is the distinction of the ionized states of metallic species instead of temperature-dependent lumped effective atomic number.

## 6.1 Introduction

Formation of metal-vapor plasmas in a pulsed capillary discharge generates high-density electrothermal plasma from the ablation of the metallic liner material with typical number densities in the range of $10^{26} - 10^{27}\ m^{-3}$, and temperatures in the range 1-5 eV **[1].** The saturated vapor pressure and the dynamic temperature of molten metal largely affect the formation of the metal vapor plasma and its distribution. Purity and bulk density of the

plasma is dependent on the liner material and device dimensions. Inappropriate arc conditions, lack of arc control, contamination on the electrode surfaces or electrode sever erosion may lead to metal vapor contamination **[2-6].** Even the clusters coming out of the ablated metal surface may lead to formation of dusty plasma as it is quite commonly found in plasmas with an electron temperature below 10 eV. In such a case the plasma is not fully ionized, and thus the ions tend to collide with neutral atoms as well as the clusters. In the experiments under consideration, where the screening length is typically less than a millimeter, and the plasma pressure is in hundreds of MPa, collisionality could be quite significant and hence the cluster formation is becoming eminent.

Unlike the case of insulating materials like Lexan or other non-conductive polycarbonate resins, a capillary discharge system with ablative metallic sleeve will have to be equipped with insulating ends to prevent short circuiting. A 1.0 cm long insulating guard in tubular shape is kept at each side of the metallic sleeve, which keeps the metallic sleeve floating and prevents short-circuiting the discharge current. The capillary in this configuration, as illustrated in Fig. 6.1, is connected to an expansion volume to simulate the flow into a fusion reactor vacuum vessel following a disruption event. The capillary source and the expansion chamber simulate the divertor and the vacuum vessel, respectively.

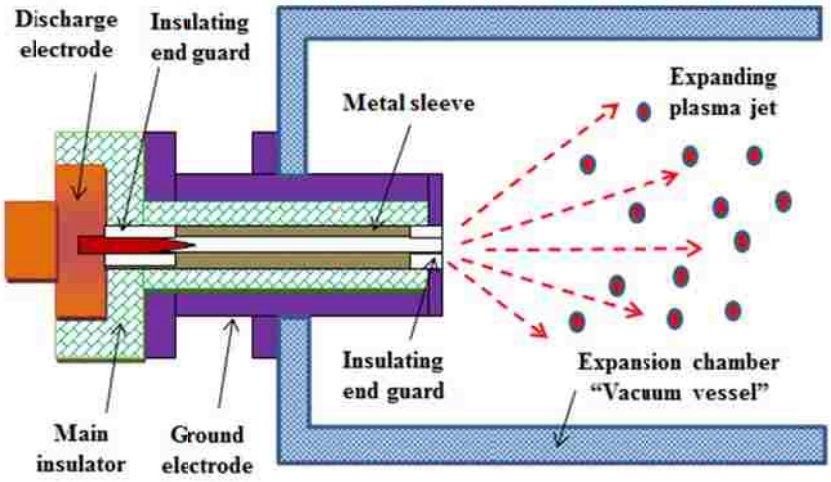


**Fig. 6.1** Schematic diagram of a capillary discharge with ablative metallic sleeve connected to an expansion chamber simulating the fusion vacuum vessel

To investigate the compressibility index in metal vapor plasma, in the simulation of fusion disruption, six metals were chosen as sleeve materials for their possible application in various plasma facing components; namely tungsten (W), molybdenum (Mo), iron (Fe), Chromium (Cr), Titanium (Ti) and aluminium (Al). The ETFLOW solver **[7]** has been run for multiple values of peak discharge current covering a range of 40 – 100 kA, for all selected metal liners. The ETFLOW calculates the temperature T (eV), pressure P (MPa), number density Np (particles/$m^3$), bulk density ρ (kg/$m^3$), plasma bulk velocity $V_{bulk}$ (m/s) and the total ablated metal mass $M_{abl}$ (mg) at each axial node. The peak values at the last node, the capillary exit, are taken as the values of interest in simulating the plasma flow and expansion into the vacuum vessel. Ionization of individual atoms, as well as the cluster formation and subsequent ionization in the ablated metal-vapor plasma bulk, have been taken into account. In the present case, the first and the second ionization have been considered for isolated atoms, as well as the smallest atomic cluster (as a dimer having a single positive charge). The effect of plasma bulk temperature and the effective atomic numbers on the metal-vapor plasma bulk flow parameters have been investigated. As well known in the compressible flow regime, the adiabatic compressibility index ($\gamma_p$) is an important aspect that significantly affects the supersonic flow patterns. In this work mathematical models for the adiabatic compressibility index of partially ionized metal vapor have been proposed, that include plasma bulk temperature, atomic ionization energies and corresponding effective atomic numbers, dimer ionization energy and some predictive parameters that account for associated non-linearity as well as non-ideality.

## 6.2 Temperature-Dependent Compressibility Index Models

The isolated atoms or the monomers and the dimers being considered as the main constituents of the partially ionized high density metal vapor bulk; assuming the non-interacting, ideal gas behaviour of the constituents in a mixture of monoatomic and diatomic gases, one would prefer a linear approximation approach in finding the adiabatic compressibility index of the system resulting in an approximate value of $\gamma_p \approx (\gamma_{Mono} + \gamma_{dia}) / 2 \approx 1.53$. But partially ionized, very high density, high temperature, high pressure electrothermal plasmas exhibit highly non-linear behavior and the modeling of adiabatic

compressibility index as a function of plasma bulk temperature becomes much more complicated. Two similar, yet different models for the adiabatic compressibility index ($\gamma_p$) have been proposed in this work. For each model four cases have been presented, which essentially make the formulae quite versatile and capable of explaining any irregular changes that might occur in the parameter profiles under different experimental conditions. The first model for $\gamma_p$ is given below in Eq. (6.1).

$$\left.\begin{gathered}\frac{\gamma_p}{\gamma_p-1.53} = 1.1 + 0.25 * \frac{\left\{a_1\left(\frac{E_{I1}}{T_p}\right)^{a_2} + b_1\left(\frac{E_{I2}}{T_p}\right)^{b_2} + c_1\left(\frac{E_{Dim}}{T_p}\right)^{c_2}\right\}}{\left(1+Z^*_{comb}\right)^{d}}, \\ \left(0.25 \le T_p(eV) \le 10\right) \\ \text{where, } Z^*_{comb} = \left({Z_1}^{k_1} + {Z_2}^{k_2}\right)^{\frac{1}{k_1+k_2}} \\ \gamma_p\left(T_p < 0.25\ eV, Z^*_{comb}\right) = \gamma_p\left(T_p = 0.25\ eV, Z^*_{comb}\right) \\ \gamma_p\left(T_p > 10\ eV, Z^*_{comb}\right) = \gamma_p\left(T_p = 10\ eV, Z^*_{comb}\right)\end{gathered}\right\} \quad (6.1)$$

Here $E_{I1}$ and $E_{I2}$ are the ionization energies corresponding to the first and second ionizations respectively, for an isolated atom in the gaseous phase. $E_{Dim}$ is dimer ionization energy, $T_p$ is the plasma bulk temperature in eV, $Z_1$ and $Z_2$ are the effective atomic numbers in the first and second ionization of isolated atom, respectively. The parameters $a_1$, $a_2$ , $b_1$ , $b_2$ , $c_1$ , $c_2$ , $k_1$ , $k_2$ and $d$ are chosen intuitively and they take into account non-ideal as well as non-linear effects associated with the system. Four specific cases defined by four sets of values of the above mentioned parameters were investigated. These cases will enable an insight into the effect of dynamically changing $\gamma_p$ on the metal vapor plasma flow characteristics. Table 6.1 lists the selected values of the parameters for each case.

**Table 6.1** Non-linearity parameters for Model 1

| Non-linearity parameter | Case 1 | Case 2 | Case 3 | Case 4 |
|---|---|---|---|---|
| $a_1$ | 1.00 | 1.00 | 1.00 | 1.00 |
| $a_2$ | 0.04 | 0.08 | 0.27 | 0.38 |
| $b_1$ | 1.00 | 1.00 | 1.00 | 1.00 |
| $b_2$ | 0.04 | 0.08 | 0.27 | 0.38 |
| $c_1$ | 1.00 | 1.00 | 1.00 | 1.00 |
| $c_2$ | 0.04 | 0.08 | 0.27 | 0.38 |
| $k_1$ | 0.90 | 0.20 | 0.70 | 0.80 |
| $k_2$ | 0.90 | 0.20 | 0.70 | 0.80 |
| $d$ | 0.85 | 0.40 | 0.80 | 0.60 |

For all selected metals, the plots for $\gamma(T_p)$ will follow a similar profile. The departure from one case to another will also be very similar, as a generic mathematical model has been used. The values of $\gamma(T_p)$ as a function of $T_p$ for tungsten using Model 1 are illustrated in Fig. 6.2. The adiabatic compressibility index increases with the increase in the plasma temperature for all cases with less increase for case 1, which appears to be more flat. Strong increase is obvious for cases 3 and 4, almost a factor of 2 higher at the highest temperature (10 eV) as compared to the lowest temperature of 0.25 eV.

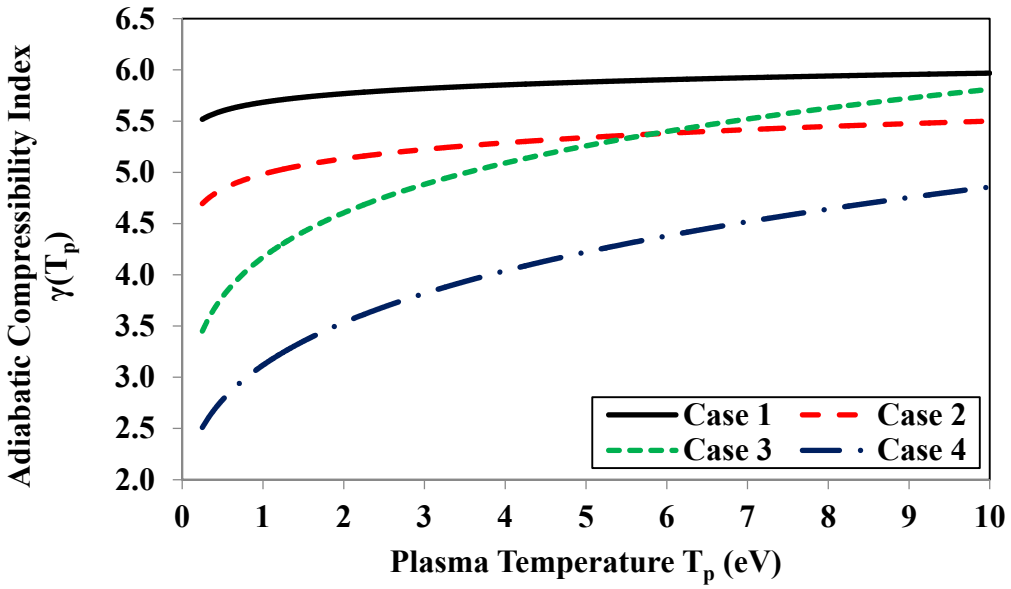


**Fig. 6.2** $\gamma(T_p)$ as a function of plasma temperature $T_p$ for tungsten using Model 1

Model 2 is somewhat similar to Model 1, with a major difference in writing the parameter $d$ as the exponent to a mathematical expression that contains the combined optimized orbital exponent $Z^*_{comb}$ (as defined in Eq. 6.1), which includes the individual optimized orbital exponents $Z_1$ and $Z_2$, respectively. Essentially this means for higher values of $d$, the value of $\gamma_p$ will depend on a polynomial of $Z^*_{comb}$ manifesting a higher extent of non-linearity. The effective nuclear charge increases with the increase in the cluster size **[8].** Thus, by tuning the non-linearity parameters in the expression of adiabatic compressibility index to suitable values, such that $Z^*_{comb}$ covers an adequately varied range of numerical values; the effect of the cluster formation and subsequent ionization on the bulk plasma flow characteristics can be computed. In case of Model 2, single power on each of the individual optimized orbital exponents has been used. Model 2 is given mathematically in Eq. (6.2):

$$\left.\begin{array}{c} \frac{\gamma_p}{\gamma_p - 1.53} = 1.2 + 0.15 * \frac{\left\{a_1'\left(\frac{E_{I1}}{T_p}\right)^{a_2'} + b_1'\left(\frac{E_{I2}}{T_p}\right)^{b_2'} + c_1'\left(\frac{E_{Dim}}{T_p}\right)^{c_2'}\right\}}{\left(r_1' Z_1^{s_1'} + r_2' Z_2^{s_2'}\right)}; \\ \left(0.25 \leq T_p(eV) \leq 10\right) \\ \gamma_p\left(T_p < 0.25\ eV, Z_1, Z_2\right) = \gamma_p\left(T_p = 0.25\ eV, Z_1, Z_2\right) \\ \gamma_p\left(T_p > 10\ eV, Z_1, Z_2\right) = \gamma_p\left(T_p = 10\ eV, Z_1, Z_2\right) \end{array}\right\} \quad (6.2)$$

where**,** $E_{I1}$ , $E_{I2}$ , $E_{Dim}$ , $T_p$ , $Z_1$ and $Z_2$ bear the same meaning as in Model 1. $a_1'$ , $a_2'$ , $b_1'$ , $b_2'$, $c_1'$, $c_2'$ , $r_1'$ , $r_2'$ , $s_1'$ and $s_2'$ are the parameters that incorporates non-linearity and non-ideal effects. By using these models for $\gamma_p$, unexpected bulk irregularities and sudden variation in bulk flow characteristics can be explained, which may arise in various experimental scenarios. Table 6.2 lists the selected values of the parameters for each case.

**Table 6.2** Non-linearity parameters for Model 2

| Non-linearity parameter | Case 1 | Case 2 | Case 3 | Case 4 |
|---|---|---|---|---|
| $a_1'$ | 1.00 | 1.00 | 1.00 | 1.00 |
| $a_2'$ | 0.15 | 0.16 | 0.17 | 0.30 |
| $b_1'$ | 1.00 | 1.00 | 1.00 | 1.00 |
| $b_2'$ | 0.15 | 0.16 | 0.17 | 0.30 |
| $c_1'$ | 1.00 | 1.00 | 1.00 | 1.00 |
| $c_2'$ | 0.15 | 0.16 | 0.17 | 0.30 |
| $r_1'$ | 0.70 | 0.70 | 0.70 | 0.20 |
| $r_2'$ | 0.30 | 0.30 | 0.30 | 0.20 |
| $s_1'$ | 0.45 | 0.75 | 1.05 | 0.60 |
| $s_2'$ | 0.45 | 0.75 | 1.05 | 0.80 |

The values of $\gamma(T_p)$ as a function of $T_p$ for tungsten using Model 2 are illustrated in Fig. 6.3. Again, the adiabatic compressibility index increases with the increase in the plasma temperature for all cases as was previously shown when using Model 1. However, the rate of increase is not as high as that of Model 1.

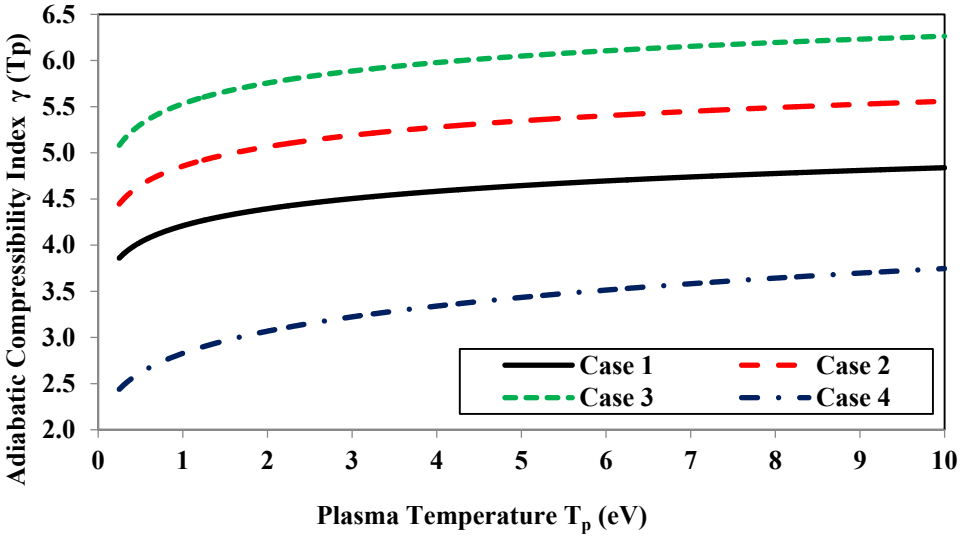


**Fig. 6.3** $\gamma(T_p)$ as a function of plasma temperature $T_p$ for tungsten using Model 2

The ionization energies for the single isolated metal atoms as well as the dimers have been taken from available well-known literature **[9-12].** Some of the thermodynamic properties for specific metals were obtained from the published work of P. D. Desai **[13].** The effective atomic numbers or the optimized orbital exponents were obtained using information

available in published literature **[14, 15].** Table 6.3 lists the ionization energies and the optimized orbital exponents of the selected metals. By incorporating these models for **γ** into the temperature sensitive supersonic flow equations as well as the shock models, as described in one of our previous work **[18],** it was shown that variation in bulk flow parameters of the metal vapor plasma is caused by non-linear changes in adiabatic compressibility index under isentropic conditions of the expanding plasma bulk.

**Table 6.3** Ionization energies and optimized orbital exponents

| **Metal** | $E_{I1}$ **(eV)** | $E_{I2}$ **(eV)** | $E_{Dim}$ **(eV)** | $Z_1$ | $Z_2$ |
|---|---|---|---|---|---|
| **W** | 7.8640 | 16.10 | 14.43 | 3.550 | 3.550 |
| **Mo** | 7.0924 | 16.16 | 8.00 | 6.106 | 11.392 |
| **Fe** | 7.9024 | 16.19 | 6.10 | 5.434 | 5.434 |
| **Cr** | 6.7665 | 16.49 | 6.40 | 5.133 | 9.757 |
| **Ti** | 6.8281 | 13.57 | 6.13 | 4.817 | 4.817 |
| **Al** | 5.9858 | 18.83 | 6.21 | 4.117 | 4.066 |

## 6.3 Result and Discussion

Capillary exit parameters of interest have been tabulated in Tables 6.4, 6.5, 6.6 and 6.7 for four different peak discharge current values of 40, 50, 60 and 80 kA, respectively, which covers a reasonably wide range. The exit parameters were calculated using the 1-D ETFLOW code [7]. The exit parameters in Tables 6.4, 6.5, 6.6 and 6.7 are the plasma temperature T (eV), pressure P (MPa), number density $N_p$ (#/$m^3$), density **ρ** (kg/$m^3$), plasma exit velocity $V_{bulk}$ (m/s) and total ablated mass $M_{abl}$ (mg). Tables 6.4 to 6.7 clearly show that the peak magnitude of all plasma exit parameters increases with the increase of the peak discharge current. However this increment in flow parameter is not linear with the increment in the peak discharge current. The capillary exit data obtained here are the bulk parameter values with which the metal vapor from ablation leaves the micro-nozzle and enters the converging section of the transition region **[16-18].**

**Table 6.4** Capillary exit parameters for peak discharge current I = 40 kA

| Metal | T (eV) | P ( MPa) | Np (# /$m^3$) | ρ (kg/$m^3$) | $V_{bulk}$ (m/s) | $M_{abl}$ (mg) |
|---|---|---|---|---|---|---|
| **W** | 2.780 | 395.192 | $1.12 \times 10^{27}$ | 341.857 | 1404.19 | 1039.37 |
| **Mo** | 2.680 | 412.061 | $1.03 \times 10^{27}$ | 164.057 | 1947.20 | 561.94 |
| **Fe** | 2.504 | 445.977 | $1.18 \times 10^{27}$ | 109.411 | 2424.76 | 411.83 |
| **Cr** | 2.503 | 451.773 | $1.09 \times 10^{27}$ | 94.097 | 2558.28 | 364.28 |
| **Ti** | 2.539 | 405.441 | $9.24 \times 10^{26}$ | 73.433 | 2797.41 | 290.83 |
| **Al** | 2.479 | 472.132 | $1.03 \times 10^{27}$ | 46.138 | 3529.53 | 189.50 |

**Table 6.5** Capillary exit parameters for peak discharge current I = 50 kA

| Metal | T (eV) | P (MPa) | Np (# /$m^3$) | ρ (kg/$m^3$) | $V_{bulk}$ (m/s) | $M_{abl}$ (mg) |
|---|---|---|---|---|---|---|
| **W** | 2.974 | 558.673 | $1.36 \times 10^{27}$ | 415.110 | 1480.69 | 1330.21 |
| **Mo** | 2.916 | 570.215 | $1.28 \times 10^{27}$ | 203.892 | 2022.15 | 716.24 |
| **Fe** | 2.646 | 588.561 | $1.43 \times 10^{27}$ | 132.587 | 2509.40 | 517.74 |
| **Cr** | 2.638 | 594.873 | $1.34 \times 10^{27}$ | 115.681 | 2667.26 | 458.67 |
| **Ti** | 2.691 | 591.277 | $1.17 \times 10^{27}$ | 92.982 | 2898.57 | 367.26 |
| **Al** | 2.640 | 632.541 | $1.25 \times 10^{27}$ | 55.997 | 3702.54 | 242.59 |

**Table 6.6** Capillary exit parameters for peak discharge current I = 60 kA

| Metal | T (eV) | P (MPa) | Np (# /$m^3$) | ρ (kg/$m^3$) | $V_{bulk}$ (m/s) | $M_{abl}$ (mg) |
|---|---|---|---|---|---|---|
| **W** | 3.188 | 705.855 | $1.62 \times 10^{27}$ | 494.475 | 1525.14 | 1621.51 |
| **Mo** | 3.088 | 726.104 | $1.52 \times 10^{27}$ | 242.124 | 2107.15 | 870.01 |
| **Fe** | 2.793 | 752.961 | $1.69 \times 10^{27}$ | 156.695 | 2601.42 | 624.15 |
| **Cr** | 2.782 | 768.145 | $1.59 \times 10^{27}$ | 137.265 | 2773.65 | 554.03 |
| **Ti** | 2.950 | 747.377 | $1.43 \times 10^{27}$ | 113.646 | 3147.54 | 446.31 |
| **Al** | 2.776 | 796.389 | $1.48 \times 10^{27}$ | 66.302 | 3804.79 | 294.29 |

**Table 6.7** Capillary exit parameters for peak discharge current I = 80 kA

| Metal | T (eV) | P (MPa) | Np (# /$m^3$) | ρ (kg/$m^3$) | $V_{bulk}$ (m/s) | $M_{abl}$ (mg) |
|---|---|---|---|---|---|---|
| **W** | 3.539 | 1114.000 | $2.18 \times 10^{27}$ | 665.409 | 1648.43 | 2201.05 |
| **Mo** | 3.408 | 1137.145 | $2.08 \times 10^{27}$ | 331.319 | 2259.81 | 1182.99 |
| **Fe** | 3.113 | 1130.056 | $2.26 \times 10^{27}$ | 209.547 | 2826.95 | 837.65 |
| **Cr** | 3.030 | 1166.647 | $2.14 \times 10^{27}$ | 187.742 | 2954.30 | 745.51 |
| **Ti** | 3.150 | 1335.867 | $1.98 \times 10^{27}$ | 157.358 | 3278.45 | 608.53 |
| **Al** | 3.024 | 1164.840 | $1.95 \times 10^{27}$ | 87.355 | 3995.50 | 398.23 |

Figures 6.4 and 6.5 display the Mach number profile along the axial direction into the transition region (Fig. 6.4) and the expansion chamber (Fig. 6.5) showing that the Mach number is almost the same for all metals, which was previously discussed in our work on flow patterns and scaling of the flow bulk parameters **[16, 17].** However, the minor

deviations that arise are solely due to the changes in the adiabatic compressibility index, which has been modeled as a function of plasma bulk temperature as well as metal properties.

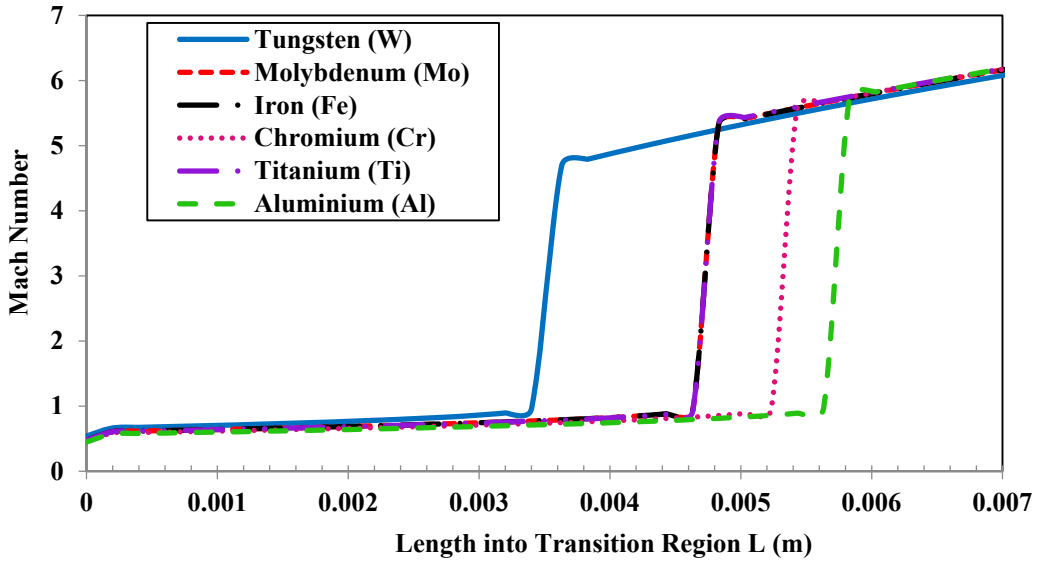


**Fig. 6.4** Mach Number along the axial length in the transition region for I=40 kA peak current for Case 1 (Model 1)

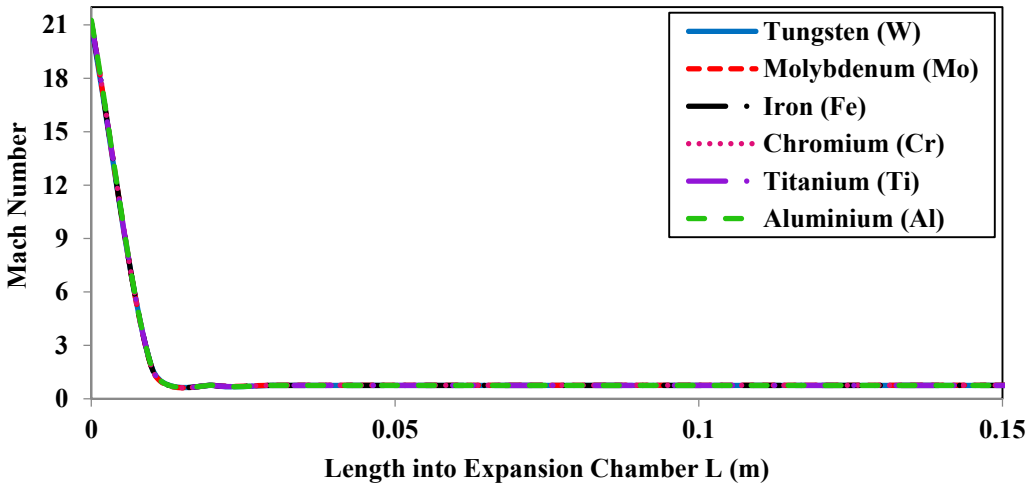


**Fig. 6.5** Mach number along the axial length in the expansion chamber for Case 1 (Model 1)

Figures 6.6 through 6.13 show the flow bulk parameters along the axial direction for $I_{peak}$=40kA for Case 1 (Model 1). Figure 6.6 shows the plasma temperature along the axial length in the transition region immediately after the ET source exit (0-0.007 meter) for I= 40 kA, Case 1 (Model 1). The temperature drops quickly inside this region for all tested metals. The temperature into the expansion chamber immediately after exiting the transition region and through the axial direction of the chamber is shown in Fig. 6.7, where the temperature rises and stays almost constant through the length of the chamber.

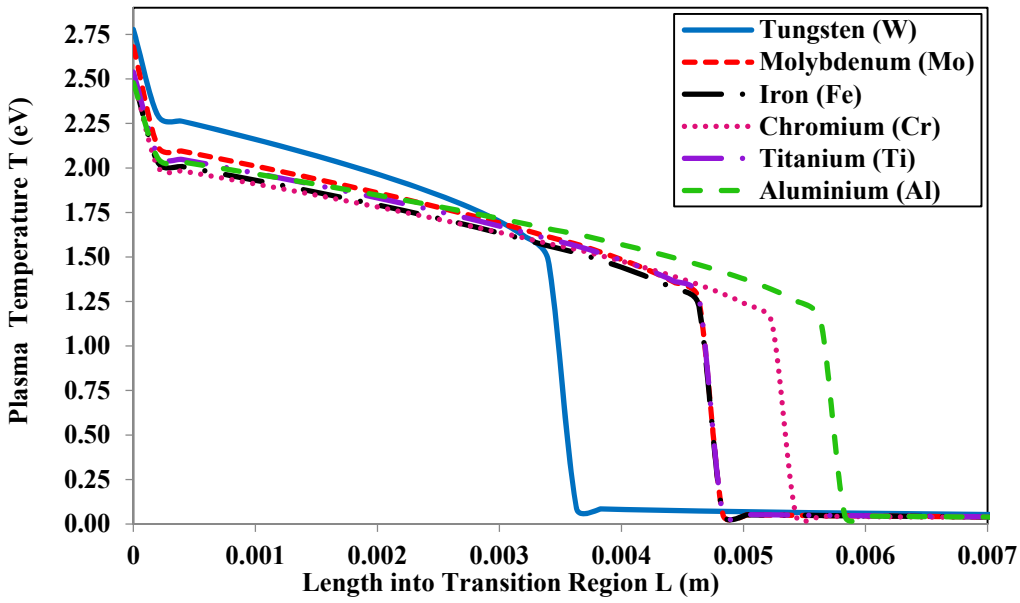


**Fig. 6.6** Plasma temperature along the axial length in the transition region immediately after the ET source exit

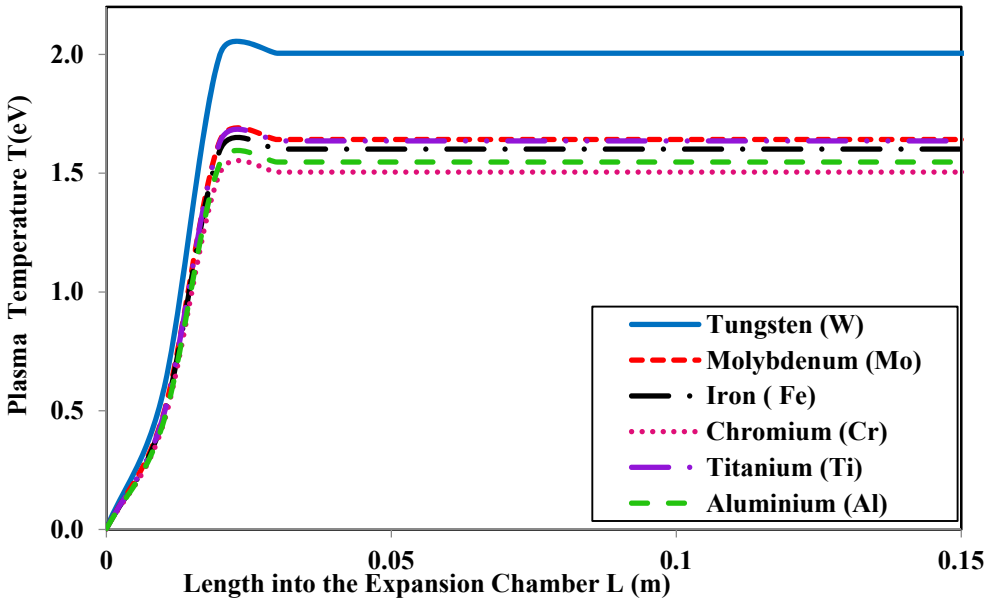


**Fig. 6.7** Plasma temperature into the expansion chamber immediately after exiting the transition region and through the axial direction of the chamber

Figure 6.8 shows the plasma pressure along the axial length in the transition region immediately after the ET source exit (0-0.007 meter) for I= 40 kA, Case 1 (Model 1). The pressure drops quickly inside this region for all tested metals, and has a similar profile of that of the temperature. The pressure into the expansion chamber immediately after exiting the transition region and through the axial direction of the chamber is shown in Fig. 6.9, where the pressure rises and stays almost constant through the length of the chamber; a pattern similar to that of the temperature.

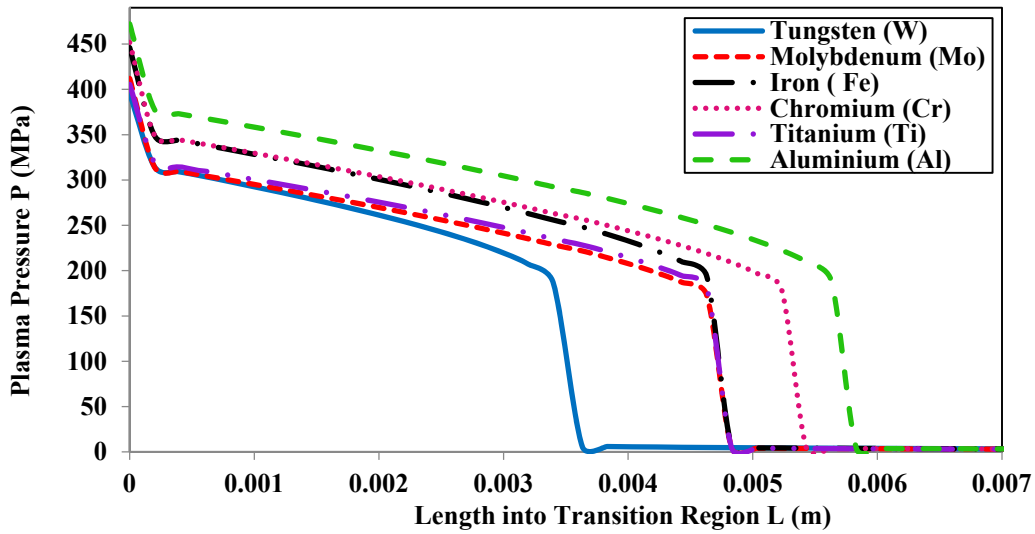


**Fig. 6.8** Plasma pressure along the axial length in the transition region immediately after the ET source exit

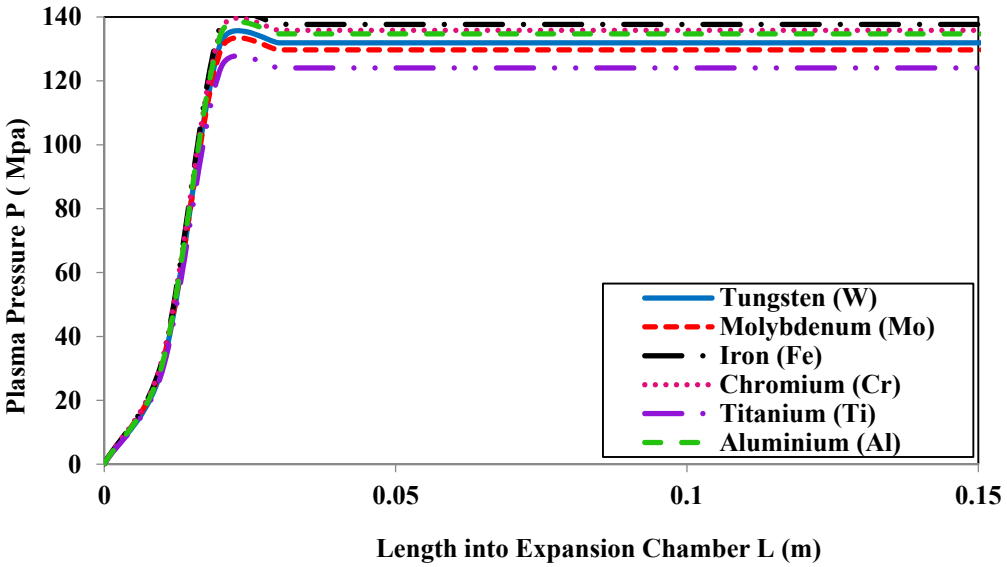


**Fig. 6.9** Plasma pressure into the expansion chamber immediately after exiting the transition region and through the axial direction of the chamber

Figure 6.10 shows the plasma bulk velocity along the axial length in the transition region immediately after the ET source exit. The bulk velocity increases inside this region for all tested metals and remains at a constant value after 0.007m into the transition. The velocity into the expansion chamber immediately after exiting the transition region and through the

axial direction of the chamber is shown in Fig. 6.11, where the velocity slightly drops and stays almost constant through the length of the chamber.

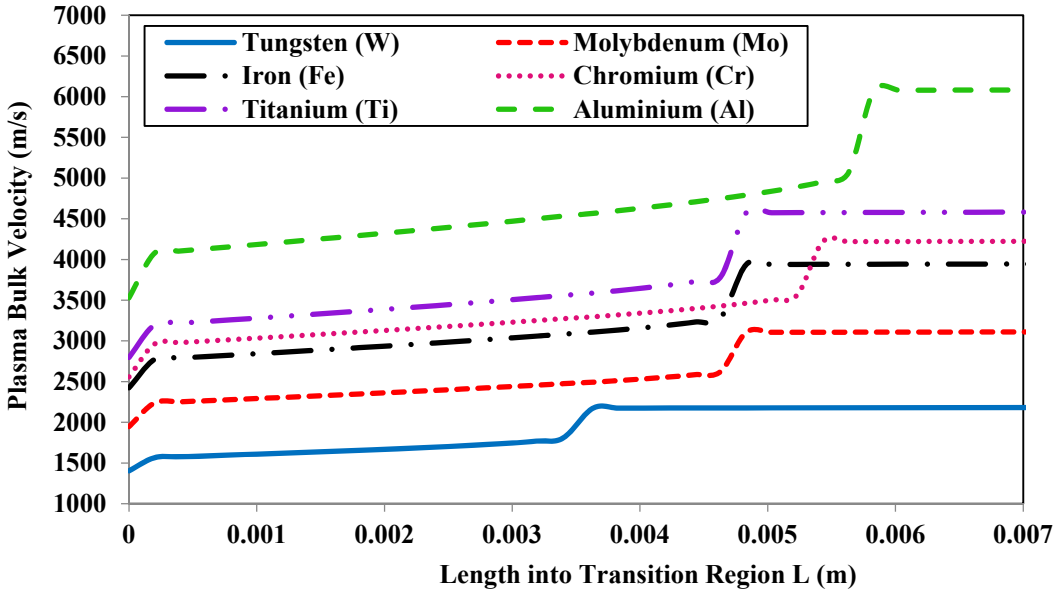


**Fig. 6.10** Plasma bulk velocity along the axial length in the transition region immediately after the ET source exit

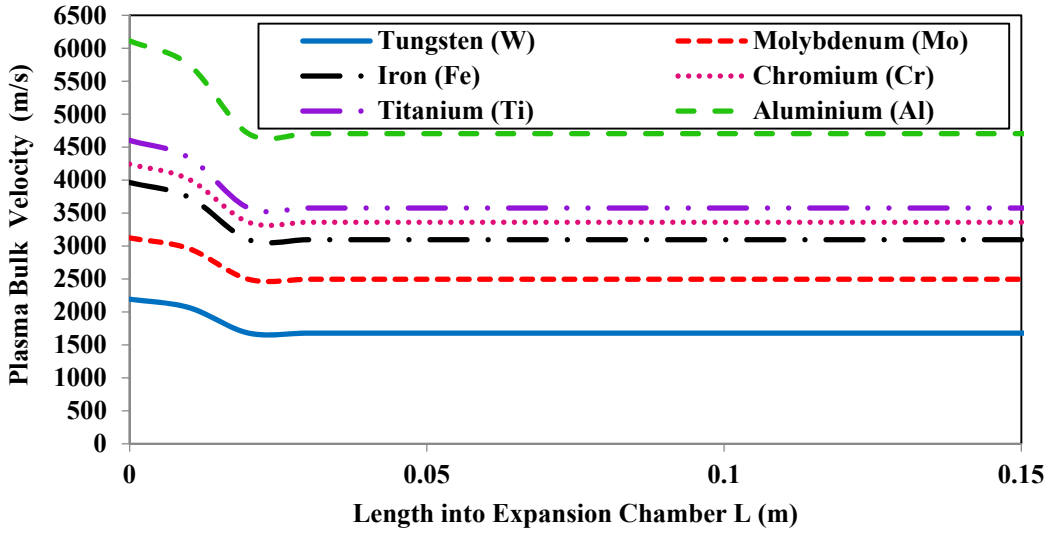


**Fig. 6.11** Plasma Bulk velocity into the expansion chamber immediately after exiting the transition region and through the axial direction of the chamber

Figure 6.12 shows the plasma bulk density along the axial length in the transition region immediately after the ET source exit. The bulk density decreases inside this region for all tested metals and remains at a constant value after 0.007m into the transition. Of interest is the higher drop rate in the density of tungsten as compared to all other tested metals. The density into the expansion chamber immediately after exiting the transition region and through the axial direction of the chamber is shown in Fig. 6.13, where the density increases and stays almost constant through the length of the chamber, with tungsten density rises higher than all other metals.

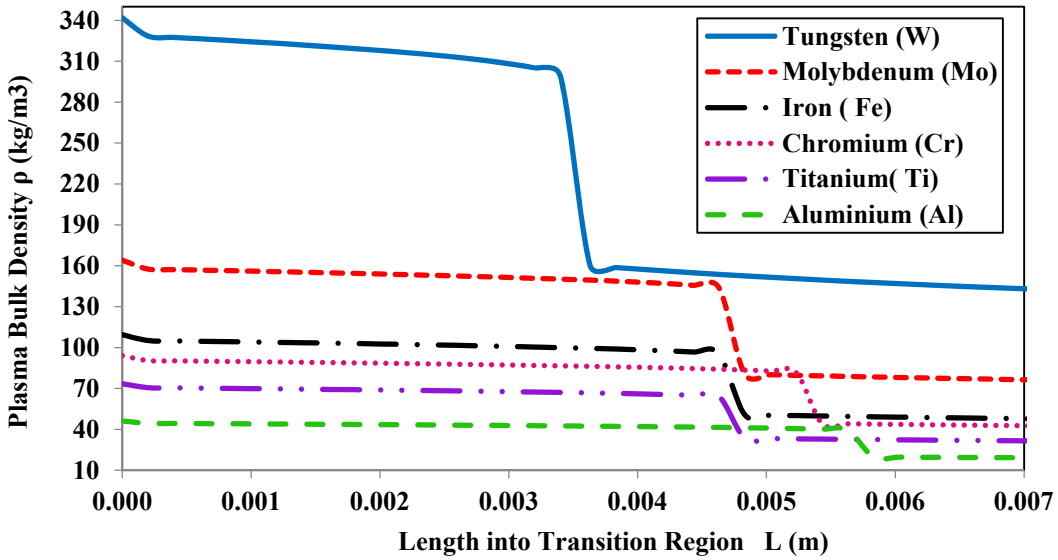


**Fig. 6.12** Plasma bulk density along the axial length in the transition region immediately after the ET source exit

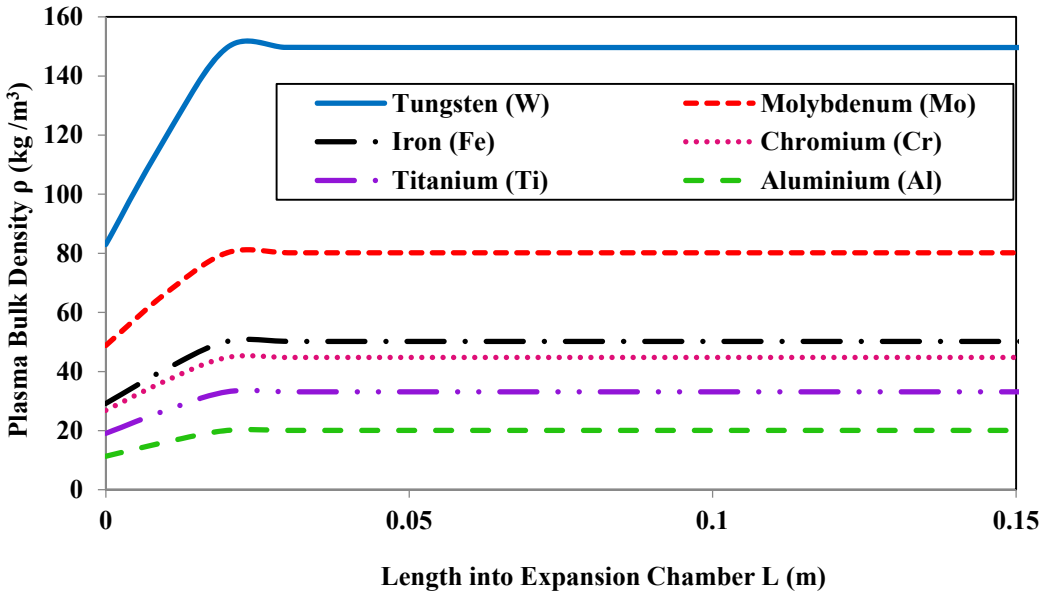


**Fig. 6.13** Plasma Bulk density into the expansion chamber immediately after exiting the transition region and through the axial direction of the chamber

Table 6.8 shows that as the bulk plasma flow becomes sub-sonic inside the expansion chamber of uniform area cross-section, some of the steady-state flow parameters for the metal vapor plasmas differ in magnitude by quite a significant amount, whereas the other parameters do not vary that much. For example the steady state plasma bulk temperature for tungsten has been found to be 2.005 eV ,which is the maximum value; whereas the lowest bulk temperature was found to be 1.505 eV in case of chromium vapor plasma. The steady-state plasma pressure is the maximum in case of iron ablated plasma and was found to be 137.67 MPa, while the minimum pressure has been estimated to be 124.05 MPa in the case where titanium sleeve was used. Looking at the above two flow parameters one does not see much difference between the maximum and the minimum steady-state values. But there is a significant change in case of the plasma bulk density. The maximum bulk density in the steady-state subsonic conditions has been estimated to be 149.64 kg/m$^3$, for the tungsten vapor plasma, which is about 7 times larger than that found as the minimum of all others, a considerably low 20.07 kg/m$^3$ for aluminium vapor plasma. For the plasma bulk velocity the trend is opposite. The maximum steady-state bulk speed of 4704.17 m/s occurs in case of aluminium vapor plasma and it is almost a factor of 3 higher than that of the minimum bulk velocity 1678.86 m/s in the case of tungsten.

**Table 6.8** Bulk flow parameter values at steady-state subsonic Condition inside the chamber

| Metals | T (eV) | P ( MPa) | ρ (kg/m$^3$) | $V_{bulk}$ (m/s) |
|---|---|---|---|---|
| **W** | 2.005 | 131.89 | 149.64 | 1678.86 |
| **Mo** | 1.642 | 129.70 | 80.21 | 2494.98 |
| **Fe** | 1.601 | 137.67 | 50.21 | 3095.51 |
| **Cr** | 1.505 | 135.82 | 44.77 | 3360.71 |
| **Ti** | 1.636 | 124.05 | 33.16 | 3576.98 |
| **Al** | 1.547 | 134.69 | 20.07 | 4704.17 |

In order to calculate the erosion thickness ($\Delta x$) of the metallic sleeves used in the simulation experiment to predict the extent of damage on the plasma facing surfaces prior to the supersonic expansion of the arc-ablated partially ionized aerosol mass, a new mathematical formula based on simple mass balance has been introduced:

$$M_{abl} = 2\pi \left(r_c + \frac{\Delta x}{2}\right) \Delta x \, L \, \rho_{Metal} \tag{6.3}$$

where, $r_c$ is the inner radius of the capillary sleeve; $\Delta x$ is the erosion thickness, $L$ is the effective length of the capillary that is exposed to the radiant heat flux, $\rho_{Metal}$ is the density of the metal used in the ablative sleeve and $M_{abl}$ is the ablated mass as predicted by the ETFLOW plasma code [7]. Equation 3 leads to the following quadratic equation, which gives the erosion thickness for a particular metal exposed to radiant heat flux at a certain peak discharge current:

$$\frac{(\Delta x)^2}{2} + r_c \, \Delta x - \frac{M_{abl}}{(2\pi \, L \, \rho_{Metal})} = 0 \tag{6.4}$$

All the lengths are in *meter*, density is in $kgm^{-3}$, ablated mass is in $kg$. The data presented in Tables 6.4 to 6.7 have been used in tandem with Eq. 6.4 to calculate the erosion thickness of the metals of interest for the listed peak current values and are tabulated in Table 6.9 and plotted in Fig. 6.14.

**Table 6.9** Erosion thicknesses of tested metals as a function of discharge current

| $I_{Peak}$ (kA) | $(\Delta x)_W$ μm | $(\Delta x)_{Mo}$ μm | $(\Delta x)_{Fe}$ μm | $(\Delta x)_{Cr}$ μm | $(\Delta x)_{Ti}$ μm | $(\Delta x)_{Al}$ μm |
|---|---|---|---|---|---|---|
| 40 | 46.351 | 48.189 | 45.861 | 45.304 | 56.351 | 60.679 |
| 50 | 59.360 | 61.223 | 57.489 | 56.881 | 70.903 | 77.364 |
| 60 | 71.859 | 74.131 | 69.106 | 68.511 | 85.852 | 93.480 |
| 80 | 96.945 | 100.162 | 92.224 | 91.664 | 116.190 | 125.520 |

As seen from Table 6.9, and Fig. 6.14, the ablated mass increases with the increase in the peak discharge current. The removal thickness is the largest in case of aluminium followed by titanium, chromium, iron, molybdenum and tungsten, respectively. Lesser removal thickness of a metal indicates a lesser extent of surface damage, which intuitively makes it a suitable candidate for being used as a plasma facing component under such high heat-flux conditions. The computational results obtained in this current work are in agreement with recent published experimental and computational research work on erosion of plasma-facing components that suggests tungsten and molybdenum to be good materials among the potentially durable metals which can be used in practical fusion reactors **[19-22].** These results demonstrate the extent of disruption for each of the selected metals, which enables selection of the right metal for a particular plasma-facing component in future fusion reactors, as well as other applications in which metallic components are exposed to high heat flux deposition. As shown in Fig. 6.14, it appears that the erosion is close to linear increase with the increase in the magnitude of the peak discharge current.

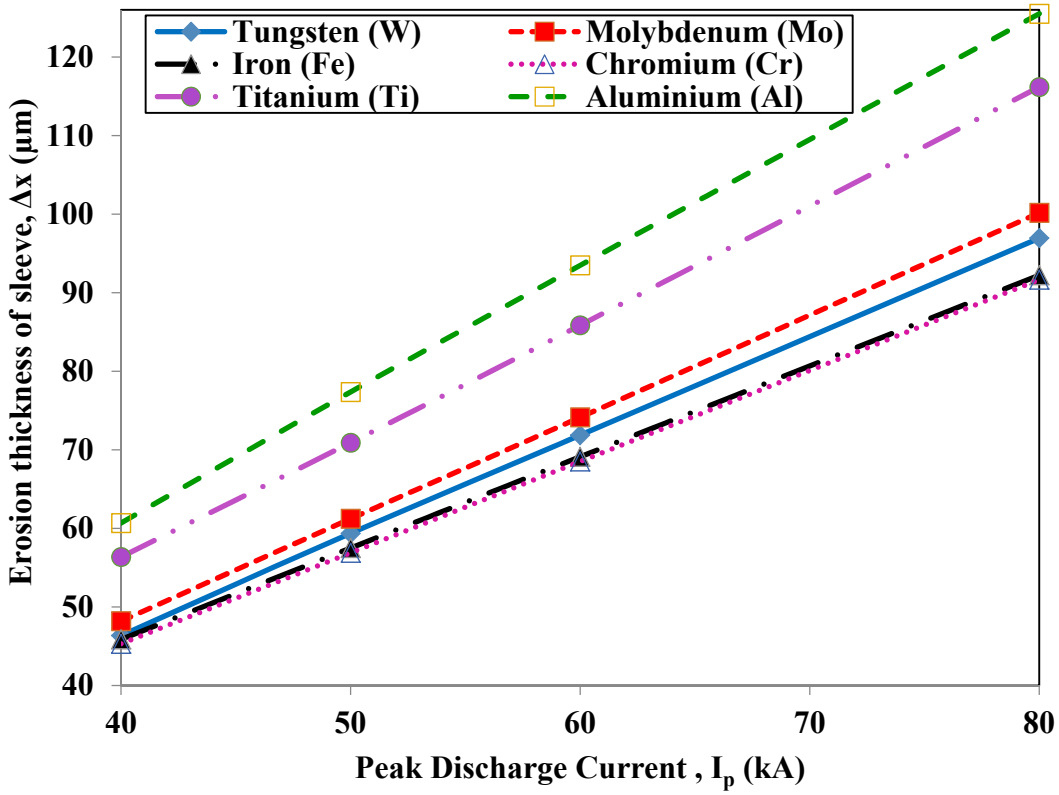


**Fig. 6.14** Erosion thickness (μm) versus peak discharge current (kA)

## 6.4 Effect of non-linearity on tungsten vapor plasma: a specific case

The choice of a capillary running a peak discharge current of 60 kA is an attempt to run at higher current in order to look into non-ideal and non-linear behavior in the flow parameters associated with the adiabatic compressibility index. Tungsten is selected as a case study due to its importance as a potential plasma facing material in the divertor of fusion reactors. It is a material selected in recent research as the armor for the divertor upper vertical target, dome and cassette liner, as well as for lower baffle because of its unique resistance to ion and charge-exchange particle erosion in comparison with other materials **[21].** Tungsten coated surfaces now represent a fraction of 65% of all plasma facing components (~25 $m^2$). The only two other major components that are not yet coated are the strike-point region of the lower divertor as well as the limiters at the low field side **[21, 22].**

Nonlinearity parameters from Tables 6.1 and 6.2, representing Models 1 and 2, respectively, are considered for this specific case of tungsten. Figure 6.15 shows the Mach

number along the axial length for the peak current of 60 kA for Model 1, where it is obvious that the Mach number, being a very strong function of the cross-sectional area, hardly depends on the non-linearities associated with the adiabatic compressibility index and remains almost the same for all the cases, irrespective of the used $\gamma$ model, typical to the behavior previously reported in Ref. 16, 17 and 18.

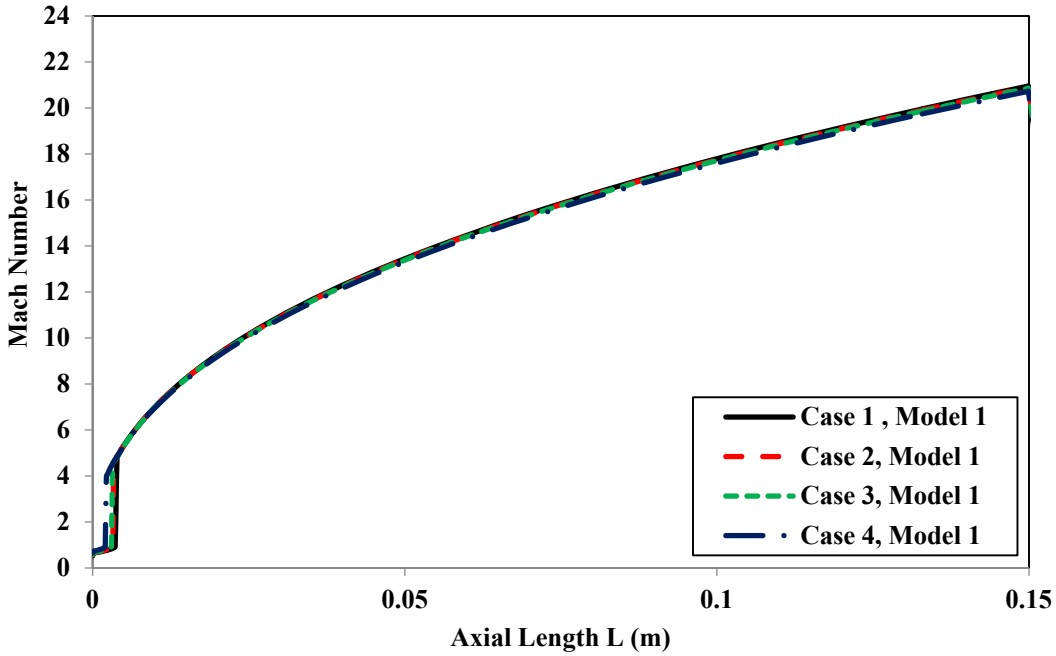


**Fig. 6.15** Mach number along the axial length for a peak discharge current of 60 kA (Model 1)

The results of the tungsten case study will be illustrated for the axial length up to 0.3 meters. Fig. 6.16 shows the plasma bulk density along the axial length for I=60 kA using Model 1, where it is obvious that non-linearity and non-ideal effects can considerably affect the supersonic flow of the metal vapor bulk plasma. The plasma bulk density drops fast in the converging nozzle then rises in the conversing section and reaches steady state in the expansion chamber. The same behavior is also typical when using Model 2 as illustrated in Fig. 6.17.

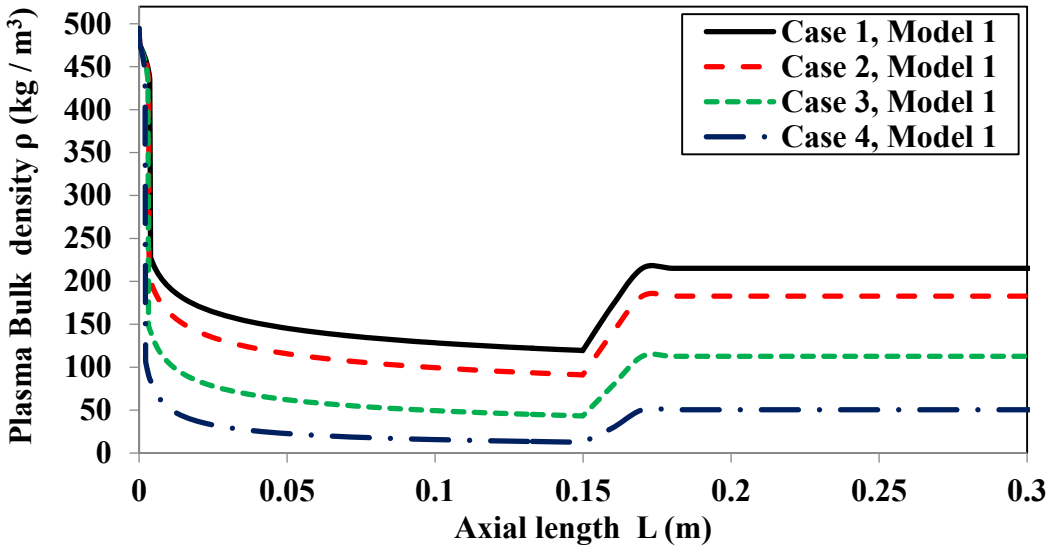


**Fig. 6.16** Plasma bulk density along the axial length for I=60 kA (Model 1)

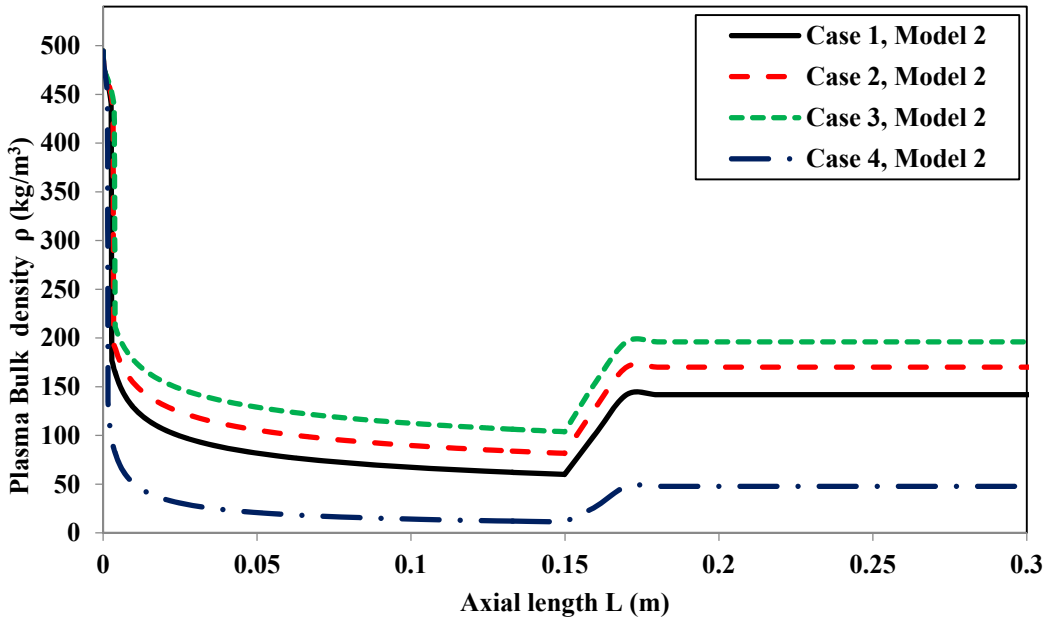


**Fig. 6.17** Plasma **b**ulk density along the axial length for I=60 kA (Model 2)

Similar behavior is also seen in the pressure profiles along the axial direction when using Model 1 (Fig. 6.18) and Model 2 (Fig. 6.19). The pressure drops fast in the transition section, rises at entry to the chamber and remains at a steady state through the expansion volume. However, this is not the case for the plasma bulk velocity as it increases in the transition section then drops to a steady state value into the expansion volume, as seen in Fig. 6.20 (Model 1) and Fig. 6.21 (Model 2).

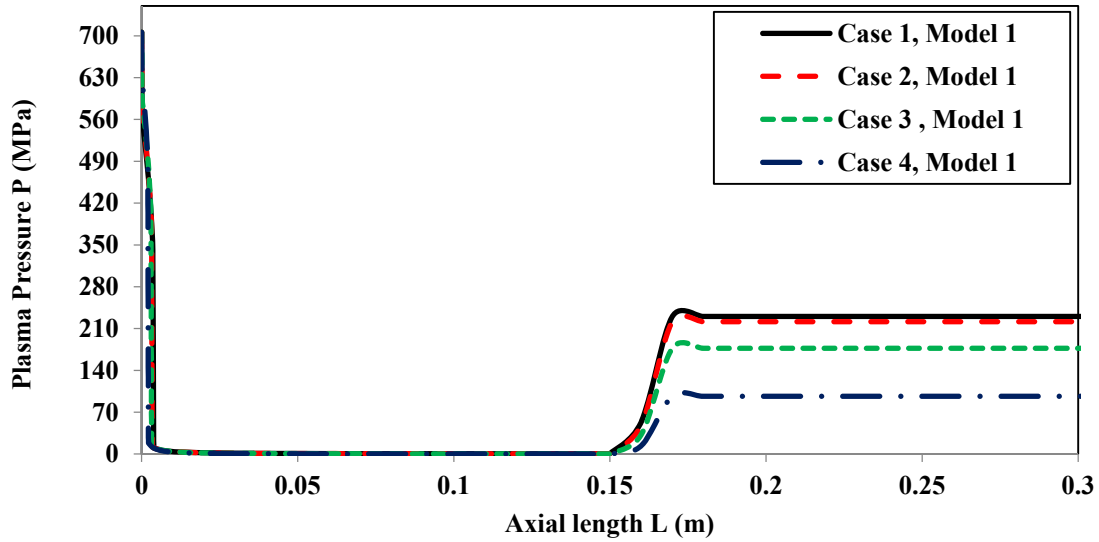


**Fig. 6.18** Plasma pressure along the axial length for I=60 kA (Model 1)

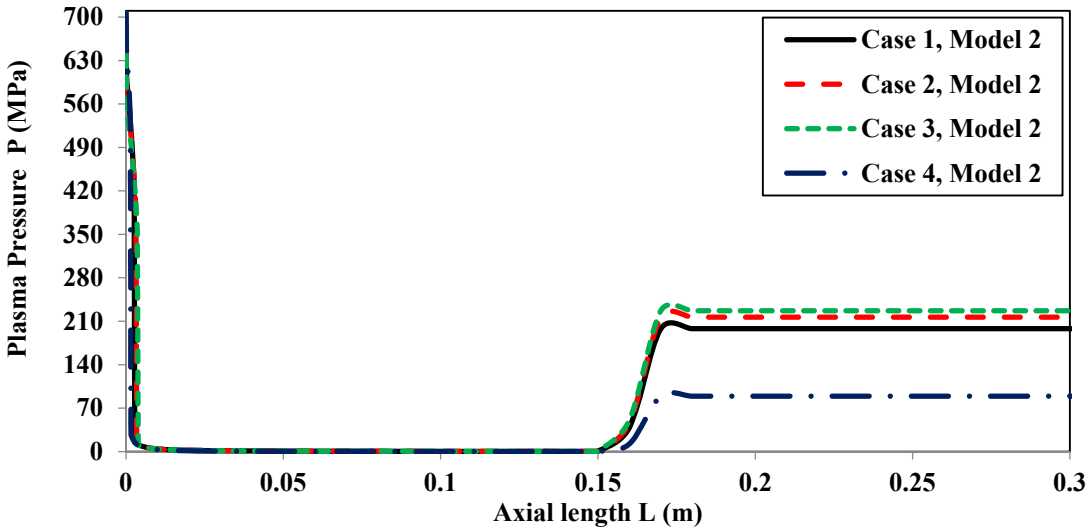


**Fig. 6.19** Plasma pressure along the axial length for I=60 kA (Model 2)

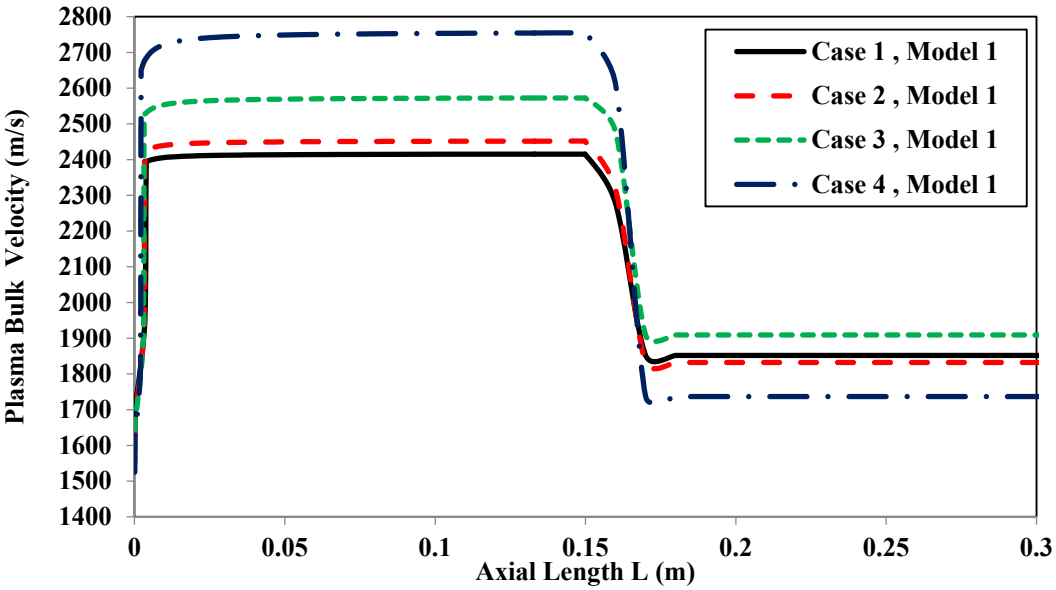


**Fig. 6.20** Plasma bulk velocity along the axial length for I=60 kA (Model 1)

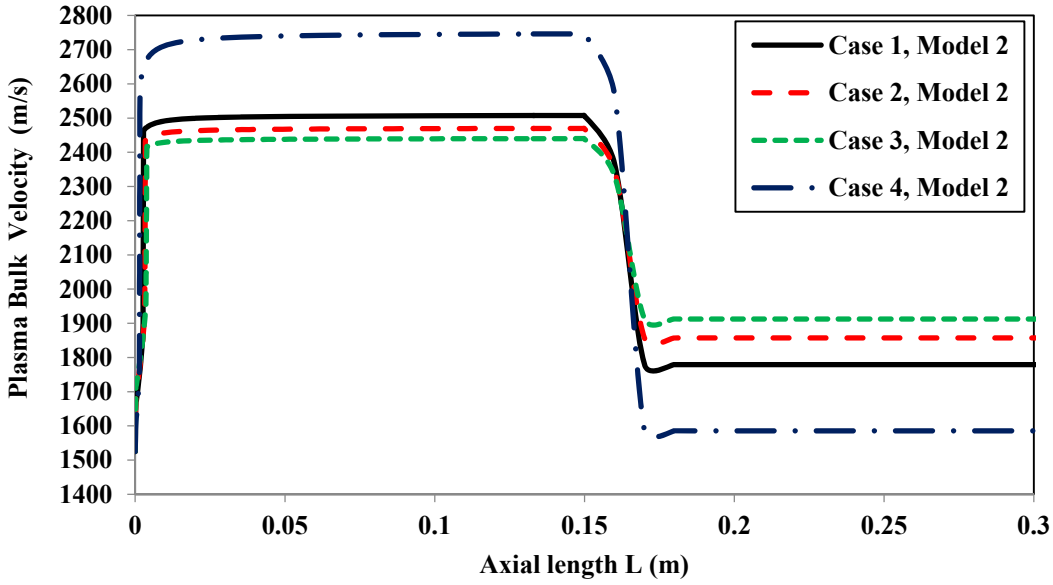


**Fig. 6.21** Plasma pressure along the axial length for I=60 kA (Model 2)

Plasma temperature, as seen in Fig. 6.22 (Model 1) and Fig. 6.23 (Model 2), follows the same behavior of density and pressure, it drops fast in the transition section, rises at entry to the chamber and remains at a steady state through the expansion volume. This behavior is expected due to the fact that the plasma kinetic pressure is dependent on both density and

temperature. Tables 6.10 and 6.11 summarize the results of the parameters for each of the four cases when using Model 1 (Table 6.10) and Model 2 (Table 6.11).

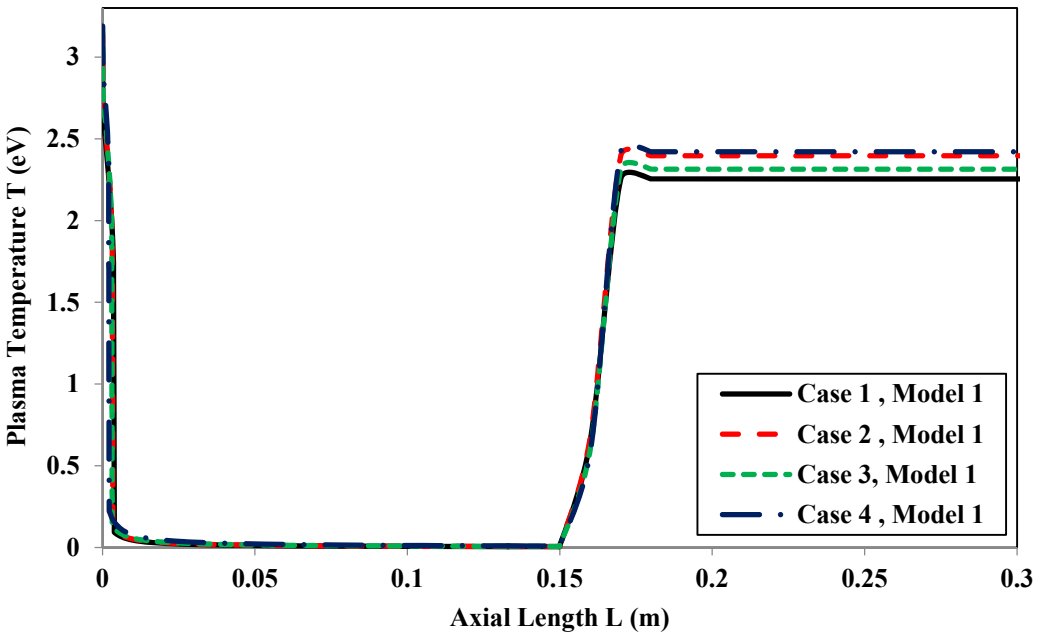


**Fig. 6.22** Plasma temperature along the axial length for I=60 kA (Model 1)

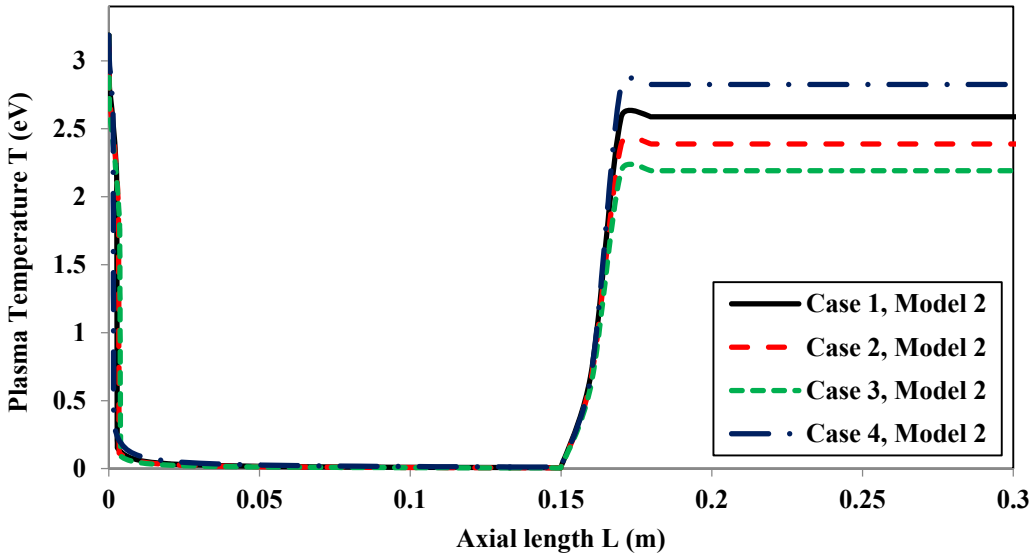


**Fig. 6.23** Plasma temperature along the axial length for I=60 kA (Model 2)

**Table 6.10:** Bulk flow parameter at steady-state subsonic condition inside the chamber for γ Model 1 using capillary exit data corresponding to $I_{peak}$ = 60 kA

| **Steady-state Flow parameters** | **Case 1** | **Case 2** | **Case 3** | **Case 4** |
|---|---|---|---|---|
| **T (eV)** | 2.25500 | 2.39600 | 2.31500 | 2.42100 |
| **P ( MPa)** | 230.162 | 221.504 | 176.989 | 96.5570 |
| **ρ (kg/m$^3$)** | 215.211 | 182.764 | 112.669 | 50.4070 |
| **$V_{bulk}$ (m/s)** | 1851.84 | 1832.11 | 1908.98 | 1736.65 |

**Table 6.11:** Bulk flow parameter at steady-state subsonic condition inside the chamber for γ Model 2 using capillary exit data corresponding to $I_{peak}$ = 60 kA

| **Steady-state Flow parameters** | **Case 1** | **Case 2** | **Case 3** | **Case 4** |
|---|---|---|---|---|
| **T (eV)** | 2.58800 | 2.38800 | 2.19100 | 2.8260 |
| **P ( MPa)** | 197.988 | 216.557 | 226.909 | 89.345 |
| **ρ (kg/m$^3$)** | 141.786 | 170.105 | 196.082 | 47.779 |
| **$V_{bulk}$ (m/s)** | 1779.27 | 1857.04 | 1912.67 | 1585.69 |

As has been seen in Figures 6.16 to 6.23 it is obvious that non-linearity and non-ideal effects can affect the supersonic flow. All the bulk flow parameters exhibit significant changes, however plasma bulk temperature has been found to be least affected by the non-linear changes in the adiabatic compressibility index (γ) of the bulk plasma. In case of Model 1, extreme cases may see a swing in steady-state plasma bulk temperature by as much as 7.36%, whereas in case of Model 2 this swing has been observed to increase up to 28.982% with respect to the lower end value, the actual differences being not too large. Plasma bulk density and plasma pressure have been observed to get affected by a large amount due to the non-linear effects. Steady-state plasma bulk density has been observed to differ by a significant amount; about a factor of 4.27 in case of Model 1, and by a factor of 4.10 in case of Model 2, the lowest bound being the reference point of the respective computational instances. Plasma pressure in the expansion chamber has been observed to differ by a factor of 2.38 in case of Model 1, and by a factor of 2.54 in case of Model 2, in each of the

instances the lowest pressure being the reference point. Plasma bulk velocity, however exhibits a much lower sensitivity towards these non-ideal and non-linear effects. In case of Model 1, extreme case values differ by 9.92% and the difference goes up to 20.62% in case of Model 2. As the bulk velocity ($V$) is dictated by the sonic speed ($a$) at a certain temperature ($T$), pressure ($P$), and density ($\rho$); thus it depends also on the value of γ. The Mach number is $Ma = V/a$ , where $a = (\gamma P/\rho)^{1/2}$.

In the present set-up, the steady-state subsonic flow inside the expansion chamber is characterized by a constant Mach number ($Ma \approx 0.6 - 0.7$) irrespective of the various cases demonstrated in this work. Thus clearly it can be seen that for our purpose - $V \propto (\gamma P/\rho)^{1/2}$ . From the models of adiabatic compressibility index, it can be seen that $(\gamma)^{1/2}$ does not differ much in the various cases of interest, even if the extreme limits are considered. Thus steady–state plasma velocity is dictated by the ratio of the plasma bulk pressure to the plasma bulk density. The higher the value of $(P/\rho)$ ratio, the greater is the steady-state bulk velocity Lower values of $\rho$ in some cases indicate that there may be higher rate of recombination, cluster formation, or agglomeration in occasional instances resulting in an unexpected drop in the plasma bulk density, which results in a proportional decrease in the plasma pressure. These are the form of in-system physical hindrances which essentially slows down the steady state plasma flow. The minor changes in plasma bulk temperature indicate that the processes are energetically stable and consistent. Nevertheless, the non-linear effects help in determining the safety factor in designing the active volume as it should be able to hold the plasma with a sufficiently high bulk pressure.

## 6.5 Conclusions

In this work the effect of temperature-dependent adiabatic compressibility index on the supersonic plasma jet generated from arc-ablated metal sleeves has been investigated. Looking at the disruptive nature, one can decide upon proper metals for the plasma-facing components. Additionally added safety can also be ensured as nonlinearities have been taken into account to some extent. The observed deviation is attributed to the added parameters but helped to have an insight towards 1-D expansion behavior of moderately temperate metal vapor plasmas

## 6.6 References


[1] J. Gilligan, M. Bourham, The use of an electrothermal plasma gun to simulate the extremely high heat flux conditions of a tokamak disruption, J. Fusion Energy, **12(3)**, 311-316 (1993)

[2] S. V. Kukhlevsky et al, Generation of pure, high-density metal-vapor plasma by capillary discharge, Applied Phys. Letters, **74(19)**, 2779-2781(1999)

[3] L. L. Raja, P. L Varghese, Modeling of the electrothermal Ignitor metal vapor plasma for electrothermal-chemical guns, IEEE Trans. Magnetics, 33(1), 316-321 (1997)

[4] G. J. Dunn, S. D. Allemand, T. W. Eagar, Metal vapors in gas tungsten arcs: Part I. spectroscopy and monochromatic photography, Metallurgical Transactions A, **17A**, 1851-1863 (1986)

[5] J. Kutzner, Metal vapor plasma jets in the high-current vacuum arcs, Proc. ISDEIV, XVIIth International Symp. on Discharges and Electrical Insulation in Vacuum, 21-26 July 1996, Berkeley, CA, **1**, pp. 99-103 (1996)

[6] G. E. Dale, M. A. Bourham M.A, Melt-layer erosion and resolidification of metallic plasma-facing components', Proc. 17th IEEE NPSS Symposium on Fusion Engineering, 6-10 October 1997, San Diego, CA, **2**, 892-895 (1997)

[7] L. Winfrey, J. Gilligan, A. Saveliev, M. Abd Al-Halim, M. Bourham, A study of plasma parameters in a capillary discharge with calculations using ideal and non-ideal plasma models for comparison with experiment, IEEE Trans. Plasma Science, 40(3), 843-852 (2012)

[8] P. Sigmund, I. S. Bitensky, J. Jensen, Molecule and cluster bombardment: energy loss, trajectories and collision cascades, Nuclear Instruments and Methods in Physics research B, **112(1-4)**, 1-11(1996)

[9] C. W. Bauschlicher, L. A. Barnes, P. R. Taylor, Lowest ionization potentials of $Al_2$**,** J. Phys. Chem, **93**, 2932-2935 (1989)

[10] A. Kalemos, A. Mavridis, The electronic structure of $Ti_2$ and $Ti_2^+$', J. Chem. Phys., 135, 134302 (1-8) (2011)

[11] A. E. Kramida, J. Reader, Ionization energies of tungsten ions: $W^{2+}$ through $W^{72+}$, Atomic Data and Nuclear Data Tables, **92**, 457- 479 (2006)

[12] V. D. Lakhno (Ed.) , G. N. Chuev (Ed.), Physics of Clusters, World Scientific Publishing Co. Pte. Ltd. (1998)

[13] P. D. Desai, Thermodynamic properties of manganese and molybdenum, J. Phys. Chem. Ref. Data, **16(1)** , 91-108 (1987)

[14] J. C. Slater, Atomic shielding constants, Physical Review, **36**, 57-64 (1930)

[15] E. Clementi, D. L. Raimondi, W. P. Reinhardt, Atomic screening constants from SCF functions. II. atoms with 37 to 86 electrons, Journal of Chem. Physics, **47 (4)** , 1300-1307 (1967)

[16] R. Majumdar, J. G. Gilligan, A. L. Winfrey, M. A. Bourham**,** Supersonic flow patterns from electrothermal plasma source for simulated ablation and aerosol expansion following a fusion disruption, J. Fusion Energy, **33(1)**, 25-31 (2014)

[17] R. Majumdar, J. G. Gilligan, A. L. Winfrey, M. A. Bourham., Scaling laws of bulk plasma parameters for a 1-D flow through a capillary with extended converging-diverging nozzle for simulated expansion into fusion reactor chamber, J. Fusion Energy , **34(4)**, 905-910 (2015)

[18] R. Majumdar, M. A. Bourham, Effect of plasma temperature and nonlinearity of the Adiabatic Compressibility index on flow parameters for hypersonic aerosol expansion following a plasma disruption, J. Fusion Energy, Published Online 27 June, 2015, DOI: 10.1007/s10894-015-9960-1.

[19] A. Hassanein, Prediction of material erosion and lifetime during major plasma instabilities in tokamak devices, Fusion Engineering and Design, **60**, 527–546 (2002).

[20] H. Bolt, V. Barabash, W. Krauss, J. Linke, R. Neu, S. Suzuki, N. Yoshida, ASDEX Upgrade Team, Materials for the plasma-facing components of fusion reactors, J. Nuclear materials, 329-333, Part A, 66-73 (2004)

[21] R. Neu et al, 'Tungsten: an option for divertor and main chamber plasma facing components in future fusion devices, Nuclear Fusion, **45**, 209 -218 (2005)

[22] J. Linke, High heat flux performance of plasma facing materials and components under service conditions in future fusion reactors, Fusion Science and Technology, 57(2T), 293-302 (2010)

# 7

# Radial Profile of Plasma Flow Parameters inside a Supersonic Nozzle Expanding into Large Volume Simulating Fusion Reactor Vacuum Vessel

The 1-D, steady state analysis of the plasma flow from an electrothermal source into a large volume via a supersonic throat assumes the plasma parameters to vary only in the axial direction with a uniform radial distribution. The 2-D evolution of the plasma as it expands outside the source capillary and the throat is of importance to investigate the scaling laws with inclusion of radial variations. As the plasma expands towards the sidewalls of the diverging section in the transition region, the bulk plasma has a finite chance to lose energy primarily in the form of heat loss, which might cause readjustment in the profile for plasma bulk temperature giving rise to a decreasing trend in the radial direction. This change in bulk plasma temperature triggers further changes in other bulk flow parameters along the radial directions, away from the axis of the flow. In this work, different mathematical models have been proposed for radial correction in the bulk flow parameter profiles within the system size as a simulation for expansion into the vacuum vessel of a magnetic fusion reactor. Symmetry of the radial profiles over a cross-sectional area has been assumed to facilitate ease of computation and analysis.

## 7.1 Introduction

Capillary discharges are considered good simulators for generating plasma particulates flowing out of the source with hyper velocities for various applications such as launchers, thrusters, fusion disruption simulators and high heat flux sources **[1-4].** These capillaries produce electrothermal (ET) plasmas of high-density, high-pressure and hyper velocities and can be modeled as a plasma fluid in 1-D or 2-D, steady state or time-dependent **[4-8].** The simulation of plasma flow following a disruption has been conducted using the

configuration of an electrothermal (ET) plasma source with a supersonic throat connected at the ET source exit and opens into a large volume representing a fusion reactor vacuum vessel **[9-11].** As the plasma expands in the throat from the converging into the diverging section of the transition region, as well as inside the expansion chamber, it comes into contact with the sidewalls and deposits a fraction of the energy in the form of heat loss to the walls. As a result the bulk temperature of the plasma layer adjacent to the sidewalls decreases faster compared to the plasma residing in the regions closer to the chamber axis, resulting in changes of the bulk plasma temperature profile. It is expected to a steep decrease in the bulk temperature profile near the wall, which leads to the formation of a core and a fringe area in the plasma. As a sufficiently long period of time elapses the profile tends to become more gradual in nature blurring the distinction between the core and fringe areas as the plasma thermally stabilizes itself towards an equilibrium state. The above wall effect is more pronounced for small narrow-type expansion chambers whereas a more gradual and diffusive expansion is expected in bigger chambers where the expanding plasma does not readily come into contact with the walls. Upon losing the heat energy through dissipation, and as the plasma starts cooling down, the chances for recombination of the ion-electron pairs will become higher. As the ion density decreases, the plasma bulk density also decreases, which causes a drop in the plasma kinetic pressure as $P \propto N_p k_B T$; $k_B$= Boltzmann's Constant, $N_p$ is number density and $T$ is plasma temperature) **[5, 6].** The decrease in the plasma temperature in the radial direction decreases the plasma bulk velocity, and such decrease is not expected to be linear.

Radial variation is proposed herein for the plasma bulk flow parameters in the converging-diverging transition region as well as inside the large expansion chamber. A new variable called *radial scale length* ($r_{scale}$) has been defined, which is basically a radial distance measured from the axis over which the plasma bulk flow parameters remain radially unchanged and decrease thereafter. The extent of radial decrease in the values of the flow parameters is dictated by some other parametric constants, which are to be chosen intuitively and realistically based on the data collected from an experimental set-up. Additionally, a quantity named as *scale length ratio* (R) has been defined which has been presented as the

pivotal element on which various mathematical formalisms prescribed for the radial correction of the bulk flow parameters are compared.

The same system geometrical configuration has been used in the current work, as shown in Fig. 1, and as discussed in detail in some of the related earlier works **[9-11].** The radial correction has been included in the 2-D modeling and has been appended to the region-specific 1-D scaling laws, which were presented for the flow of ablated plasma in an earlier work **[10].** The current profile for the PIPE shot P206 has been used as a typical electrothermal plasma discharge when creating the 2-D profiles for the plasma bulk parameters, **[8-10].** In order to maintain the simplicity of the formalism it has been assumed that the axial part and radial parts can be expressed in a variable-separated form as a product of two functions.

## 7.2 Conceptualization of Scale Length Ratio

The new variable, the scale length ratio, is defined as follows –

$$\frac{r_{scale}}{r} = R \tag{7.1}$$

where, r is the radial distance measured from the axis.

This variable has been used to model the radial profile for all the bulk flow parameters, namely plasma bulk density, pressure, kinetic temperature and bulk velocity. In the current work, three kinds of mathematical modeling have been proposed for the radial profiles of interest. Exponential radial profile has been proposed for very dense plasma bulk coming out of the capillary source and expanding thereafter in a barrel-like expansion chamber having a considerably small radius **[12, 13].** In this case the prominent wall effect leading to the formation of core and fringe areas is exhibited as discussed before. For a lesser dense bulk plasma expanding to a medium to large sized expansion volume, a parabolic radial profile has been proposed. In this case the loss-wall effect is present but not to the extent of exhibiting a localized non-equilibrium condition near the wall. For the plasma expansion in a very large volume, like the vacuum vessel of a fusion reactor real-life fusion

reactor **[14],** a power-law radial characteristic has been proposed, which indicates a diffusive expansion towards all directions. In this case the plasma is assumed to be at a fair distance from the wall, and thus there is no pronounced wall effect observed.

Separate sets of equations have been given for the exponential model, power-law model and the parabolic model respectively to describe the decrement in bulk flow parameters when moving away radially from the axis and approaching the system boundary, where the flow bulk parameters have been assumed to be at a considerably lower value near the system boundaries.

### 7.3 Development of Exponential Model

Throughout the current work the axial part for the bulk density, plasma bulk pressure, bulk temperature and plasma bulk velocity are denoted by $Z_\rho(z)$, $Z_P(z)$ , $Z_T(z)$ and $Z_v(z)$ , respectively; and for the same flow parameters the corresponding radial parts are denoted by $R_\rho(r)$, $R_P(r)$, $R_T(r)$ and $R_v(r)$, respectively. The two-dimensional representations for the flow parameters of interest are given by $F_\rho(r,z)$, $F_P(r,z)$, $F_T(r,z)$ and $F_v(r,z)$, respectively and they are expressed mathematically as the product of the corresponding radial and axial parts.

The 2-D mathematical expressions for the above mentioned flow parameters are as follows-

$$\left.\begin{aligned} F_T(r,z) &= Z_T(z) \\ F_\rho(r,z) &= Z_\rho(z) \\ F_P(r,z) &= Z_P(z) \\ F_v(r,z) &= Z_v(z) \end{aligned}\right\}; \qquad (7.2)$$

$$\{R \geq 1 \text{ and } 0 \leq Z \leq 0.4 \text{ (meters)}\}$$

Assuming the first 250 mm long expansion chamber, the total effective length starting at the capillary exit up to the end of the expansion chamber becomes 400 mm.

$$\left.\begin{aligned} F_T(r,z) &= \exp\left(\frac{-a_1'}{R}\right) * Z_T(z) \\ F_\rho(r,z) &= \exp\left(\frac{-b_1'}{R}\right) * Z_\rho(z) \\ F_P(r,z) &= \exp\left(\frac{-(a_1'+b_1')}{R}\right) * Z_P(z) \\ F_v(r,z) &= \exp\left(\frac{-c_1'}{R}\right) * Z_v(z) \end{aligned}\right\}; \quad (7.3)$$

$$\{R < 1 \; and \; 0 \leq Z \leq 0.004 \text{ (meters)}\}$$

$$\left.\begin{aligned} F_T(r,z) &= \exp\left(\frac{-a_2'}{R}\right) * Z_T(z) \\ F_\rho(r,z) &= \exp\left(\frac{-b_2'}{R}\right) * Z_\rho(z) \\ F_P(r,z) &= \exp\left(\frac{-(a_2'+b_2')}{R}\right) * Z_P(z) \\ F_v(r,z) &= \exp\left(\frac{-c_2'}{R}\right) * Z_v(z) \end{aligned}\right\}; \quad (7.4)$$

$$\{R < 1 \; and \; 0.004 < Z \leq 0.4 \text{ (meters)}\}$$

The exponential terms in the radial expressions for plasma pressure in Eqs. (7.3) and (7.4) are coming from the equation of state. It is needed to formulate values of the six different proposed constants in order to demonstrate radial variations. In the physical domain $0 \leq Z \leq 0.004$ (meters), if $r_{scale} < r_{micronozzle}$ where $r_{micronozzle} = 0.002m$ is the capillary radius i.e. R<1, and hence must set some conditions in order to solve for the constants given in Eq. (7.3), and the following has been assumed,

$$\left.\begin{aligned} F_T(r_{nozzle},z) &= 0.9 * F_T(r_{scale},z) \\ F_\rho(r_{nozzle},z) &= 0.95 * F_\rho(r_{scale},z) \end{aligned}\right\} \quad (7.5)$$

If considering the bulk velocity to be primarily consisted of thermal speed, then it is indeed the manifestation of the local plasma bulk temperature, and hence it may be concluded that the exponential may be expressed as follow:

$$\left.\begin{aligned} \exp\left(\frac{-\mathrm{a}_1'}{\left(\frac{r_{scale}}{r_{micronozzle}}\right)}\right) = 0.9\ ;\ i.e.\ \mathrm{a}_1' = -\log_{\mathrm{e}} 0.90 * \left(\frac{r_{scale}}{r_{micronozzle}}\right) \\ \exp\left(\frac{-\mathrm{b}_1'}{\left(\frac{r_{scale}}{r_{micronozzle}}\right)}\right) = 0.95\ ;\ i.e.\ \mathrm{b}_1' = -\log_{\mathrm{e}} 0.95 * \left(\frac{r_{scale}}{r_{micronozzle}}\right) \\ \mathrm{c}_1' = \frac{\mathrm{a}_1'}{2} \end{aligned}\right\} \tag{7.6}$$

In the physical domain $0.004 < Z \leq 0.4$ (meters), it is needed to solve for the parametric constants of Eq. (7.4). Accordingly, the maximum radial stretch of the system ($\mathrm{r_{max}}$), through which the bulk flow passes must be identified. This would correspond to a minimum value of R, given as follows:

$$R_{min} = \frac{r_{scale}}{r_{max}} \tag{7.7}$$

Some fractions $\mathrm{Frac_T}$ and $\mathrm{Frac_\rho}$, were selected to satisfy fractions from scaling:

$$\left.\begin{aligned} F_T(r_{max}, z) = \mathrm{Frac_T} * F_T(r_{scale}, z) \\ F_\rho(r_{max}, z) = \mathrm{Frac_\rho} * F_\rho(r_{scale}, z) \end{aligned}\right\} \tag{7.8}$$

Additionally it is assumed that the thermal speed is the major contributor to the plasma bulk flow speed and thus the formalism will be as follow:

$$\left.\begin{aligned} \exp\left(\frac{-\mathrm{a}_2'}{R_{min}}\right) = \mathrm{Frac_T}\ ;\ i.e.\ \mathrm{a}_2' = -\log_{\mathrm{e}}(Frac_T) * \mathrm{R_{min}} \\ \exp\left(\frac{-\mathrm{b}_2'}{R_{min}}\right) = \mathrm{Frac_\rho}\ ;\ i.e.\ \mathrm{b}_2' = -\log_{\mathrm{e}}(Frac_\rho) * \mathrm{R_{min}} \\ \mathrm{c}_2' = \frac{\mathrm{a}_2'}{2} \end{aligned}\right\} \tag{7.9}$$

The 2-D plots for the plasma parameters of interest are presented. It should be mentioned that the Mach number does not change radially but varies only along the axial direction as the bulk plasma flows through the transition region and settles to a subsonic steady state inside the expansion chamber. Figures 7.1 through 7.5 show the surface plots of the plasma parameters as a function of the axial distance traversed as well as the radial stretch it reaches,

as the high pressure jet coming out of the source capillary expands and evolves into the bigger volume. The values of the parameters used to simulate the 2-D profile in the exponential radial model are tabulated in Table 7.1. In this present analysis $\mathrm{r_{scale}} = 0.0022\ \mathrm{m}$; $\mathrm{Frac_T} = 0.5$ and $\mathrm{Frac_\rho} = 0.5$ and $\mathrm{r_{max}} = 0.2541\ m$ from the system specification and hence $R_{min} = 0.0087m$. Thus one can calculate the required parametric constants for a specific case of interest.

**Table 7.1** Parameter values corresponding to the model for exponential radial profile

| Model Parameters | $\mathbf{a_1'}$ | $\mathbf{b_1'}$ | $\mathbf{c_1'}$ | $\mathbf{a_2'}$ | $\mathbf{b_2'}$ | $\mathbf{c_2'}$ |
|---|---|---|---|---|---|---|
| Test Values | 0.1159 | 0.0564 | 0.058 | 0.006 | 0.006 | 0.003 |

The Mach number remains radially unchanged as expected, as it can be seen in Fig. 7.1. The plasma pressure profile has the steepest decreasing profile as it combines the decreasing trends of both plasma bulk temperature and bulk density. The bulk velocity profile has the least amount of radial variation compared to other flow bulk parameters, the basis of comparison being the relative change in magnitude, compared to the respective axial values.

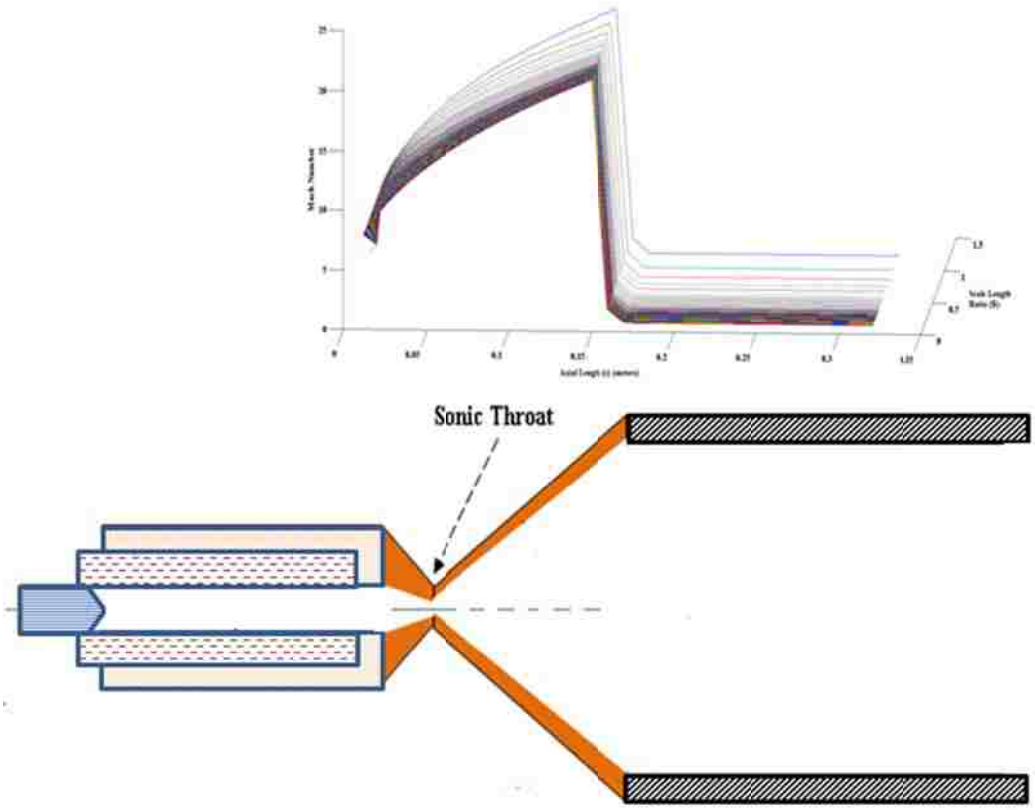


**Fig. 7.1** Two-dimensional profile for Mach number in the throat and the expansion volume

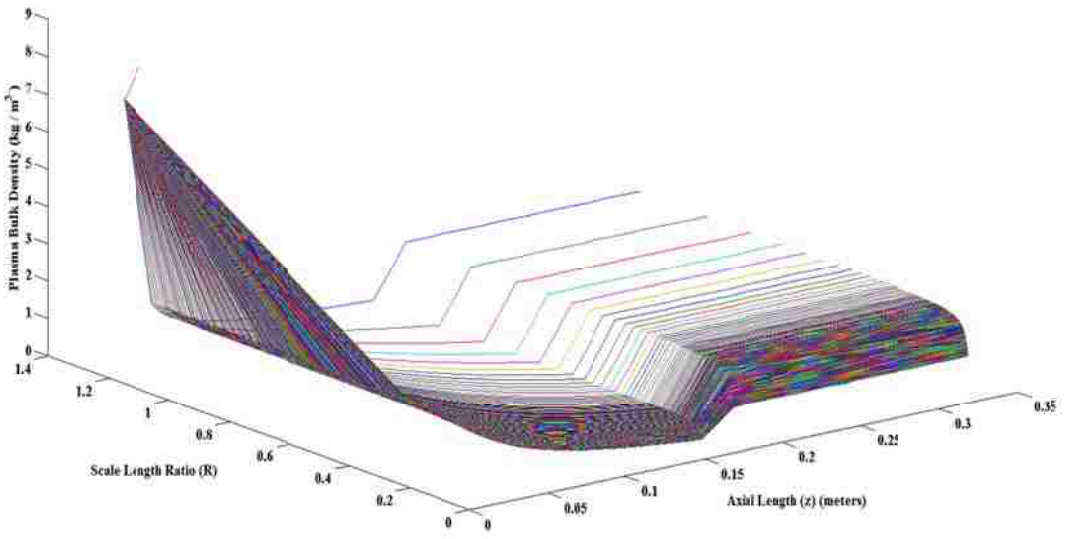


**Fig. 7.2** Two-dimensional profile for plasma bulk density in the throat and the expansion volume (exponential model)

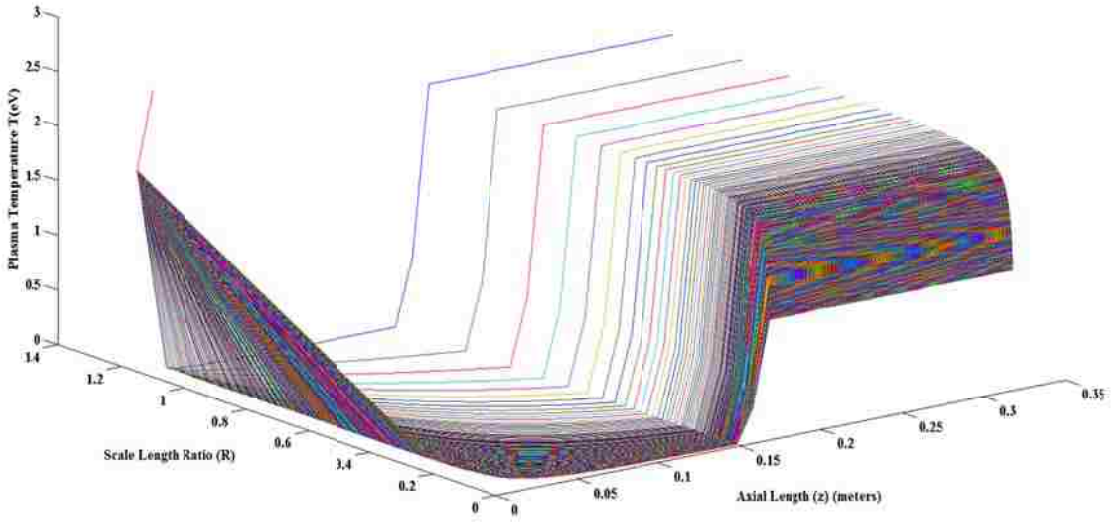


**Fig. 7.3** Two-dimensional profile for plasma temperature in the throat and the expansion volume (exponential model)

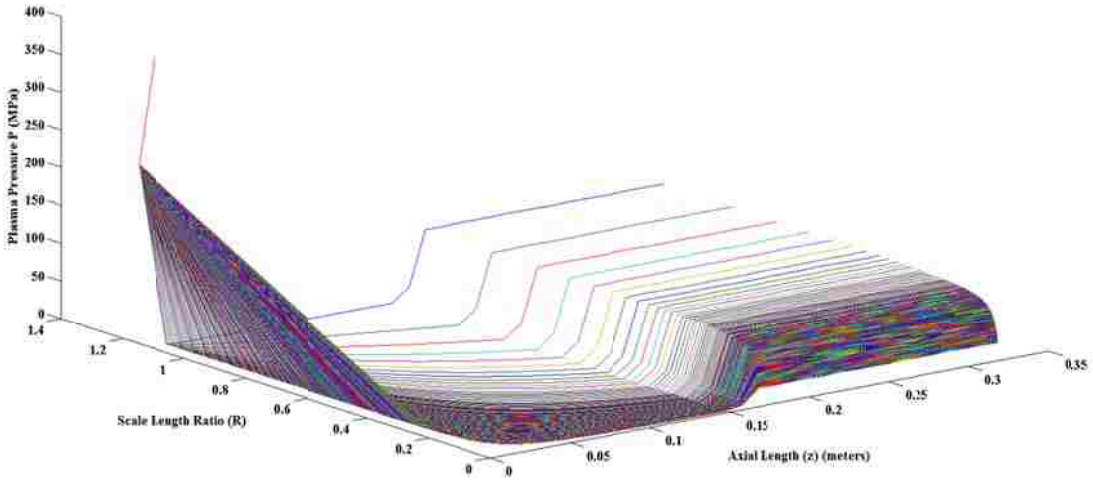


**Fig. 7.4** Two-dimensional profile for plasma pressure in the throat and the expansion volume (exponential model)

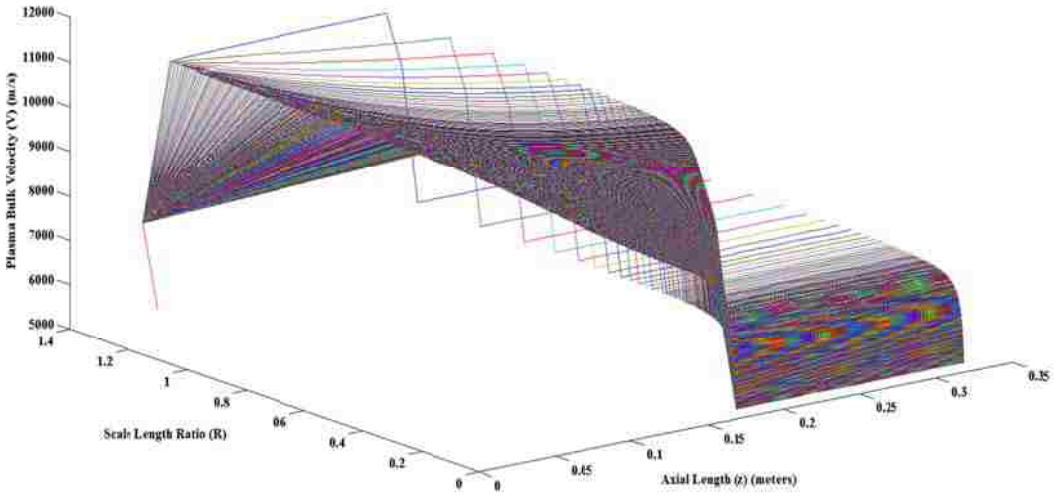


**Fig. 7.5** Two-dimensional profile for plasma bulk velocity in the throat and the expansion volume (exponential model)

## 7.4 Development of Power-law Model

The power-law model has been proposed as a relevant alternative to the exponential model to describe the radial profile. Both models can be useful in specific situations describing important characteristics of a particular system suitable for some particular applications. It is to be mentioned that closure 2 of the exponential model is also applicable for the power-law model with no changes in it. For R<1 the mathematical expressions for the 2-D functions of interest are given below:

$$\left.\begin{aligned} F_T(r,z) &= \mathrm{R}^{a_1} * Z_T(z) \\ F_\rho(r,z) &= \mathrm{R}^{b_1} * Z_\rho(z) \\ F_P(r,z) &= \mathrm{R}^{(a_1+b_1)} * Z_P(z) \\ F_v(r,z) &= \mathrm{R}^{c_1} * Z_v(z) \end{aligned}\right\}; \quad \{\mathrm{R} < 1 \; and \; 0 \le Z \le 0.004 \text{ (meters)}\} \tag{7.10}$$

$$\left.\begin{aligned} F_T(r,z) &= \mathrm{R}^{a_2} * Z_T(z) \\ F_\rho(r,z) &= \mathrm{R}^{b_2} * Z_\rho(z) \\ F_P(r,z) &= \mathrm{R}^{(a_2+b_2)} * Z_P(z) \\ F_v(r,z) &= \mathrm{R}^{c_2} * Z_v(z) \end{aligned}\right\}; \quad \{\mathrm{R} < 1 \; and \; 0.004 < Z \le 0.4 \;\; \text{(meters)}\} \tag{7.11}$$

The parameters used as exponents on $R$ in each of the expressions give the intended radial corrections for the respective plasma flow parameters. The power-law terms in the radial expression for plasma pressure in Eqs. (7.10) and (7.11) are from the equation of state.

It is essential to formulate the value of the parametric constants $a_1, b_1, c_1, a_2, b_2 \; and \; c_2$ proposed in the formalism in order to demonstrate 2-D distribution of the bulk plasma flow in terms of its major attributes of interest.

In the physical domain $0 \leq \mathrm{Z} \leq 0.004$ (meters), if $\mathrm{r_{scale}} < \mathrm{r_{micronozzle}}$ where $\mathrm{r_{micronozzle}} = 0.002\mathrm{m}$ is the capillary radius, i.e. R<1, and hence must set some conditions in order to solve for the constants given in Eqs. (7.10) and (7.11), and the following has been assumed, and the conditions are same as those given in Eq. (7.8). Moreover one of the major physical assumptions is that the local plasma velocity to be dictated by the local kinetic temperature of the plasma. Thus the plasma velocity is expected to vary as the square root of the plasma temperature. Taking into account the above statements and using Eq. (7.7), one gets:

$$\left.\begin{aligned} \left(\frac{\mathrm{r_{scale}}}{\mathrm{r_{nozzle}}}\right)^{\mathrm{a_1}} = 0.9 \; ; \; i.e. \; \mathrm{a_1} = \frac{\log_e 0.9}{\log_e\left(\frac{\mathrm{r_{scale}}}{\mathrm{r_{nozzle}}}\right)} \\ \left(\frac{\mathrm{r_{scale}}}{\mathrm{r_{nozzle}}}\right)^{\mathrm{b_1}} = 0.95; \; i.e. \; \mathrm{b_1} = \frac{\log_e 0.95}{\log_e\left(\frac{\mathrm{r_{scale}}}{\mathrm{r_{nozzle}}}\right)} \\ \mathrm{c_1} = \frac{\mathrm{a_1}}{2} \end{aligned}\right\} \tag{7.12}$$

and

$$\left.\begin{aligned} \left(\frac{\mathrm{r_{scale}}}{\mathrm{r_{max}}}\right)^{\mathrm{a_2}} = Frac_T \; ; \; i.e. \; \mathrm{a_2} = \frac{\log_e(Frac_T)}{\log_e(\mathrm{R_{min}})} \\ \left(\frac{\mathrm{r_{scale}}}{\mathrm{r_{max}}}\right)^{\mathrm{b_2}} = Frac_\rho \; ; \; i.e. \; \mathrm{b_2} = \frac{\log_e(Frac_\rho)}{\log_e(\mathrm{R_{min}})} \\ \mathrm{c_2} = \frac{\mathrm{a_2}}{2} \end{aligned}\right\} \tag{7.13}$$

The test parameter values used to create the 2-D plots for the plasma parameters with the gradually diminishing radial profile following a power-law trend are listed in Table 7.2. For the analysis with power-law model, it was chosen to have $\mathrm{r_{scale}} = 0.0022$ m , $\mathrm{Frac_T} = 0.5$ and $\mathrm{Frac_\rho} = 0.5$, and $\mathrm{r_{max}} = 0.2541\, m$ from system specification, and hence $R_{min} = 0.0087$, as previously calculated for the exponential model. Hence, one can compute the case

specific values of the parametric constants for the power-law radial profiles. Figures 7.6-7.9 display the surface plots of the plasma parameters as a function of the axial distance traversed as well as the radial stretch it reaches, as the high pressure jet coming out of the source capillary expands and evolves into the bigger volume.

**Table 7.2** Parameter values corresponding to the model for power-law radial profile

| Model Parameters | $\mathbf{a_1'}$ | $\mathbf{b_1'}$ | $\mathbf{c_1'}$ | $\mathbf{a_2'}$ | $\mathbf{b_2'}$ | $\mathbf{c_2'}$ |
|---|---|---|---|---|---|---|
| Test Values | -1.1054 | -0.5382 | -0.5527 | 0.1461 | 0.1461 | 0.073 |

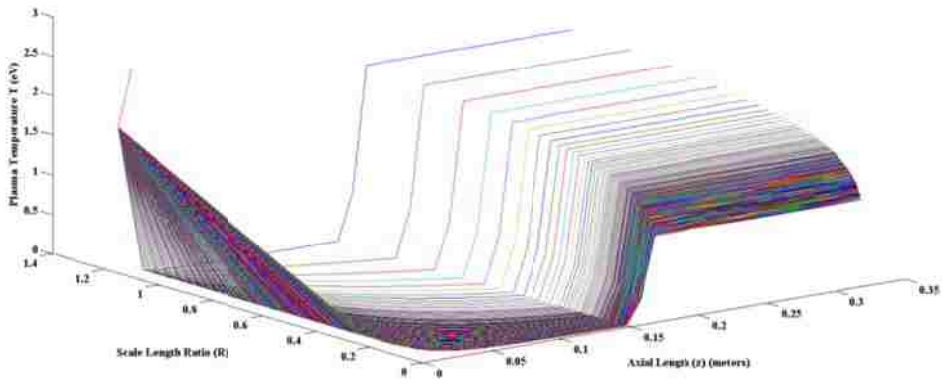


**Fig. 7.6** Two-dimensional profile for plasma temperature in the throat and the expansion volume (power-law model)

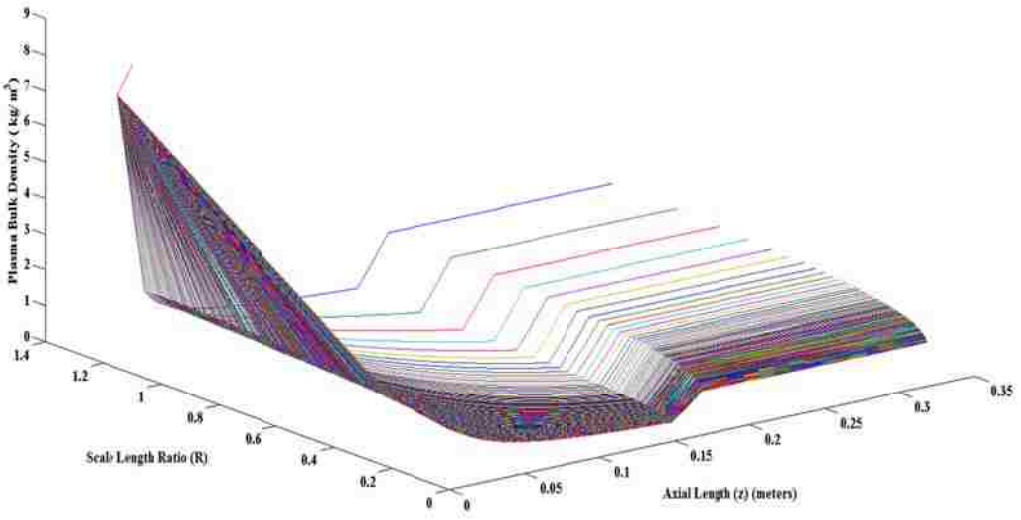


**Fig. 7.7** Two-dimensional profile for plasma bulk density in the throat and the expansion volume (power-law model)

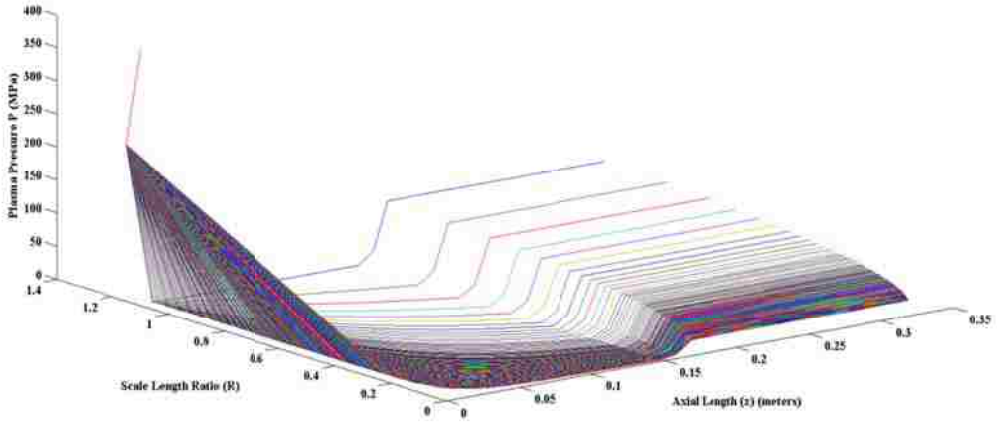


**Fig. 7.8** Two-dimensional profile for plasma bulk pressure in the throat and the expansion volume (power-law model)

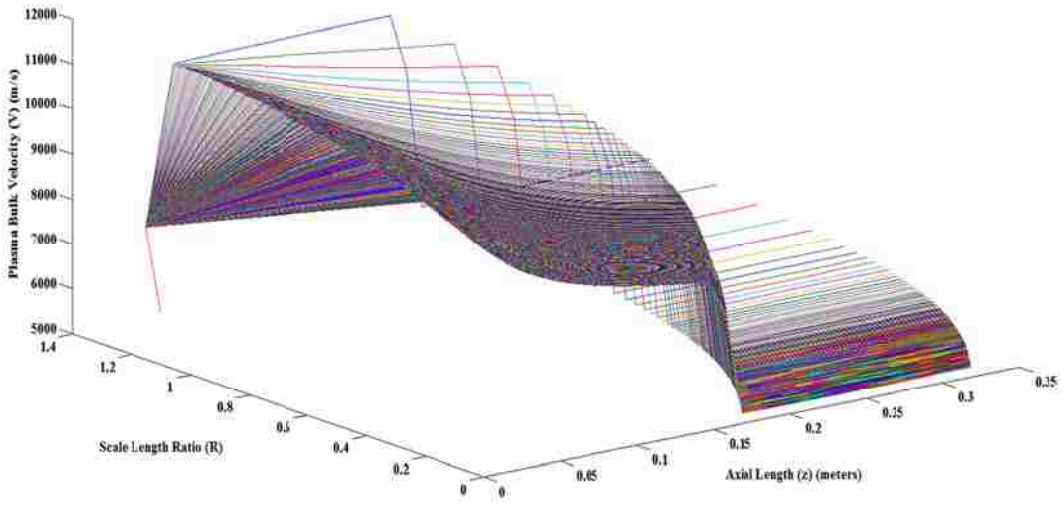


**Fig. 7.9** Two-dimensional profile for plasma bulk velocity in the throat and the expansion volume (power-law model)

## 7.5 Development of Parabolic Model

For the parabolic model a slightly different mathematical approach has been followed. The principal similarity between all the three models is that the plasma bulk flow parameters remain radially unchanged until $\mathrm{r_{scale}}$ and the bulk flow parameters reach global minima at $R = R_{min}$ (i.e. $r = r_{max}$). The formalism for this model has been prescribed as follows:

$$\left.\begin{aligned} F_T(r,z) &= (\mathrm{K_{T,1}} * \mathrm{R}^2 + \mathrm{K_{T,2}} * \mathrm{R} + \mathrm{K_{T,3}}) * Z_T(z) \\ F_\rho(r,z) &= (\mathrm{K_{\rho,1}} * \mathrm{R}^2 + \mathrm{K_{\rho,2}} * \mathrm{R} + \mathrm{K_{\rho,3}}) * Z_\rho(z) \\ F_P(r,z) &= (\mathrm{K_{P,1}} * \mathrm{R}^2 + \mathrm{K_{P,2}} * \mathrm{R} + \mathrm{K_{P,3}}) * Z_P(z) \\ F_v(r,z) &= (\mathrm{K_{v,1}} * \mathrm{R}^2 + \mathrm{K_{v,2}} * \mathrm{R} + \mathrm{K_{v,3}}) * Z_v(z) \end{aligned}\right\}; \quad (7.14)$$

$$\text{for } \{\mathrm{R} < 1 \; and \; 0 < Z \leq 0.4 \text{ (meters)}\}.$$

Additionally, as per the previous assumptions, the boundary conditions at the diverging exit for this case have been formulated as follows:

$$\left.\begin{array}{c} R_T(r = r_{scale}) = R_{T,max} \\ R_\rho(r = r_{scale}) = R_{\rho,max} \\ R_P(r = r_{scale}) = R_{P,max} \\ R_v(r = r_{scale}) = R_{v,max} \\ and \\ R_T(r = r_{max}) = R_{T,min} \\ R_\rho(r = r_{max}) = R_{\rho,min} \\ R_P(r = r_{max}) = R_{P,min} \\ R_v(r = r_{max}) = R_{v,min} \end{array}\right\} . \tag{7.15}$$

Some relevant fractions have been defined based on the ratio of the minimum and the maximum values of the respective plasma parameters, which help in formulating the mathematical expressions required for the parabolic radial profile, along with the boundary conditions needed for the solution. Numerical values for those fractions have to be intuitively chosen in a case-specific manner.

$$\left.\begin{array}{c} \frac{R_{T,min}}{R_{T,max}} = Frac_T \\ \frac{R_{\rho,min}}{R_{\rho,max}} = Frac_\rho \\ \frac{R_{P,min}}{R_{P,max}} = Frac_P \\ \frac{R_{v,min}}{R_{v,max}} = Frac_v \\ and\ additionally\ we\ have\ \ Frac_v = (Frac_T)^{\frac{1}{2}}; \\ \text{(asssuming only thermal component of plasma bulk speed)} \\ Frac_P = Frac_T * Frac_\rho \\ (from\ equation\ of\ state) \end{array}\right\} \tag{7.16}$$

In the vicinity of the radial position $r = r_{scale}$, the profile in general for the plasma flow parameters is expected to be of somewhat flattening nature, such that the derivative of the function representing the radial part at $r = r_{scale}$ can be assumed to be zero. A pictorial representation of how the radial profile might look like with a parabolic approximation is presented herein in Fig. 7.10. For the current work $Frac_T = Frac_\rho = 0.5$ has been set.

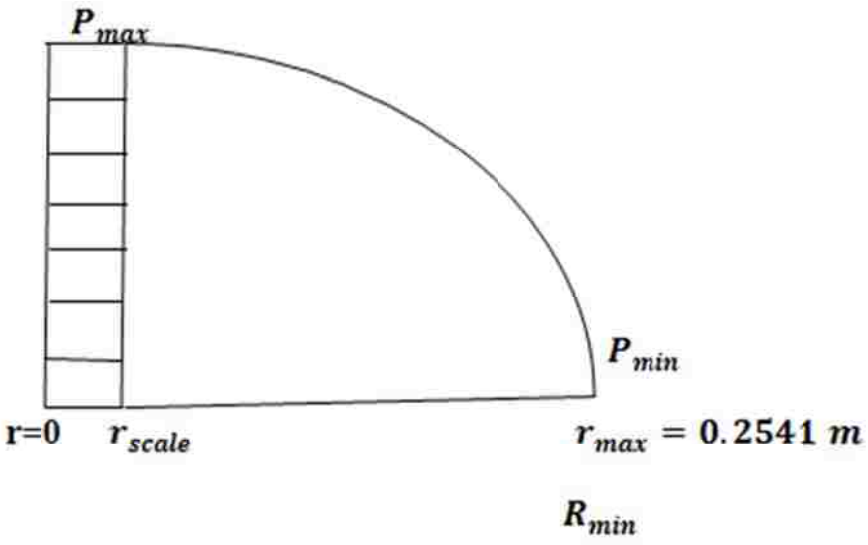


**Fig 7.10.** Pictorial representation of the parabolic profile for plasma flow parameters

Also, the coefficients will be calculated so that definite parabolic profile can be represented graphically for each of the plasma parameters. Concentrating on only the radial part of the plasma kinetic temperature, the strategy to find the coefficients of interest have been shown here. From Eqs. (7.15) and (7.16) it follows:

$$\left.\begin{aligned} \mathrm{K_{T,1}} + \mathrm{K_{T,2}} + \mathrm{K_{T,3}} &= R_{T,max} \\ \mathrm{K_{T,1}} * \mathrm{R_{min}^2} + \mathrm{K_{T,2}} * \mathrm{R_{min}} + \mathrm{K_{T,3}} &= R_{T,min} = Frac_T * R_{T,max} \end{aligned}\right\} \quad (7.17)$$

and the bulk flow parameters stay at the radial maximum value at $r = r_{scale}$, thus resulting in $\frac{dR_T(r)}{dr} = 0$.

Upon using this condition on Eq. (7.14), the following condition is obtained:

$$\mathrm{K_{T,1}} * \left(\frac{r_{scale}}{r}\right)^2 + \mathrm{K_{T,2}} * \left(\frac{r_{scale}}{r}\right) + \mathrm{K_{T,3}} = R_T(r)$$

$$\text{So, } \frac{dR_T(r)}{dr} = \mathrm{K_{T,1}} * r_{scale}^2 \left(\frac{-2}{r^3}\right) - \mathrm{K_{T,2}} * \left(\frac{r_{scale}}{r^2}\right)$$

$$\frac{\mathrm{d}R_T(r)}{\mathrm{dr}}(r = r_{scale}) = -\frac{2\mathrm{K_{T,1}}}{r_{scale}} - \frac{\mathrm{K_{T,2}}}{r_{scale}} = 0$$

$$\text{or, } \left(2\mathrm{K_{T,1}} + \mathrm{K_{T,2}}\right) = 0$$

$$\text{or, } \mathrm{K_{T,2}} = -2\mathrm{K_{T,1}}$$

By subtracting the second equation from the first one of Eq. (7.17), the following expression is obtained:

$$\mathrm{K_{T,1}} * (1 - R_{min}^2) - 2\mathrm{K_{T,1}} * (1 - R_{min}) = (1 - Frac_T) * R_{T,max} \ . \quad (7.18)$$

And using the value of $\mathrm{K_{T,2}}$ the following expression can be written:

$$\mathrm{K_{T,3}} - \mathrm{K_{T,1}} = R_{T,max} \ . \quad (7.19)$$

From Eqs. (7.18) and (7.19) expressions for the coefficients pertaining to the radial part of the plasma bulk temperature can be obtained:

$$\left.\begin{aligned} \mathrm{K_{T,1}} &= -\frac{R_{T,max}(1-Frac_T)}{(1-R_{min})^2} \\ \mathrm{K_{T,2}} &= \frac{2*R_{T,max}(1-Frac_T)}{(1-R_{min})^2} \\ \mathrm{K_{T,3}} &= R_{T,max}\left(1 - \frac{(1-Frac_T)}{(1-R_{min})^2}\right) \end{aligned}\right\} \quad (7.20)$$

(Coefficients for plasma temperature).

The mathematical expressions for the coefficients pertaining to the parabolic radial profiles of the other flow parameters of interest can be obtained by proceeding with very similar steps of formulation. The coefficients of interest are:

$$\left.\begin{aligned} \mathrm{K_{\rho,1}} &= -\frac{R_{\rho,max}(1-Frac_\rho)}{(1-R_{min})^2} \\ \mathrm{K_{\rho,2}} &= \frac{2*R_{\rho,max}(1-Frac_\rho)}{(1-R_{min})^2} \\ \mathrm{K_{\rho,3}} &= R_{\rho,max}\left(1 - \frac{(1-Frac_\rho)}{(1-R_{min})^2}\right) \end{aligned}\right\} \quad (7.21)$$

(Coefficients for plasma bulk density),

$$\left.\begin{aligned} \mathrm{K_{P,1}} &= -\frac{R_{P,max}(1-Frac_P)}{(1-R_{min})^2} \\ \mathrm{K_{P,2}} &= \frac{2*R_{P,max}(1-Frac_P)}{(1-R_{min})^2} \\ \mathrm{K_{P,3}} &= R_{P,max}\left(1 - \frac{(1-Frac_P)}{(1-R_{min})^2}\right) \end{aligned}\right\} \quad (7.22)$$

(Coefficients for plasma pressure),

$$\left.\begin{aligned} \mathrm{K_{v,1}} &= -\frac{R_{v,max}(1-Frac_v)}{(1-R_{min})^2} \\ \mathrm{K_{v,2}} &= \frac{2*R_{v,max}(1-Frac_v)}{(1-R_{min})^2} \\ \mathrm{K_{v,3}} &= R_{v,max}\left(1-\frac{(1-Frac_v)}{(1-R_{min})^2}\right) \end{aligned}\right\} \qquad (7.23)$$

(Coefficients for plasma bulk velocity).

Figures 7.11-7.14 display the surface plots of the plasma parameters as a function of the axial distance traversed as well as the radial stretch it reaches, as the high pressure jet coming out of the source capillary expands and evolves into the bigger volume.

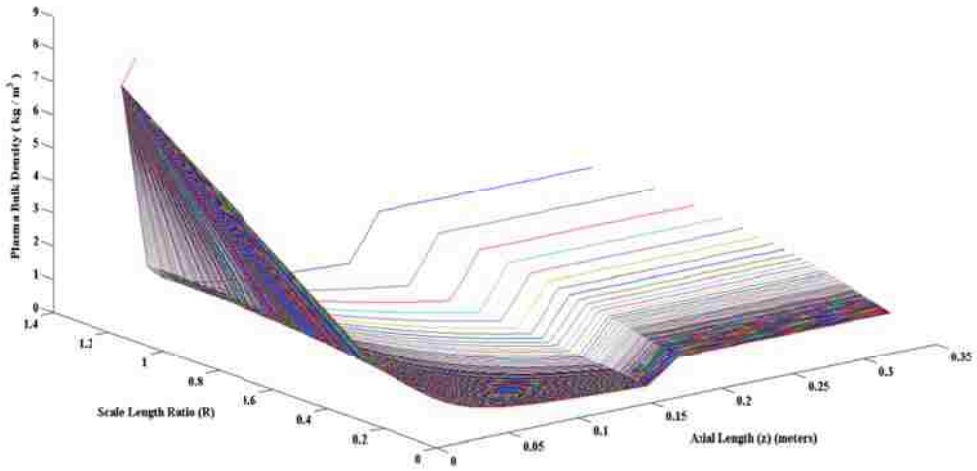


**Fig. 7.11** Two-dimensional profile for plasma bulk density in the throat and the expansion volume (parabolic model)

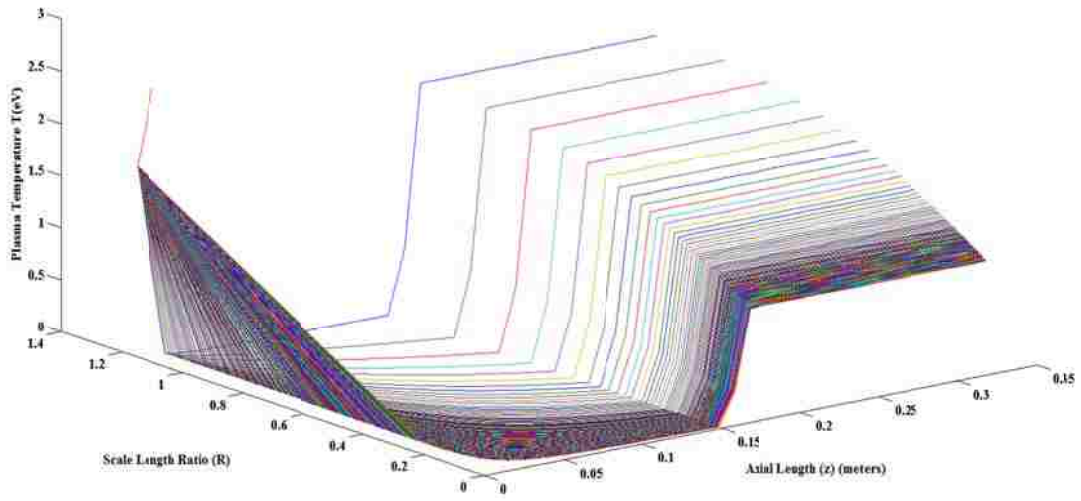


**Fig. 7.12** Two-dimensional profile for plasma temperature in the throat and the expansion volume (parabolic model)

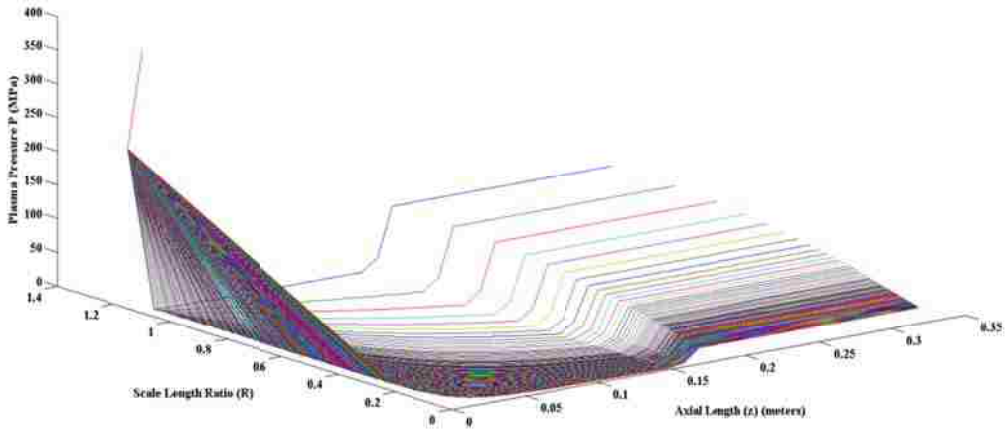


**Fig. 7.13** Two-dimensional profile for plasma pressure in the throat and the expansion volume (parabolic model)

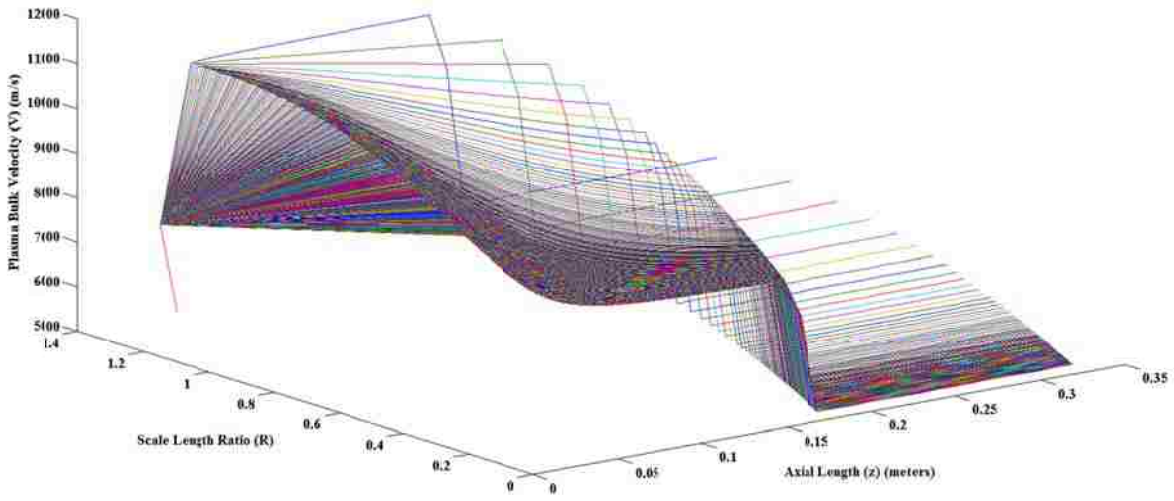


**Fig. 7.14** Two-dimensional profile for plasma velocity in the throat and the expansion volume (parabolic model)

## 7.6 Comparison and comments on the models

Looking at a cross-sectional slice one can clearly see that for the exponential model the bulk flow parameters remain fairly unchanged until a radial distance ~ R = 0.3 , and decreases thereafter towards the boundary with a quite sharp bend. This may be a possibility when there is an excessive hard disruption event that leads to the release of excessive amount of impurities along the axial direction, so that up to a certain radial distance the flow parameter profiles remain unaffected, the pronounced radial effects only being exhibited near the boundary. In case of power-law model, the plasma parameters start to decrease from the vicinity of $r_{scale}$ , i.e. R=1.0 and the radially decreasing nature propagates towards the boundary. The parabolic model predicts a reasonably unaffected radial profile until ~ R=0.80 and has a gradual fall thereafter.

The graphical characteristics of both the power-law and the parabolic models are quite similar as both of them show gradually decreasing radial profile, although the power-law may demonstrate a steep fall depending on the values of the parameters involved. However, the power-law and the parabolic profile can be applicable to the scenarios where the particulates gradually disperse inside the active volume of a fusion chamber. Thus it can roughly be said that radial profiles can be expected to follow somewhat exponential nature

when the plasma flows into a smaller expansion chamber, whereas other hard disruptions may lead more likely to a parabolic distribution where the chamber size ranges from medium to large.

However for the accurate prediction of aerosol evolution following a disruption event in a fusion reactor, there will be a need for enough off-axis data from experiments involving expansion barrels of uniform cross section. It is also useful to obtain data on the amount of the collected dust at different locations of the large chamber, which in turn gives an idea about the bulk transport. Depending on the requirement, and availability of the off-axis data, one can upgrade the models to an *adaptive weighted mixed model*, where it takes the original ordinate of an experimental point that represents the value of a flow parameter at a certain radial location in a cross-section, then the weights can be calculated. Values closer to experimental data will update the model to be closer to the experimental values. Assuming a particular scenario $d_2 > d_1$ this signifies that the experimental data is closer to the exponential model profile than the parabolic profile, then it is to assign the weights $W_1$ and $W_2$, such that:

$W_1 = \frac{d_2}{d_1+d_2}$ and $W_2 = \frac{d_1}{d_1+d_2}$.

And the tracking function of the bulk flow parameter might be formulates as follow:

$$F_{Track}(r,z) = Z(z) * (W_1 * R_{exponential}(r) + W_2 * R_{pararabolic}(r)) \quad (7.24)$$

This adds sophistication to the 2-D modeling. One added advantage of the mixed model is to introduce time-varying weights; this model would predict the temporal evolution reasonably accurate. Time-varying analytical model would need a check for the plasma parameters at each of the data-collection points at different locations, so for a very big virtual reactor chamber with large number of data collection array and very fine computational mesh, the algorithm may become computationally quite expensive.

## 7.7 References


[1] M. Bourham, J. Gilligan, O. Hankins, W. Eddy, J. Hurley, Electrothermal plasma source as a high heat flux simulator for plasma-facing components and launch technology studies , Proc. 9th International Conference on High Power Particle Beams, Washington, D.C., May 25-29 (1992), **Vol. III**, 1979-1983 (1992)

[2] J. Gilligan, M. Bourham, The use of an electrothermal plasma gun to simulate the extremely high heat flux conditions of a tokamak disruption, J. Fusion Energy, **12(3)**, 311-316 (1993)

[3] E. Y. Shcolnikov, A. V. Chebotarev, Y. A. Kulikov, A. V. Melnik, S. V. Volkov, High efficiency electrothermal accelerator, IEEE Trans. Magn., **31(1)**, 447–451(1995)

[4] T. Edamitsu, H. Tahara, Experimental and numerical study of an electrothermal pulsed plasma thruster for small satellites, *Vacuum*, **80(11/12)**, 1223–1228 (2006)

[5] J. D. Powell, A. E. Zielinski, Capillary discharge in the electrothermal gun," *IEEE Trans. Magn.*, **29(1)**, 591–595 (1993)

[6] J. D. Hurley, M. A. Bourham, J. G. Gilligan, Numerical simulation and experiment of plasma flow in the electrothermal launcher SIRENS, IEEE Transactions on Magnetics, **31(1)**, 616-620 (1995)

[7] E. Weiss, D. Zoler, S. Wald, E. Elias, Modeling of electrical confined-capillary-discharge where the discharge zone is extended by an additional pipe," Phys. Lett. A, 373(10), 972–975 (2009)

[8] **A.** L. Winfrey, J. G. Gilligan, A. V. Saveliev, M. Abd Al-Halim, M. A. Bourham, A study of plasma parameters in a capillary discharge with calculations using ideal and non-ideal plasma models for comparison with experiment, *IEEE Trans. Plasma Science*, **40(3)**, 843-852 (2012)

[9] R. Majumdar, J. G. Gilligan, A. L. Winfrey, M. A. Bourham**,** Supersonic flow patterns from electrothermal plasma source for simulated ablation and aerosol expansion following a fusion disruption, J. Fusion Energy, **33(1)**, 25-31 (2014)

[10] R. Majumdar, J. G. Gilligan, A. L. Winfrey, M. A. Bourham., Scaling laws of bulk plasma parameters for a 1-D flow through a capillary with extended converging-diverging nozzle for simulated expansion into fusion reactor chamber, J. Fusion Energy, **34(4)**, 905-910 (2015)

[11] R. Majumdar, M. A. Bourham, Effect of plasma temperature and nonlinearity of the Adiabatic Compressibility index on flow parameters for hypersonic aerosol expansion following a plasma disruption, J. Fusion Energy, Published Online 27 June, 2015, DOI: 10.1007/s10894-015-9960-1.

[12] John Philip Sharpe, Particulate generation during disruption simulation on the SIRENS high heat flux facility, PhD Dissertation, North Carolina State University, 2000

[13] J. P. Sharpe, B. J. Merrill, D. A. Petti, M. A. Bourham, J.G. Gilligan, Modeling of particulate production in the SIRENS plasma disruption simulator, *J. Nuclear Materials,* **290**, 1128-1133 (2001)

[14] Thomas J. Dolan, (Ed.), Magnetic fusion technology, Lecture notes in Energy 19, Springer Science and Business Media, p. 826, 2013

# Concluding Remarks

Supersonic flow patterns for simulated ablation and expansion following fusion disruption have been investigated, showing uniform aerosol expansion into the vacuum vessel

1-D steady state scaling laws for Bulk Flow Parameters were developed that predicts the flow parameters along the axis of the expansion chamber

A temperature –dependent non-linear compressibility index model has been developed for polycarbonate plasma ablated from an electrothermal capillary discharge

Characterized metal vapor plasma with temperature effects and non-linearity for selected metals as possible materials for PFCs in fusion reactors, and other devices.

2-D formulation of the evolution of arc- ablated plasma jet inside the expansion chamber has been developed and adaptive tracking functions have been prescribed.

# Future Work

Inclusion of the time-dependent flow in the 1-D supersonic flow patterns

Inclusion of recombination of plasma ions when plasma temperature drops down

Inclusion of material properties in the development of the scaling laws

Inclusion of the time-dependent flow in the 2-D formalism

# APPENDICES

# 8

# Appendices

## 8.1 Appendix A

**Note on geometry model:**

The selected geometry model of a converging-diverging throat was compared to a previous model proposed by Sharpe (2000), where he allowed a diverging section between the capillary exit and the vacuum chamber to computationally avoid shocking the flow. The following drawings compare the two geometries showing the extended transition region for each model and the geometry details.

**Capillary-extended Transition Region**

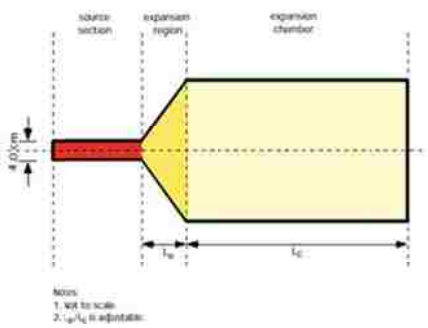


Previous geometry model
*"Phil Sharpe, 2000"*

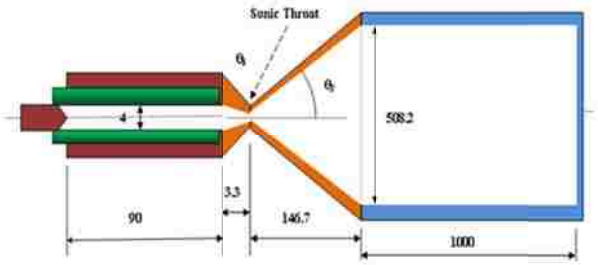


Current geometry model , 2013

**Schematic diagram of capillary discharge with attached transition and expansion regions**

[**N.B.** Dimensions are in **mm** (not to scale) ,$\theta_1 = 2°, \theta_2 = 60°$ ]

## Geometry Comparison

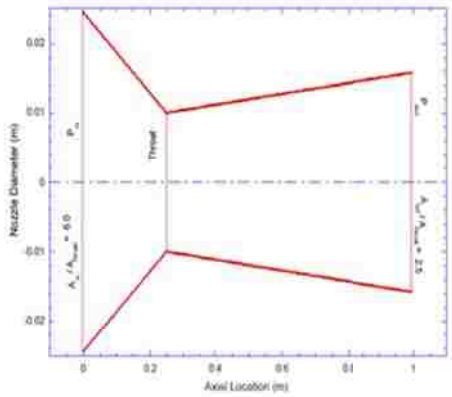


Phil Sharpe , 2000

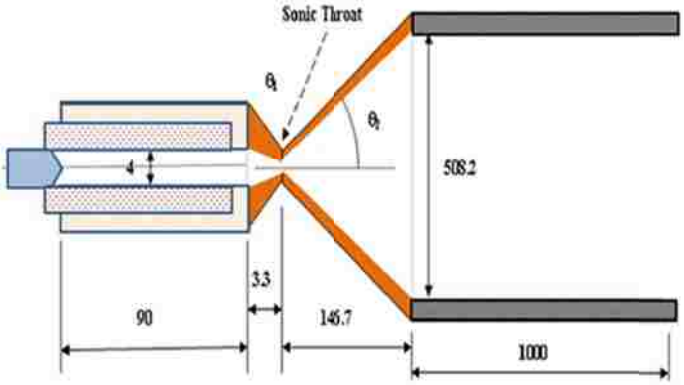


Current geometry, 2013

The Mach number along the axis shows similar results between the current model (right) and Sharpe's model (left) indicating a similar Mach number profiles.

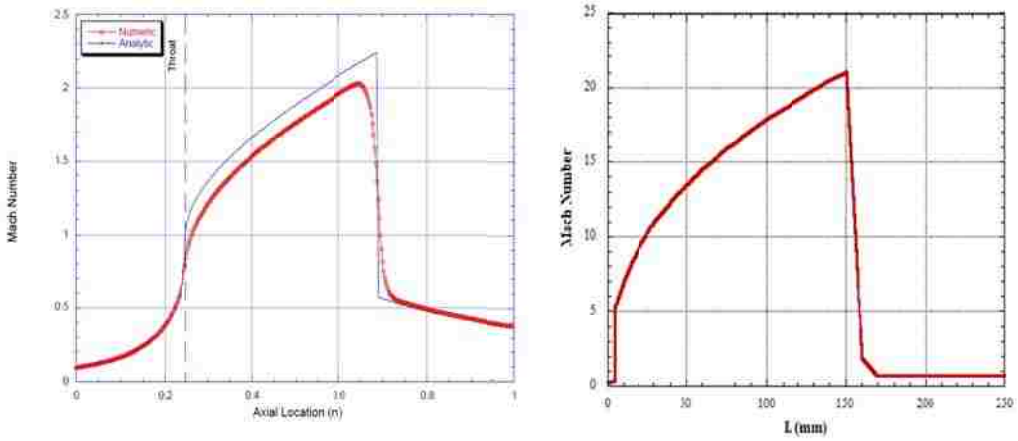


**Phil Sharpe , 2000**

Similarly, the plasma temperature along the axis is quite similar in both models as shown below.

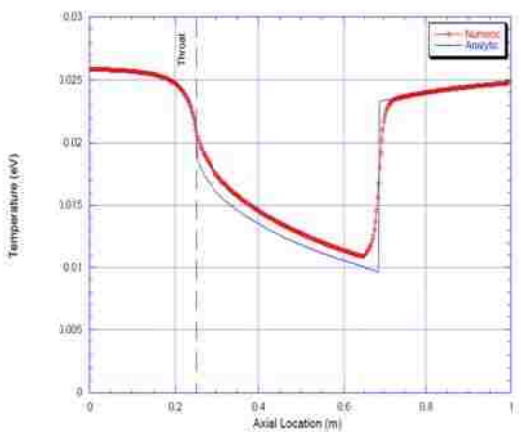


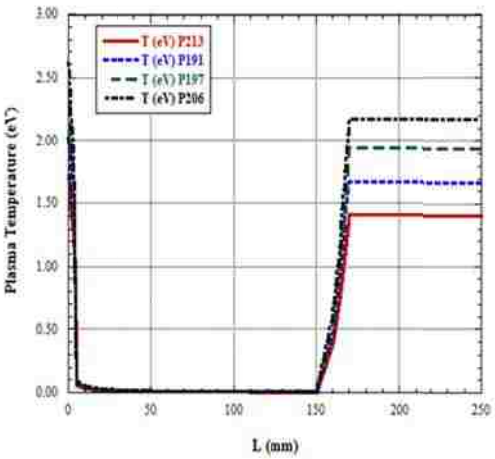


**Phil Sharpe , 2000**

Similarly, the plasma exit pressure along the axis is quite similar in both models as shown below.

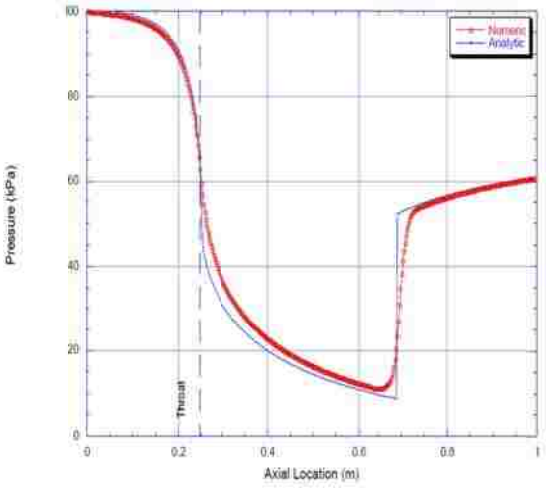


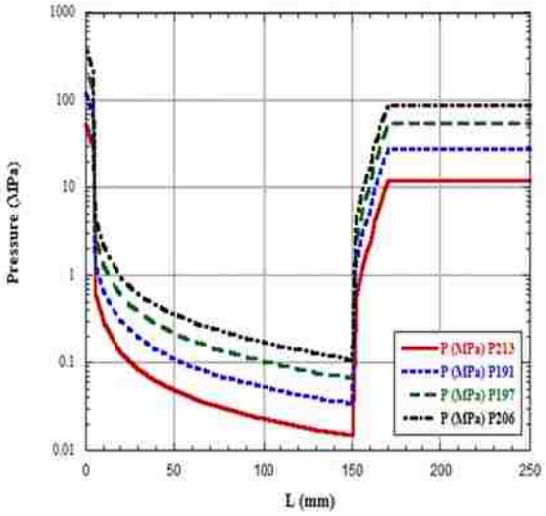


**Phil Sharpe, 2000**

## 8.2 Appendix B

### Codes for chapter 3:

### I. Routine for handling the Capillary-extended transition region

```
function [Q]=
Transition_Region_Model_paper1(Rho_noz_end,P_noz_end,V_noz_end,T_noz_end,r
_noz_end,Theta_sub,Theta_super)
% Terms with 'noz_end' suffix denote the respective capillary exit flow
parameter values
% Theta_sub is the angle of convergence in the converging section and
Theta_super is the angle of divergence in the diverging section

Gamma=3.8; % Adiabatic compressibility Index for the bulk plasma
L_tot=0.15;
a_noz_end=(Gamma*P_noz_end/Rho_noz_end)^0.5; % calculation of sonic speed
at the capillary exit
Mach_noz_end = V_noz_end/a_noz_end;
A_noz_end= pi*r_noz_end^2;
Numer=1+0.5*(Gamma-1)*Mach_noz_end^2;
Denom=0.5*(Gamma+1);
Expo=-(Gamma+1)/(2*(Gamma-1));
Fact=0.5*(Gamma-1);
A_crit = A_noz_end * Mach_noz_end*(Numer/Denom)^Expo;% calculation of
sonic throat area
r_crit=(A_crit/pi)^0.5;
Theta_sub_rad=(Theta_sub*pi)/180;
Theta_super_rad=(Theta_super*pi)/180;
H1=(r_noz_end - r_crit);
L1=H1/tan(Theta_sub_rad);
L_sub=0:0.0002:L1;
N=length(L_sub);
Mach_sub(1)=Mach_noz_end;
Rho(1)=Rho_noz_end;
P(1)=P_noz_end;
P_Mpa(1)=P(1)*1e-6;
T(1)=T_noz_end;
T_ev(1)=T(1)/11600;
V(1)=V_noz_end;
A_sub(1)=A_noz_end;
 for i=2:N
H(i)=(L1-L_sub(i))*tan(Theta_sub_rad);
D(i)=2*(H(i)+r_crit);
A_sub(i)=pi*D(i)^2/4;
F= A_sub(i)/A_crit;
if(F>=1 && F<1.34)
Mach_sub(i)= 1-0.88*(log(A_sub(i)/A_crit))^0.45;
elseif(F>=1.34)
Mach_sub(i)=(1+0.27*(A_sub(i)/A_crit)^-2)/(1.728*(A_sub(i)/A_crit));
end
end
L2=(L_tot-L1);
```

```
H2=L2*tan(Theta_super_rad);
L_super=L1:0.0002:L_tot;
M=length(L_super);
for i=1:M
H(i)=L_super(i)*tan(Theta_super_rad);
D(i)=2*(H(i)+r_crit);
A_super(i)=pi*D(i)^2/4;
F= A_super(i)/A_crit;
if(F>=1 && F<2.9)
Mach_super(i)= 1+1.2*(F-1)^0.5;
elseif(F>=2.9)
Mach_super(i)=(216*F - 254*F^0.6667)^0.2;
end
end
L=[L_sub(1:N) L_super(2:M)];
Mach=[Mach_sub(1:N) Mach_super(2:M)];
J=length(Mach);
for j=2:J
Rho(j)=Rho(j-1)*((1+ Fact*Mach(j-1)^2)/(1+ Fact*Mach(j)^2))^(1/(Gamma-1));
P(j)=P(j-1)*((1+ Fact*Mach(j-1)^2)/(1+ Fact*Mach(j)^2))^(Gamma/(Gamma-1));
T(j)=T(j-1)*((1+ Fact*Mach(j-1)^2)/(1+ Fact*Mach(j)^2));
P_Mpa(j)=P(j)*1e-6;
T_ev(j)=T(j)/11600;
end
for l=2:J
a(l)=(Gamma*P(l)/Rho(l))^0.5;
V(l)=Mach(l)*a(l);
end
% Array of area ratio
A=[A_sub(1:N) A_super(2:M)];
for q=1:J
G(q)= A(q)/A_crit;
end

% Loading of the Bulk Parameter values into respective arrays
Mach_Number=Mach(1:J);
P_Mpa=P_Mpa(1:J);
T_ev=T_ev(1:J);
Rho=Rho(1:J);
V=V(1:J);

% Loading of the Bulk Parameter values into Excel file
xlswrite('Transition_Region_Model_paper1.xls',Mach_Number(1:5:J),'Sheet1')
xlswrite('Transition_Region_Model_paper1.xls',P_Mpa(1:5:J),'Sheet2')
xlswrite('Transition_Region_Model_paper1.xls',T_ev(1:5:J),'Sheet3')
xlswrite('Transition_Region_Model_paper1.xls',Rho(1:5:J),'Sheet4')
xlswrite('Transition_Region_Model_paper1.xls',L(1:5:J),'Sheet5')
xlswrite('Transition_Region_Model_paper1.xls',V(1:5:J),'Sheet6')
xlswrite('Transition_Region_Model_paper1.xls',G(1:5:J),'Sheet7')

% plotting of the respective figures
figure(1)
plot(L(1:J),Mach(1:J),'k','linewidth',3)
figure(2)
plot(L(1:J),Rho(1:j),'r','linewidth',3)
```

```
figure(3)
plot(L(1:J),P_Mpa(1:J),'b','linewidth',3)
figure(4)
plot(L(1:J),V(1:J),'m','linewidth',3)
figure(5)
plot(L(1:J),T_ev(1:J),'c','linewidth',3)
```

## II. Sub-Routine for handling the shocks

```
function[R]=Shock_Parameter_analysis_NEW(Mach_end_point,Rho_end_point,T_ev
_end_point,P_MPa_end_point)
% we enter the diverging exit values of the flow bulk parameters as input
arguments
format long G
L=0:0.01:1;
N=length(L);

Theta_Sh=[30 36 42 55 65 75 85 90];% shock angles in degrees
T=length(Theta_Sh);

for l=1:T
Theta_Sh_rad(l)=Theta_Sh(l)*pi/180;% shock angles in radians
end

% We initialize the first elements of the respective arrays with diverging
exit values
Mach(1)=Mach_end_point;
T_ev(1)=T_ev_end_point;
P_Mpa(1)=P_MPa_end_point;
Rho(1)=Rho_end_point;

Gamma =3.8

   for i =1:N-1

    if(Mach(i)>=20)
        Shock= Theta_Sh_rad(1);
    elseif(Mach(i)>=16 && Mach(i)<20)
        Shock= Theta_Sh_rad(2);
    elseif(Mach(i)>=12 && Mach(i)<16)
        Shock= Theta_Sh_rad(3);
    elseif(Mach(i)>=9 && Mach(i)<12)
        Shock= Theta_Sh_rad(4);
    elseif(Mach(i)>=5.5 && Mach(i)<9)
        Shock= Theta_Sh_rad(5);
    elseif(Mach(i)>=3.0 && Mach(i)<5.5)
        Shock= Theta_Sh_rad(6);
    elseif(Mach(i)>=1.2 && Mach(i)< 3)
        Shock= Theta_Sh_rad(7);
    elseif(Mach(i)>0.8 && Mach(i)<1.2)
        Shock = Theta_Sh_rad(8);
    elseif( Mach(i)<=0.8)
        Mach(i+1)=Mach(i);
    i=i+1;
    end
```

```
  F=(sin(Shock))^2;
  store(i)=F;
    Nume=(Gamma+1)*Mach(i)^2;
    Denom=2*(Mach(i)^2*F -1);

    Deviation=acot(tan(Shock)*((Nume/Denom)-1));
    Angle_Diff=Shock - Deviation;

    D=(sin(Angle_Diff))^2;

Mach(i+1)= ((((Gamma-1)*Mach(i)^2*F + 2)/(2*Gamma*Mach(i)^2*F-(Gamma-
1)))/D)^0.5;
   end

for j =2:N
if (Mach(j-1)>=10)
    T_ev(j)=T_ev(j-1)*(2*Gamma*(Gamma-1)/(Gamma+1)^2)*Mach(j-1)^2*store(j-
1);
    Rho(j)=Rho(j-1)*(Gamma+1)/(Gamma-1);
    P_Mpa(j)=P_Mpa(j-1)*((2*Gamma)/(Gamma+1))*Mach(j-1)^2 *store(j-1);
elseif(Mach(j-1)>0.8 && Mach(j-1)<10)
T_ev(j)=T_ev(j-1)* ((Gamma-1)*Mach(j-1)^2*store(j-1) + 2)*(2*Gamma*Mach(j-
1)^2*store(j-1)-(Gamma-1))/((Gamma+1)^2 *Mach(j-1)^2 *store(j-1));
P_Mpa(j)=P_Mpa(j-1)*(2*Gamma*Mach(j-1)^2*store(j-1)-(Gamma-1))/(Gamma+1);
Rho(j)=Rho(j-1)*((Gamma+1)*Mach(j-1)^2*store(j-1))/((Gamma-1)*Mach(j-
1)^2*store(j-1) + 2);
elseif(Mach(j-1)<=0.8)
T_ev(j)=T_ev(j-1);
P_Mpa(j)=P_Mpa(j-1);
Rho(j)=Rho(j-1);
end
end

% Calculation of plasma bulk velocity
for j =1:N
a(j)=(Gamma*P_Mpa(j)*1e6/Rho(j))^0.5;
V(j)=Mach(j)*a(j);
end

% Loading of the Bulk Parameter values into respective output arrays
Mach_data=Mach(1:N)
T_ev_data=T_ev(1:N)
P_Mpa_data=P_Mpa(1:N)
Rho_data=Rho(1:N)
V_data=V(1:N)

% Plotting of the respective figures
figure(1)
plot(L(1:N),Mach(1:N),'k','linewidth',3)
figure(2)
plot(L(1:N),Rho(1:N),'r','linewidth',3)
figure(3)
plot(L(1:N),P_Mpa(1:N),'b','linewidth',3)
figure(4)
```

```
plot(L(1:N),V(1:N),'m','linewidth',3)
figure(5)
plot(L(1:N),T_ev(1:N),'c','linewidth',3)
```

## 8.3 Appendix C

### Codes for chapter 4:

### I. Routine for handling the One-dimensional scaling laws for flow bulk parameters

```
function[R]=Scaling_Law_Definition(Rho_noz_exit,T_noz_exit,P_noz_exit,Mach
_noz_exit,V_noz_exit,Z_sp)

% Terms with 'noz_exit' suffix denote the respective capillary exit flow
parameter values
% Z_sp gives us shock pitch length

Gamma=3.8;

Z_Trans=[0 0.0005 0.001 0.0015 0.002 0.0025 0.003 0.0033 0.004 0.005 0.01
0.015 0.02 0.025 0.03 0.035 0.04 0.045 0.05 0.055 0.06 0.065 0.07 0.075
0.08 0.085 0.09 0.095 0.1 0.11 0.12 0.13 0.14 0.15]; % Non-uniform axial
grid in transition region
N=length(Z_Trans);
Z_Ch=0.15:(Z_sp/4):0.25; % Uniform axial grid in expansion chamber

M=length(Z_Ch);
for i=1:N
if(Z_Trans(i)>=0 && Z_Trans(i)<=0.004)
T_Trans(i)=(T_noz_exit/2.627)*(2.627-246.0974*Z_Trans(i));
Rho_Trans(i)=(Rho_noz_exit/8.601)*(8.601-320.2329*Z_Trans(i));
P_Trans(i)=(P_noz_exit/386)*(386-46320*Z_Trans(i));
Mach_Trans(i)=(Mach_noz_exit/0.5397)*(0.5397+76.908*Z_Trans(i));
V_Trans(i)=(V_noz_exit/6160)*(6160+524633.51*Z_Trans(i));

elseif(Z_Trans(i)>0.004 && Z_Trans(i)<=0.15)
T_Trans(i)=(T_noz_exit/2.627)*0.0014*Z_Trans(i)^-0.802;
Rho_Trans(i)=(Rho_noz_exit/8.601)*0.60207*Z_Trans(i)^-0.273;
P_Trans(i)=(P_noz_exit/386)*0.01383*Z_Trans(i)^-1.089;
Mach_Trans(i)=45.317*Z_Trans(i)^0.4038;%% non-linear Mach part left as it
is
V_Trans(i)=(V_noz_exit/6160)*11773*Z_Trans(i)^0.0024;
end
end
T_DE=T_Trans(N);
Rho_DE=Rho_Trans(N);
P_DE=P_Trans(N);
```

```
Mach_DE=Mach_Trans(N);
V_DE=V_Trans(N);
T_s1=(T_noz_exit/2.627)*0.6090;
T_s2=(T_noz_exit/2.627)*2.1685;
Rho_s1=(Rho_noz_exit/8.601)*1.6769;
Rho_s2=(Rho_noz_exit/8.601)*2.397;
P_s1=(P_noz_exit/386)*17.4458;
P_s2=(P_noz_exit/386)*88.7856;



%% post shock Mach values will depend only on diverging exit value, so no
input-dependent scaling / modification for Mach
Mach_s1=1.9;
Mach_s2=0.7073;
V_s1=(V_noz_exit/6160)*10441.15;
V_s2=(V_noz_exit/6160)*7333.858;
m_T=(T_s1-T_DE)/Z_sp;
m_P=(P_s1-P_DE)/Z_sp;
m_Rho=(Rho_s1-Rho_DE)/Z_sp;
m_Mach=(Mach_s1-Mach_DE)/Z_sp;
m_V=(V_s1-V_DE)/Z_sp;
A_T=(T_s2-2*T_s1+T_DE)/(2*Z_sp^2);
B_T=(2*Z_sp*(T_s2-T_s1)-(T_s2-2*T_s1+T_DE)*(0.3+3*Z_sp))/(2*Z_sp^2);
C_T=T_DE-0.0225*A_T-0.15*B_T;
A_P=(P_s2-2*P_s1+P_DE)/(2*Z_sp^2);
B_P=(2*Z_sp*(P_s2-P_s1)-(P_s2-2*P_s1+P_DE)*(0.3+3*Z_sp))/(2*Z_sp^2);
C_P=P_DE-0.0225*A_P-0.15*B_P;
A_Rho=(Rho_s2-2*Rho_s1+Rho_DE)/(2*Z_sp^2);
B_Rho=(2*Z_sp*(Rho_s2-Rho_s1)-(Rho_s2-
2*Rho_s1+Rho_DE)*(0.3+3*Z_sp))/(2*Z_sp^2);
C_Rho=Rho_DE-0.0225*A_Rho-0.15*B_Rho;
A_Mach=0;
B_Mach=(Mach_s2-Mach_s1)/Z_sp;
C_Mach=Mach_s1-(0.15+Z_sp)*B_Mach;
A_V=(V_s2-2*V_s1+V_DE)/(2*Z_sp^2);
B_V=(2*Z_sp*(V_s2-V_s1)-(V_s2-2*V_s1+V_DE)*(0.3+3*Z_sp))/(2*Z_sp^2);
C_V=V_DE-0.0225*A_V-0.15*B_V;

for j=1:M
if(Z_Ch(j)>=0.15 && Z_Ch(j)<=0.15+Z_sp)
T_Ch(j)=(m_T*(Z_Ch(j)-0.15)+T_DE);
Rho_Ch(j)=(m_Rho*(Z_Ch(j)-0.15)+Rho_DE);
P_Ch(j)=(m_P*(Z_Ch(j)-0.15)+P_DE);
Mach_Ch(j)=(m_Mach*(Z_Ch(j)-0.15)+Mach_DE);
V_Ch(j)=(m_V*(Z_Ch(j)-0.15)+V_DE);

elseif(Z_Ch(j)>0.15+Z_sp && Z_Ch(j)<=0.15+2*Z_sp)
T_Ch(j)=(A_T*Z_Ch(j)^2+B_T*Z_Ch(j)+C_T);
Rho_Ch(j)=(A_Rho*Z_Ch(j)^2+B_Rho*Z_Ch(j)+C_Rho);
P_Ch(j)=(A_P*Z_Ch(j)^2+B_P*Z_Ch(j)+C_P);
Mach_Ch(j)=(A_Mach*Z_Ch(j)^2+B_Mach*Z_Ch(j)+C_Mach);
V_Ch(j)=(A_V*Z_Ch(j)^2+B_V*Z_Ch(j)+C_V);

%% steady-state values
```

```
elseif(Z_Ch(j)>0.15+2*Z_sp)
T_Ch(j)=T_s2;
Rho_Ch(j)=Rho_s2;
P_Ch(j)=P_s2;
Mach_Ch(j)=Mach_s2;
V_Ch(j)=V_s2;
end
end
% creation of continuous bulk flow parameter 1-D array
Z=[Z_Trans(1:N) Z_Ch(2:M)];
P_Mpa=[P_Trans(1:N) P_Ch(2:M)];
T_eV=[T_Trans(1:N) T_Ch(2:M)];
Rho=[Rho_Trans(1:N) Rho_Ch(2:M)];
V=[V_Trans(1:N) V_Ch(2:M)];
Mach=[Mach_Trans(1:N) Mach_Ch(2:M)];
J=length(Z);

%% Loading in Excel
% xlswrite('Scaling_Law.xlsx',Z(1:J),'Sheet1')
% xlswrite('Scaling_Law.xlsx',Mach(1:J),'Sheet2')
% xlswrite('Scaling_Law.xlsx',Rho(1:J),'Sheet3')
% xlswrite('Scaling_Law.xlsx',P_Mpa(1:J),'Sheet4')
% xlswrite('Scaling_Law.xlsx',V(1:J),'Sheet5')
% xlswrite('Scaling_Law.xlsx',T_eV(1:J),'Sheet6')

% Plotting of the respective figures
figure(1)
plot(Z(1:J),Mach(1:J),'k','linewidth',3)
hold on
figure(2)
plot(Z(1:J),Rho(1:J),'r','linewidth',3)
hold on
figure(3)
plot(Z(1:J),P_Mpa(1:J),'b','linewidth',3)
hold on
figure(4)
plot(Z(1:J),V(1:J),'m','linewidth',3)
hold on
figure(5)
plot(Z(1:J),T_eV(1:J),'c','linewidth',3)
hold on
```

## 8.4 Appendix D

### Codes for chapter 5:

### I. Routine for handling the temperature-affected 1-D flow in Capillary-extended transition region

```
function [Mach_Exit P_Mpa_Exit T_ev_Exit  Rho_Exit V_Exit]
=Refreshed_Transition_Region_Model_Gamma_Var1(Rho_noz_end,P_noz_end,V_noz_
end,T_noz_end,r_noz_end,Theta_sub,Theta_super, Categ, Non_Lin)

% Terms with 'noz_end' suffix denote the respective capillary exit flow
parameter values
% Theta_sub is the angle of convergence in the converging section and
Theta_super is the angle of divergence in the diverging section

format long G

Rho(1)=Rho_noz_end;
P(1)=P_noz_end;
P_Mpa(1)=P(1)*1e-6;
T(1)=T_noz_end;
T_ev(1)=T(1)/11600;
V(1)=V_noz_end;

[Gamma(1)] =Gamma_var_temp1(T_ev(1), Categ, Non_Lin);% Category chooses
model,and Non_lin chooses non-linearity

L_tot=0.15;
a_noz_end=(Gamma(1)*P(1)/Rho(1))^0.5;
Mach_noz_end = V_noz_end/a_noz_end;
Mach_sub(1)=Mach_noz_end;
A_noz_end= pi*r_noz_end^2;

Numer=1+0.5*(Gamma(1)-1)*Mach_noz_end^2;
Denom=0.5*(Gamma(1)+1);
Expo=-(Gamma(1)+1)/(2*(Gamma(1)-1));
Fact=0.5*(Gamma(1)-1);

 % Calculation of sonic throat area
A_crit = A_noz_end * Mach_noz_end*(Numer/Denom)^Expo;
r_crit=(A_crit/pi)^0.5;

Theta_sub_rad=(Theta_sub*pi)/180;
Theta_super_rad=(Theta_super*pi)/180;
H1=(r_noz_end - r_crit);
L1=H1/tan(Theta_sub_rad);

L_sub=0:0.0002:L1;
N=length(L_sub);
```

```
for i=2:N
    H(i)=(L1-L_sub(i))*tan(Theta_sub_rad);
    D(i)=2*(H(i)+r_crit);
    A(i)=pi*D(i)^2/4;
    F= A(i)/A_crit;
    if(F>=1 && F<1.34)
        Mach_sub(i)= 1-0.88*(log(A(i)/A_crit))^0.45;
    elseif(F>=1.34)
    Mach_sub(i)=(1+0.27*(A(i)/A_crit)^-2)/(1.728*(A(i)/A_crit));
    end
end

L2=(L_tot-L1);
H2=L2*tan(Theta_super_rad);
L_super=L1:0.0002:L_tot;
M=length(L_super);

for i=1:M
    H(i)=L_super(i)*tan(Theta_super_rad);
    D(i)=2*(H(i)+r_crit);
    A(i)=pi*D(i)^2/4;
    F= A(i)/A_crit;
    if(F>=1 && F<2.9)
        Mach_super(i)= 1+1.2*(F-1)^0.5;
    elseif(F>=2.9)
        Mach_super(i)=(216*F - 254*F^0.6667)^0.2;
    end

end
L=[L_sub(1:N) L_super(2:M)];
Mach=[Mach_sub(1:N) Mach_super(2:M)];
J=length(Mach);

for j=2:J
      Numer(j-1)=1+0.5*(Gamma(j-1)-1)*Mach(j-1)^2;
      Denom(j-1)=0.5*(Gamma(j-1)+1);
      Expo(j-1)=-(Gamma(j-1)+1)/(2*(Gamma(j-1)-1));
      Fact(j-1)=0.5*(Gamma(j-1)-1);
      T(j)=T(j-1)*((1+ Fact(j-1)*Mach(j-1)^2)/(1+ Fact(j-1)*Mach(j)^2));
      T_ev(j)=T(j)/11600;
    Gamma(j) =Gamma_var_temp1(T_ev(j), Categ, Non_Lin);% category chooses
model,and Non_lin chooses non-linearity
    Fact(j)=0.5*(Gamma(j)-1);
    Rho(j)=Rho(j-1)*((1+ Fact(j-1)*Mach(j-1)^2))^(1/(Gamma(j-1)-1))/((1+
Fact(j)*Mach(j)^2))^(1/(Gamma(j)-1));
    P(j)=P(j-1)*((1+ Fact(j-1)*Mach(j-1)^2))^(Gamma(j-1)/(Gamma(j-1)-
1))/((1+ Fact(j)*Mach(j)^2))^(Gamma(j)/(Gamma(j)-1));
    P_Mpa(j)=P(j)*1e-6;
   end

    for l=2:J
    a(l)=(Gamma(l)*P(l)/Rho(l))^0.5;
    V(l)=Mach(l)*a(l);
    end
```

```
Mach_Number=Mach(1:J);
P_Mpa=P_Mpa(1:J);
T_ev=T_ev(1:J);
Rho=Rho(1:J);
V=V(1:J);

%% Parameter Values at Diverging section Exit %%
Mach_Exit= Mach_Number(J);
P_Mpa_Exit=P_Mpa(J);
T_ev_Exit=T_ev(J);
Rho_Exit=Rho(J);
V_Exit=V(J);

%% Loading in Excel

xlswrite('Transition_Region_Paper2_Extra.xls',L(1:J),'Sheet1')
xlswrite('Transition_Region_Paper2_Extra.xls',Mach(1:J),'Sheet2')
xlswrite('Transition_Region_Paper2_Extra.xls',Rho(1:J),'Sheet3')
xlswrite('Transition_Region_Paper2_Extra.xls',P_Mpa(1:J),'Sheet4')
xlswrite('Transition_Region_Paper2_Extra.xls',V(1:J),'Sheet5')
xlswrite('Transition_Region_Paper2_Extra.xls',T_ev(1:J),'Sheet6')

%% Plots
% figure(1)
% plot(L(1:J),Mach(1:J),'k','linewidth',1)
% hold on
% figure(2)
% plot(L(1:J),Rho(1:J),'r','linewidth',1)
% hold on
% figure(3)
% plot(L(1:J),P_Mpa(1:J),'b','linewidth',1)
% hold on
% figure(4)
% plot(L(1:J),V(1:J),'m','linewidth',1)
% hold on
% figure(5)
% plot(L(1:J),T_ev(1:J),'c','linewidth',1)
% hold on
```

### *1.* Sub-Routine for handling the temperature –affected shocks

```
function[Mach_Exit P_Mpa_Exit T_ev_Exit  Rho_Exit
V_Exit]=Temperature_Affected_Shock_Model(Mach_end_point,Rho_end_point,T_ev
_end_point,P_MPa_end_point,Categ,Non_Lin)%% theta is entered in degrees
format long G
L=0:0.01:1;
N=length(L);
Mach(1)=Mach_end_point;
T_ev(1)=T_ev_end_point;
P_Mpa(1)=P_MPa_end_point;
Rho(1)=Rho_end_point;
[Gamma(1)] = Gamma_var_temp(T_ev(1), Categ, Non_Lin);% category chooses
model,and Non_lin chooses non-linearity

Theta_Sh=[30 36 42 55 65 75 85 90];%  shock angles in degrees
```

```
T=length(Theta_Sh);
 for l=1:T
Theta_Sh_rad(l)=Theta_Sh(l)*pi/180;%  shock angles in radians
end
  for j =1:N-1

    if(Mach(j)>=20)
        Shock= Theta_Sh_rad(1);
    elseif(Mach(j)>=16 && Mach(j)<20)
        Shock= Theta_Sh_rad(2);
    elseif(Mach(j)>=12 && Mach(j)<16)
        Shock= Theta_Sh_rad(3);
    elseif(Mach(j)>=9 && Mach(j)<12)
        Shock= Theta_Sh_rad(4);
    elseif(Mach(j)>=5.5 && Mach(j)<9)
        Shock= Theta_Sh_rad(5);
    elseif(Mach(j)>=3.0 && Mach(j)<5.5)
        Shock= Theta_Sh_rad(6);
    elseif(Mach(j)>=1.2 && Mach(j)< 3)
        Shock= Theta_Sh_rad(7);
    elseif(Mach(j)>0.8 && Mach(j)<1.2)
        Shock = Theta_Sh_rad(8);
    elseif( Mach(j)<=0.8)

% steady state values
 Mach(j+1)=Mach(j);
 T_ev(j+1)=T_ev(j);
 P_Mpa(j+1)=P_Mpa(j);
 Rho(j+1)=Rho(j);
 Gamma(j+1)=Gamma(j);
 j=j+1;
    end
  F=(sin(Shock))^2;
  store(j)=F;

    Nume=(Gamma(j)+1)*Mach(j)^2;
    Denom=2*(Mach(j)^2*F -1);
    Deviation=acot(tan(Shock)*((Nume/Denom)-1));
    Angle_Diff=Shock - Deviation;
    D=(sin(Angle_Diff))^2;

Mach(j+1)= ((((Gamma(j)-1)*Mach(j)^2*F + 2)/(2*Gamma(j)*Mach(j)^2*F-
(Gamma(j)-1)))/D)^0.5;

if (Mach(j)>=10)
    T_ev(j+1)=T_ev(j)*(2*Gamma(j)*(Gamma(j)-1)/(Gamma(j)+1)^2)*Mach(j)^2
*store(j);
    Rho(j+1)=Rho(j)*(Gamma(j)+1)/(Gamma(j)-1);
    P_Mpa(j+1)=P_Mpa(j)*((2*Gamma(j))/(Gamma(j)+1))*Mach(j)^2 *store(j);
    [Gamma(j+1)] =Gamma_var_temp(T_ev(j+1), Categ, Non_Lin);
elseif(Mach(j)>0.8 && Mach(j)<10)
T_ev(j+1)=T_ev(j)* ((Gamma(j)-1)*Mach(j)^2*store(j) +
2)*(2*Gamma(j)*Mach(j)^2*store(j)-(Gamma(j)-1))/((Gamma(j)+1)^2 *Mach(j)^2
*store(j));
```

```
P_Mpa(j+1)=P_Mpa(j)*(2*Gamma(j)*Mach(j)^2*store(j)-(Gamma(j)-
1))/(Gamma(j)+1);
Rho(j+1)=Rho(j)*((Gamma(j)+1)*Mach(j)^2*store(j))/((Gamma(j)-
1)*Mach(j)^2*store(j) + 2);
[Gamma(j+1)] =Gamma_var_temp(T_ev(j+1), Categ, Non_Lin); % function call
for gamma
end

 end
for j =1:N
a(j)=(Gamma(j)*P_Mpa(j)*1e6/Rho(j))^0.5;
V(j)=Mach(j)*a(j);
end

Mach_data=Mach(1:N);
T_ev_data=T_ev(1:N);
P_Mpa_data=P_Mpa(1:N);
Rho_data=Rho(1:N);
V_data=V(1:N);

%% Parameter Values at Subsonic Steady state %%
Mach_Exit= Mach_data(N);
P_Mpa_Exit=P_Mpa_data(N);
T_ev_Exit=T_ev_data(N);
Rho_Exit=Rho_data(N);
V_Exit=V_data(N);

%% Loading in Excel

xlswrite('Shock_BigChamber_Paper2.xls',L(1:N),'Sheet1')
xlswrite('Shock_BigChamber_Paper2.xls',Mach(1:N),'Sheet2')
xlswrite('Shock_BigChamber_Paper2.xls',Rho(1:N),'Sheet3')
xlswrite('Shock_BigChamber_Paper2.xls',P_Mpa(1:N),'Sheet4')
xlswrite('Shock_BigChamber_Paper2.xls',V(1:N),'Sheet5')
xlswrite('Shock_BigChamber_Paper2.xls',T_ev(1:N),'Sheet6')

% Plots
% figure(1)
% plot(L(1:N),Mach(1:N),'k','linewidth',1)
% hold on
% figure(2)
% plot(L(1:N),Rho(1:N),'r','linewidth',1)
% hold on
% figure(3)
% plot(L(1:N),P_Mpa(1:N),'b','linewidth',1)
% hold on
% figure(4)
% plot(L(1:N),V(1:N),'m','linewidth',1)
% hold on
% figure(5)
% plot(L(1:N),T_ev(1:N),'c','linewidth',1)
% hold on
```

## II. Temperature-affected Adiabatic Compressibility index (gamma)

```
function [Gamma] = Gamma_var_temp1(T, Categ, Non_Lin)

switch (Categ)

    case{1}
        switch (Non_Lin)
            case {1}
                a1=1;
                a2=0.1;
                b1=1;
                b2=0.1;
                c1=1;
                c2=0.1;
                d=1.2;
                flush1 =4.1305;
                flush2=4.48903;
            case{2}
                a1=1;
                a2=0.3;
                b1=1;
                b2=0.3;
                c1=1;
                c2=0.3;
                d=0.8;
                flush1 =2.81;
                flush2 =4.2384;
            case{3}
               a1=1;
                a2=0.9;
                b1=1;
                b2=0.9;
                c1=1;
                c2=0.9;
                d=1.8;
                flush1 =1.862;
                flush2 =4.67531;
            case{4}
               a1=1;
                a2=1;
                b1=1;
                b2=1;
                c1=1;
                c2=1;
                d=1;
                flush1 =1.4283;
                flush2=4.45842;

            otherwise
                display('No further option is available');
        end
```

```
   E_CO=11.109 ;%in eV
   E_CO2=5.451;% in eV
   E_CH=4.48;% in eV

   if(T<0.03)
       Gamma =flush1;
   elseif(T>=0.03 && T<=10)% temperature taken in eV
Denom = (a1*(E_CO2/T)^a2 + b1*(E_CO/T)^b2+c1*(E_CH/T)^c2);
Z_eff= 6.6449 * T^0.0825;
r=1.4+ 0.15*(Denom /((1+Z_eff)^d));
Gamma=1.35/(1-(1/r));

   elseif(T>10)
       Gamma =flush2;
   end

case{2}
    switch (Non_Lin)

       case{1}
            a1=1;
            a2=0.01;
            b1=1;
            b2=0.01;
            c1=1;
            c2=0.01;
            d1=4;
            d2=0.7;
            flush1 =4.4323;
            flush2=4.7492;

       case{2}
            a1=1;
            a2=0.2;
            b1=1;
            b2=0.2;
            c1=1;
            c2=0.2;
            d1=3;
            d2=0.8;
            flush1 =3.2;
            flush2 =4.7547;

       case{3}
            a1=1;
            a2=0.25;
            b1=1;
            b2=0.25;
            c1=1;
            c2=0.25;
            d1=4;
            d2=0.3;
            flush1 =2.4612;
            flush2=4.1027;
```

```
            case{4}
                a1=1;
                a2=1.1;
                b1=1;
                b2=1.1;
                c1=1;
                c2=1.1;
                d1=4;
                d2=2.5;
                flush1 =1.7729;
                flush2=5.8262;
            otherwise
                display('No further option is available');
            end

        E_CO=11.109 ;%in eV
        E_CO2=5.451;% in eV
        E_CH=4.48;% in eV
        if(T<0.03)
            Gamma =flush1;
        elseif(T>=0.03 && T<=10)
      Denom = (a1*(E_CO2/T)^a2 + b1*(E_CO/T)^b2+c1*(E_CH/T)^c2);
      Z_eff= 6.6449 * T^0.0825;
      r=1.3 + 0.6*(Denom /((1+ d1*Z_eff^d2)));
      Gamma=1.35/(1-(1/r));

        elseif(T>10)
            Gamma =flush2;
        end
end
```

## 8.5 Appendix E

### Codes for chapter 6:

### I. Routine for handling the temperature-affected Metal-Vapor plasma flow in Capillary-extended transition region

```
function [Mach_Exit P_Mpa_Exit T_ev_Exit  Rho_Exit V_Exit]
=Metal_Vapor_Transition_Region_Model_Gamma_Var(Rho_noz_end,P_noz_end,V_noz
_end,T_noz_end,r_noz_end,Theta_sub,Theta_super, Categ, Non_Lin, E_I1_eV,
E_I2_eV,E_Dim_eV,Z_I1,Z_I2)
format long G
E_I1=E_I1_eV;
E_I2=E_I2_eV;
E_Dim=E_Dim_eV;

Rho(1)=Rho_noz_end;
P(1)=P_noz_end;
P_Mpa(1)=P(1)*1e-6;
```

```
T(1)=T_noz_end;
T_ev(1)=T(1)/11600;
V(1)=V_noz_end;

[Gamma(1)] =Metal_Vapor_Gamma_var_temp(T_ev(1), Categ, Non_Lin, E_I1,
E_I2, E_Dim,Z_I1,Z_I2);% Category chooses model, and Non_lin chooses non-
linearity

L_tot=0.15;
a_noz_end=(Gamma(1)*P(1)/Rho(1))^0.5;
Mach_noz_end = V_noz_end/a_noz_end;
Mach_sub(1)=Mach_noz_end;
A_noz_end= pi*r_noz_end^2;

Numer=1+0.5*(Gamma(1)-1)*Mach_noz_end^2;
Denom=0.5*(Gamma(1)+1);
Expo=-(Gamma(1)+1)/(2*(Gamma(1)-1));
Fact=0.5*(Gamma(1)-1);

A_crit = A_noz_end * Mach_noz_end*(Numer/Denom)^Expo;
r_crit=(A_crit/pi)^0.5;



Theta_sub_rad=(Theta_sub*pi)/180;
Theta_super_rad=(Theta_super*pi)/180;
H1=(r_noz_end - r_crit);
L1=H1/tan(Theta_sub_rad);

L_sub=0:0.0002:L1;
N=length(L_sub);



for i=2:N
    H(i)=(L1-L_sub(i))*tan(Theta_sub_rad);
    D(i)=2*(H(i)+r_crit);
    A(i)=pi*D(i)^2/4;
    F= A(i)/A_crit;
    if(F>=1 && F<1.34)
        Mach_sub(i)= 1-0.88*(log(A(i)/A_crit))^0.45;
    elseif(F>=1.34)
        Mach_sub(i)=(1+0.27*(A(i)/A_crit)^-2)/(1.728*(A(i)/A_crit));
    end
end

L2=(L_tot-L1);
H2=L2*tan(Theta_super_rad);
L_super=L1:0.0002:L_tot;
M=length(L_super);

for i=1:M
    H(i)=L_super(i)*tan(Theta_super_rad);
    D(i)=2*(H(i)+r_crit);
```

```
    A(i)=pi*D(i)^2/4;
    F= A(i)/A_crit;
    if(F>=1 && F<2.9)
        Mach_super(i)= 1+1.2*(F-1)^0.5;
    elseif(F>=2.9)
        Mach_super(i)=(216*F - 254*F^0.6667)^0.2;
    end

end
L=[L_sub(1:N) L_super(2:M)];
Mach=[Mach_sub(1:N) Mach_super(2:M)];
J=length(Mach);

for j=2:J
    Numer(j-1)=1+0.5*(Gamma(j-1)-1)*Mach(j-1)^2;
Denom(j-1)=0.5*(Gamma(j-1)+1);
Expo(j-1)=-(Gamma(j-1)+1)/(2*(Gamma(j-1)-1));
Fact(j-1)=0.5*(Gamma(j-1)-1);
    T(j)=T(j-1)*((1+ Fact(j-1)*Mach(j-1)^2)/(1+ Fact(j-1)*Mach(j)^2));
    T_ev(j)=T(j)/11600;
    Gamma(j) =Metal_Vapor_Gamma_var_temp(T_ev(j), Categ, Non_Lin,E_I1,
E_I2,E_Dim,Z_I1,Z_I2);% category chooses model,and Non_lin chooses non-
linearity
    Fact(j)=0.5*(Gamma(j)-1);
    Rho(j)=Rho(j-1)*((1+ Fact(j-1)*Mach(j-1)^2))^(1/(Gamma(j-1)-1))/((1+
Fact(j)*Mach(j)^2))^(1/(Gamma(j)-1));
    P(j)=P(j-1)*((1+ Fact(j-1)*Mach(j-1)^2))^(Gamma(j-1)/(Gamma(j-1)-
1))/((1+ Fact(j)*Mach(j)^2))^(Gamma(j)/(Gamma(j)-1));
    P_Mpa(j)=P(j)*1e-6;
end

    for l=2:J
    a(l)=(Gamma(l)*P(l)/Rho(l))^0.5;
    V(l)=Mach(l)*a(l);
    end

Mach_Number=Mach(1:J);
P_Mpa=P_Mpa(1:J);
T_ev=T_ev(1:J);
Rho=Rho(1:J);
V=V(1:J);

%% Parameter Values at Diverging section Exit %%
Mach_Exit= Mach_Number(J);
P_Mpa_Exit=P_Mpa(J);
T_ev_Exit=T_ev(J);
Rho_Exit=Rho(J);
V_Exit=V(J);

%% Loading in Excel

xlswrite('Transition_Region_Metal_Vapor.xls',L(1:J),'Sheet1')
xlswrite('Transition_Region_Metal_Vapor.xls',Mach(1:J),'Sheet2')
xlswrite('Transition_Region_Metal_Vapor.xls',Rho(1:J),'Sheet3')
```

```
xlswrite('Transition_Region_Metal_Vapor.xls',P_Mpa(1:J),'Sheet4')
xlswrite('Transition_Region_Metal_Vapor.xls',V(1:J),'Sheet5')
xlswrite('Transition_Region_Metal_Vapor.xls',T_ev(1:J),'Sheet6')

%% Plots
% figure(1)
% plot(L(1:J),Mach(1:J),'k','linewidth',1)
% hold on
% figure(2)
% plot(L(1:J),Rho(1:J),'r','linewidth',1)
% hold on
% figure(3)
% plot(L(1:J),P_Mpa(1:J),'b','linewidth',1)
% hold on
% figure(4)
% plot(L(1:J),V(1:J),'m','linewidth',1)
% hold on
% figure(5)
% plot(L(1:J),T_ev(1:J),'c','linewidth',1)
% hold on
```

## II. Sub-Routine to handle the temperature affected shocks in Metal-vapor plasma 1-D flow

```
function[Mach_Exit P_Mpa_Exit T_ev_Exit  Rho_Exit V_Exit]
=Metal_Vapor_Plasma_Shock_Model(Mach_end_point,Rho_end_point,T_ev_end_poin
t,P_MPa_end_point,Categ,Non_Lin,E_I1_eV,E_I2_eV,E_Dim_eV,Z_I1,Z_I2)%%
theta is entered in degrees
format long G
E_I1=E_I1_eV;
E_I2=E_I2_eV;
E_Dim=E_Dim_eV;

L=0:0.01:1;
N=length(L);
Mach(1)=Mach_end_point;
T_ev(1)=T_ev_end_point;
P_Mpa(1)=P_MPa_end_point;
Rho(1)=Rho_end_point;
[Gamma(1)] = Metal_Vapor_Gamma_var_temp(T_ev(1), Categ,
Non_Lin,E_I1,E_I2,E_Dim,Z_I1,Z_I2);% category chooses model,and Non_lin
chooses non-linearity

Theta_Sh=[30 36 42 55 65 75 85 90];%%in degrees
T=length(Theta_Sh);
 for l=1:T
Theta_Sh_rad(l)=Theta_Sh(l)*pi/180;%%in radians
end

 for j =1:N-1
        if(Mach(j)>=20)
        Shock= Theta_Sh_rad(1);
        elseif(Mach(j)>=16 && Mach(j)<20)
```

```
        Shock= Theta_Sh_rad(2);
        elseif(Mach(j)>=12 && Mach(j)<16)
        Shock= Theta_Sh_rad(3);
        elseif(Mach(j)>=9 && Mach(j)<12)
        Shock= Theta_Sh_rad(4);
        elseif(Mach(j)>=5.5 && Mach(j)<9)
        Shock= Theta_Sh_rad(5);
        elseif(Mach(j)>=3.0 && Mach(j)<5.5)
        Shock= Theta_Sh_rad(6);
        elseif(Mach(j)>=1.2 && Mach(j)< 3)
        Shock= Theta_Sh_rad(7);
        elseif(Mach(j)>0.8 && Mach(j)<1.2)
        Shock = Theta_Sh_rad(8);
        elseif( Mach(j)<=0.8)
 Mach(j+1)=Mach(j);
 T_ev(j+1)=T_ev(j);
 P_Mpa(j+1)=P_Mpa(j);
 Rho(j+1)=Rho(j);
 Gamma(j+1)=Gamma(j);
 j=j+1;
  end
      F=(sin(Shock))^2;
  store(j)=F;

  Nume=(Gamma(j)+1)*Mach(j)^2;
    Denom=2*(Mach(j)^2*F -1);
    Deviation=acot(tan(Shock)*((Nume/Denom)-1));
    Angle_Diff=Shock - Deviation;
    D=(sin(Angle_Diff))^2;

Mach(j+1)= ((((Gamma(j)-1)*Mach(j)^2*F + 2)/(2*Gamma(j)*Mach(j)^2*F-
(Gamma(j)-1)))/D)^0.5;

if (Mach(j)>=10)
    T_ev(j+1)=T_ev(j)*(2*Gamma(j)*(Gamma(j)-1)/(Gamma(j)+1)^2)*Mach(j)^2
*store(j);
    Rho(j+1)=Rho(j)*(Gamma(j)+1)/(Gamma(j)-1);
    P_Mpa(j+1)=P_Mpa(j)*((2*Gamma(j))/(Gamma(j)+1))*Mach(j)^2 *store(j);
[Gamma(j+1)] =Metal_Vapor_Gamma_var_temp(T_ev(j+1), Categ, Non_Lin,E_I1,
E_I2,E_Dim,Z_I1,Z_I2);
elseif(Mach(j)>0.8 && Mach(j)<10)
T_ev(j+1)=T_ev(j)* ((Gamma(j)-1)*Mach(j)^2*store(j) +
2)*(2*Gamma(j)*Mach(j)^2*store(j)-(Gamma(j)-1))/((Gamma(j)+1)^2 *Mach(j)^2
*store(j));
P_Mpa(j+1)=P_Mpa(j)*(2*Gamma(j)*Mach(j)^2*store(j)-(Gamma(j)-
1))/(Gamma(j)+1);
Rho(j+1)=Rho(j)*((Gamma(j)+1)*Mach(j)^2*store(j))/((Gamma(j)-
1)*Mach(j)^2*store(j) + 2);
[Gamma(j+1)] =Metal_Vapor_Gamma_var_temp(T_ev(j+1), Categ,
Non_Lin,E_I1,E_I2,E_Dim,Z_I1,Z_I2);
end

 end
```

```
for j =1:N
a(j)=(Gamma(j)*P_Mpa(j)*1e6/Rho(j))^0.5;
V(j)=Mach(j)*a(j);
end


Mach_data=Mach(1:N);
T_ev_data=T_ev(1:N);
P_Mpa_data=P_Mpa(1:N);
Rho_data=Rho(1:N);
V_data=V(1:N);



%% Parameter Values at Subsonic Steady state %%
Mach_Exit= Mach_data(N);
P_Mpa_Exit=P_Mpa_data(N);
T_ev_Exit=T_ev_data(N);
Rho_Exit=Rho_data(N);
V_Exit=V_data(N);


 %% loading in Excel

xlswrite('Shock_BigChamber_Metal_Vapor.xls',L(1:N),'Sheet1')
xlswrite('Shock_BigChamber_Metal_Vapor.xls',Mach(1:N),'Sheet2')
xlswrite('Shock_BigChamber_Metal_Vapor.xls',Rho(1:N),'Sheet3')
xlswrite('Shock_BigChamber_Metal_Vapor.xls',P_Mpa(1:N),'Sheet4')
xlswrite('Shock_BigChamber_Metal_Vapor.xls',V(1:N),'Sheet5')
xlswrite('Shock_BigChamber_Metal_Vapor.xls',T_ev(1:N),'Sheet6')



% Plots
% figure(1)
% plot(L(1:N),Mach(1:N),'k','linewidth',1)
% hold on
% figure(2)
% plot(L(1:N),Rho(1:N),'r','linewidth',1)
% hold on
% figure(3)
% plot(L(1:N),P_Mpa(1:N),'b','linewidth',1)
% hold on
% figure(4)
% plot(L(1:N),V(1:N),'m','linewidth',1)
% hold on
% figure(5)
% plot(L(1:N),T_ev(1:N),'c','linewidth',1)

% hold on
```

### III. Temperature affected adiabatic compressibility index for Metal Vapor Bulk Plasma

```
function [Gamma] =Metal_Vapor_Gamma_var_temp(T, Categ, Non_Lin, E1, E2,
E3, Z1,Z2)
 % T has been taken in eV
switch (Categ)

    case{1}
        switch (Non_Lin)


            case {1}
                a1=1;
                a2=0.04;
                b1=1;
                b2=0.04;
                c1=1;
                c2=0.04;
                k1=0.9;
                k2=0.9;
                d=0.85;

            case{2}
                a1=1;
                a2=0.08;
                b1=1;
                b2=0.08;
                c1=1;
                c2=0.08;
                k1=0.2;
                k2=0.2;
                d=0.4;

            case{3}
               a1=1;
                a2=0.27;
                b1=1;
                b2=0.27;
                c1=1;
                c2=0.27;
                k1=0.7;
                k2=0.7;
                d=0.8;

            case{4}
                a1=1;
                a2=0.38;
                b1=1;
                b2=0.38;
                c1=1;
                c2=0.38;
                k1=0.8;
                k2=0.8;
```

```
                d=0.6;

            otherwise
                display('No further option is available');
        end

       E_I1=E1 ;%in eV
       E_I2=E2;% in eV
       E_Dim=E3;% in eV

      Denom_low = (a1*(E_I1/0.25)^a2 +
b1*(E_I2/0.25)^b2+c1*(E_Dim/0.25)^c2);
      Z_low=(Z1^k1+Z2^k2)^(1/(k1+k2));
      r_low=1.1+ 0.25*(Denom_low /((1+Z_low)^d));
      Gamma_low=1.53/(1-(1/r_low));
      flush1= Gamma_low;

      Denom_high = (a1*(E_I1/10)^a2 + b1*(E_I2/10)^b2+c1*(E_Dim/10)^c2);
      Z_high=(Z1^k1+Z2^k2)^(1/(k1+k2));
      r_high=1.1+ 0.25*(Denom_high /((1+Z_high)^d));
      Gamma_high=1.53/(1-(1/r_high));
      flush2= Gamma_high;


       if(T>=0.25 && T<=10)
    Denom = (a1*(E_I1/T)^a2 + b1*(E_I2/T)^b2+c1*(E_Dim/T)^c2);
      Z_eff=(Z1^k1+Z2^k2)^(1/(k1+k2));
      r=1.1+ 0.25*(Denom /((1+Z_eff)^d));
      Gamma=1.53/(1-(1/r));
       elseif(T<0.25)
           Gamma =flush1;

       elseif(T>10)
           Gamma =flush2;
       end

    case{2}
        switch (Non_Lin)

        case {1}
                a1=1;
                a2=0.15;
                b1=1;
                b2=0.15;
                c1=1;
                c2=0.15;
                r1=0.7;
                r2=0.3;
                s1=0.45;
                s2=0.45;

           case{2}
                a1=1;
```

```
                a2=0.16;
                b1=1;
                b2=0.16;
                c1=1;
                c2=0.16;
                r1=0.7;
                r2=0.3;
                s1=0.75;
                s2=0.75;

            case{3}
                a1=1;
                a2=0.17;
                b1=1;
                b2=0.17;
                c1=1;
                c2=0.17;
                r1=0.7;
                r2=0.3;
                s1=1.05;
                s2=1.05;

             case {4}
                a1=1;
                a2=0.3;
                b1=1;
                b2=0.3;
                c1=1;
                c2=0.3;
                r1=0.2;
                r2=0.2;
                s1=0.6;
                s2=0.8;

             otherwise
                display('No further option is available');
         end

       E_I1=E1 ;%in eV
       E_I2=E2;% in eV
       E_Dim=E3;% in eV

       F_low= (a1*(E_I1/0.25)^a2 +
b1*(E_I2/0.25)^b2+c1*(E_Dim/0.25)^c2)/(r1*Z1^s1+ r2*Z2^s2);
       r_low=1.2+ 0.15*F_low;
       Gamma_low=1.53/(1-(1/r_low));
       flush1= Gamma_low;

       F_high= (a1*(E_I1/10)^a2 +
b1*(E_I2/10)^b2+c1*(E_Dim/10)^c2)/(r1*Z1^s1+ r2*Z2^s2);
       r_high=1.2+ 0.15*F_high;
       Gamma_high=1.53/(1-(1/r_high));
       flush2= Gamma_high;
```

```
      if(T>=0.25 && T<=10)
   F = (a1*(E_I1/T)^a2 + b1*(E_I2/T)^b2+c1*(E_Dim/T)^c2)/(r1*Z1^s1+
r2*Z2^s2);
        r=1.2+ 0.15*F;
      Gamma=1.53/(1-(1/r));
     elseif(T<0.25)
           Gamma =flush1;

     elseif(T>10)
           Gamma =flush2;
     end
end
```

## 8.6 Appendix F

### Codes for chapter 7:

### I. Exponential model for 2D evolution of Lexan ablated plasma

```
function[Z  r  T_ev P_MPa Rho Vp Ma r_dyn R] =
Mission_2D_exponential_model(frac_T,frac_rho,r_scale,r_max,f,theta_sub_deg
,theta_super_deg,L2,T_ex,P_ex,Rho_ex,V_ex,Ma_ex)
format long G
%%  gamma=3.8; ( ** Just as a NOTE )

theta_sub_rad=theta_sub_deg*(pi/180);
theta_super_rad=theta_super_deg*(pi/180);

r_o=0.002;
r_e=0.2541;

Z_sub=[0  0.0005 0.001 0.0015 0.002 0.0025 0.003 0.0033];
%%Z_super=[0.005 0.01 0.015 0.02 0.025 0.03 0.035 0.04 0.045 0.05 0.055
0.06 0.065 0.07 0.075 0.08 0.085 0.09 0.095 0.1 0.11 0.12 0.13 0.14
0.1467];
Z_super=0.005:0.0005:0.1467;

Z_sp=0.01;% shock pitch length in meters
R_min=r_scale/r_max;

a1=-log(0.9)*(r_scale/r_o);
a2=-log(frac_T)*(R_min);

b1=-log(0.95)*(r_scale/r_o);
b2=-log(frac_rho)*(R_min);

c1=a1/2;
c2=a2/2;
```

```
 N=length(Z_sub);
for i=1:N
    r_sub(i)=r_o - Z_sub(i)*tan(theta_sub_rad);
end

M=length(Z_super);
for j=1:M
    r_super(j)=r_e -(L2- Z_super(j))*tan(theta_super_rad);
end

for j=1:M
 Z_mod(j)=Z_super(j)+0.0033;
end

Z_Chamber=0.15:(Z_sp):0.32;
C=length(Z_Chamber);

for c=1:C
r_Chamber(c)=r_super(M);
end

Z=[Z_sub(1:N) Z_mod(1:M) Z_Chamber(2:C)];
r=[r_sub(1:N) r_super(1:M) r_Chamber(2:C)];


%% DECLARATION Of POST-SHOCK VALUES %%
%%**********************************%%
T_s1=(T_ex/2.627)*0.6090;
T_s2=(T_ex/2.627)*2.1685;

P_s1=(P_ex/386)*17.4458;
P_s2=(P_ex/386)*88.7856;


Rho_s1=(Rho_ex/8.601)*1.6769;
Rho_s2=(Rho_ex/8.601)*2.397;


V_s1=(V_ex/6160)*10441.15;
V_s2=(V_ex/6160)*7333.858;


Ma_s1=1.9;
Ma_s2=0.7073;

%% CREATION Of SCALE_LENGTH RATIO: R %%
%%************************************%%

P=length(Z);
K=500;
for p=1:P
    for k=1:K
```

```
        if(r(p)<=0.002)
         r_dyn(p,k)=r(p);
         R(p,k)=(r_scale/(r_dyn(p,k)));
        elseif(r(p)>=0.002 )
        r_dyn(p,k)=0.002+((r(p)-0.002)/K)*(k-1);
        R(p,k)=(r_scale/(r_dyn(p,k)));
        end
    end
end

%% AXIAL PART %%
%%***************%%
for p=1:P
        if(Z(p)>=0 && Z(p)<=0.004)
                T_ev(p,1)=(T_ex/2.627)*(2.627 - 246.0974*Z(p));
                Rho(p,1)=(Rho_ex/8.601)*(8.601 - 320.2329*Z(p));
                P_MPa(p,1)=(P_ex/386)*(386 - 46320*Z(p));
                Vp(p,1)=(V_ex/6160)*(6160 + 524633.51*Z(p));
                Ma(p,1)=(Ma_ex/0.5397)*(0.5397+76.908*Z(p));

        elseif(Z(p)>0.004 && Z(p)<=0.15)

                 T_ev(p,1)=(T_ex/2.627)*0.0014*Z(p)^-0.802;
                 Rho(p,1)=(Rho_ex/8.601)*0.60207*Z(p)^-0.273;
                 P_MPa(p,1)=(P_ex/386)*0.01383*Z(p)^-1.089;
                 Vp(p,1)=(V_ex/6160)*11773*Z(p)^0.0024;
                 Ma(p,1)=45.317*Z(p)^0.4038;

        elseif(Z(p)>=0.15 && Z(p)<=(0.15+Z_sp))
                T_DE=T_ev(N+M-1,1);
                m_T=(T_s1-T_DE)/Z_sp;
                T_ev(p,1)=m_T*(Z(p)-0.15)+T_DE;

                Rho_DE=Rho(N+M-1,1);
                m_Rho=(Rho_s1-Rho_DE)/Z_sp;
                Rho(p,1)=m_Rho*(Z(p)-0.15)+Rho_DE;

                P_DE=P_MPa(N+M-1,1);
                m_P=(P_s1-P_DE)/Z_sp;
                P_MPa(p,1)=m_P*(Z(p)-0.15)+P_DE;

                V_DE=Vp(N+M-1,1);
                m_V=(V_s1-V_DE)/Z_sp;
                Vp(p,1)=m_V*(Z(p)-0.15)+V_DE;

                Ma_DE=Ma(N+M-1,1);
                m_Ma=(Ma_s1-Ma_DE)/Z_sp;
                Ma(p,1)=m_Ma*(Z(p)-0.15)+Ma_DE;

        elseif(Z(p)>=(0.15+Z_sp) && Z(p)<=(0.15+2*Z_sp))

           A_T=(T_s2-2*T_s1+T_DE)/(2*Z_sp^2);
B_T=(2*Z_sp*(T_s2-T_s1)-(T_s2-2*T_s1+T_DE)*(0.3+3*Z_sp))/(2*Z_sp^2);
```

```
            C_T=T_DE-0.0225*A_T-0.15*B_T;
            T_ev(p,1)=A_T*Z(p)^2+B_T*Z(p)+C_T;


          A_P=(P_s2-2*P_s1+P_DE)/(2*Z_sp^2);
B_P=(2*Z_sp*(P_s2-P_s1)-(P_s2-2*P_s1+P_DE)*(0.3+3*Z_sp))/(2*Z_sp^2);
          C_P=P_DE-0.0225*A_P-0.15*B_P;
          P_MPa(p,1)=A_P*Z(p)^2+B_P*Z(p)+C_P;

          A_Rho=(Rho_s2-2*Rho_s1+Rho_DE)/(2*Z_sp^2);
B_Rho=(2*Z_sp*(Rho_s2-Rho_s1)-(Rho_s2-2*Rho_s1+Rho_DE)*(0.3+3*Z_sp))/
(2*Z_sp^2);
          C_Rho=Rho_DE-0.0225*A_Rho-0.15*B_Rho;
          Rho(p,1)=A_Rho*Z(p)^2+B_Rho*Z(p)+C_Rho;

          A_V=(V_s2-2*V_s1+V_DE)/(2*Z_sp^2);
B_V=(2*Z_sp*(V_s2-V_s1)-(V_s2-2*V_s1+V_DE)*(0.3+3*Z_sp))/(2*Z_sp^2);
          C_V=V_DE-0.0225*A_V-0.15*B_V;
          Vp(p,1)=A_V*Z(p)^2+B_V*Z(p)+C_V;

          A_Ma=0;
          B_Ma=(Ma_s2-Ma_s1)/Z_sp;
          C_Ma=Mach_s1-(0.15+Z_sp)*B_Ma;
          Ma(p,1)=A_Ma*Z(p)^2+B_Ma*Z(p)+C_Ma;

        elseif(Z(p)>=(0.15+2*Z_sp))
            T_ev(p,1)=T_s2;
            P_MPa(p,1)=P_s2;
            Rho(p,1)=Rho_s2;
            Vp(p,1)=V_s2;
            Ma(p,1)=Ma_s2;
        end

end

%% RADIAL CORRECTION %%
%%********************%%
for p=1:P
    for k=2:K
        if(Z(p)>=0 && Z(p)<=0.004)
            if(R(p,k)>= f)
                T_ev(p,k)=T_ev(p,1);
                Rho(p,k)= Rho(p,1);
                P_MPa(p,k)=P_MPa(p,1);
                Vp(p,k)=Vp(p,1);
                Ma(p,k)=Ma(p,1);
            elseif(R(p,k)<f)
                T_ev(p,k)=exp(-a1/R(p,k))*T_ev(p,1);
                Rho(p,k)=exp(-b1/R(p,k))*Rho(p,1);
                P_MPa(p,k)=exp(-(a1+b1)/R(p,k))* P_MPa(p,1);
                Vp(p,k)=exp(-c1/R(p,k))*Vp(p,1);
                Ma(p,k)=Ma(p,1);
            end
        elseif(Z(p)>0.004 && Z(p)<=Z_Chamber(C))
```

```
            if(R(p,k)>=f)
                T_ev(p,k)=T_ev(p,1);
                Rho(p,k)= Rho(p,1);
                P_MPa(p,k)=P_MPa(p,1);
                Vp(p,k)=Vp(p,1);
                Ma(p,k)=Ma(p,1);
            elseif(R(p,k)<f)
                T_ev(p,k)=exp(-a2/R(p,k))*T_ev(p,1);
                Rho(p,k)=exp(-b2/R(p,k))*Rho(p,1);
                P_MPa(p,k)=exp(-(a2+b2)/R(p,k))* P_MPa(p,1);
                Vp(p,k)=exp(-c2/R(p,k))*Vp(p,1);
                Ma(p,k)=Ma(p,1);
            end

        end
    end
end
```

```
%% DATA WRITING To EXCEL FILE %%
%%*****************************%%
xlswrite('Mission_Exponential_2D.xlsx',Ma(1:P,1:K),'Sheet1')
xlswrite('Mission_Exponential_2D.xlsx',P_MPa(1:P,1:K),'Sheet2')
xlswrite('Mission_Exponential_2D.xlsx',T_ev(1:P,1:K),'Sheet3')
xlswrite('Mission_Exponential_2D.xlsx',Rho(1:P,1:K),'Sheet4')
xlswrite('Mission_Exponential_2D.xlsx',Vp(1:P,1:K),'Sheet5')
xlswrite('Mission_Exponential_2D.xlsx',r_dyn(1:P,1:K),'Sheet6')
xlswrite('Mission_Exponential_2D.xlsx',R(1:P,1:K),'Sheet7')

%% PLOTS %%
%%*******%%
% figure(1)
% plot3(Z(1:P),r_dyn(1:P,1:K),T_ev(1:P,1:K))
% figure(2)
% plot3(Z(1:P),r_dyn(1:P,1:K),Rho(1:P,1:K))
% figure(3)
% plot3(Z(1:P),r_dyn(1:P,1:K),P_MPa(1:P,1:K))
% figure(4)
% plot3(Z(1:P),r_dyn(1:P,1:K),Vp(1:P,1:K))
% figure(5)
% plot3(Z(1:P),r_dyn(1:P,1:K),Ma(1:P,1:K))

figure(1)
plot3(Z(1:P),R(1:P,1:K),T_ev(1:P,1:K))
figure(2)
plot3(Z(1:P),R(1:P,1:K),Rho(1:P,1:K))
figure(3)
plot3(Z(1:P),R(1:P,1:K),P_MPa(1:P,1:K))
figure(4)
plot3(Z(1:P),R(1:P,1:K),Vp(1:P,1:K))
figure(5)
```

```
plot3(Z(1:P),R(1:P,1:K),Ma(1:P,1:K))


% figure(1)
% plot(R(I,1:K),T_ev(I,1:K),'r')
% hold on
% figure(2)
% plot(R(I,1:K),Rho(I,1:K),'b')
% hold on
% figure(3)
% plot(R(I,1:K),P_MPa(I,1:K),'k')
% hold on
% figure(4)
% plot(R(I,1:K),Vp(I,1:K),'m')
% hold on
% figure(5)
% plot(R(I,1:K),Ma(I,1:K),'g')
% hold on
```

## II. Parabolic model for 2D evolution of Lexan ablated plasma

```
function[Z  r  T_ev P_MPa Rho Vp Ma r_dyn
R]=Mission_2D_parabolic_model(frac_T,frac_rho,r_scale,r_max,f,theta_sub_de
g,theta_super_deg,L2,T_ex,P_ex,Rho_ex,V_ex,Ma_ex)
format long G
%%  gamma=3.8; ( ** Just as a NOTE )
theta_sub_rad=theta_sub_deg*(pi/180);
theta_super_rad=theta_super_deg*(pi/180);

r_o=0.002;
r_e=0.2541;

Z_sub=[0  0.0005 0.001 0.0015 0.002 0.0025 0.003 0.0033];
Z_super=0.005:0.0005:0.1467;

Z_sp=0.01;% shock pitch length in meters
R_min=r_scale/r_max;

frac_P=frac_T*frac_rho;
frac_V=frac_T^0.5;

fact_T=(1-frac_T)/(1-R_min)^2;
fact_V=(1-frac_V)/(1-R_min)^2;
fact_rho=(1-frac_rho)/(1-R_min)^2;
fact_P=(1-frac_P)/(1-R_min)^2;

N=length(Z_sub);
for i=1:N
    r_sub(i)=r_o - Z_sub(i)*tan(theta_sub_rad);
end
```

```
M=length(Z_super);
for j=1:M
    r_super(j)=r_e -(L2- Z_super(j))*tan(theta_super_rad);
end

for j=1:M
 Z_mod(j)=Z_super(j)+0.0033;
end


Z_Chamber=0.15:(Z_sp):0.32;

C=length(Z_Chamber);

for c=1:C
r_Chamber(c)=r_super(M);
end

Z=[Z_sub(1:N) Z_mod(1:M) Z_Chamber(2:C)];
r=[r_sub(1:N) r_super(1:M) r_Chamber(2:C)];


%% DECLARATION Of POST-SHOCK VALUES %%
%%**********************************%%
T_s1=(T_ex/2.627)*0.6090;
T_s2=(T_ex/2.627)*2.1685;

P_s1=(P_ex/386)*17.4458;
P_s2=(P_ex/386)*88.7856;


Rho_s1=(Rho_ex/8.601)*1.6769;
Rho_s2=(Rho_ex/8.601)*2.397;


V_s1=(V_ex/6160)*10441.15;
V_s2=(V_ex/6160)*7333.858;


Ma_s1=1.9;
Ma_s2=0.7073;


%% CREATION Of SCALE_LENGTH RATIO : R %%
%%**********************************%%

P=length(Z);
K=500;
for p=1:P
    for k=1:K
        if(r(p)<=0.002)
```

```
         r_dyn(p,k)=r(p);
         R(p,k)=(r_scale/(r_dyn(p,k)));
        elseif(r(p)>=0.002 )
        r_dyn(p,k)=0.002+((r(p)-0.002)/K)*(k-1);
        R(p,k)=(r_scale/(r_dyn(p,k)));
        end
    end
end

%% AXIAL PART %%
%%**************%%
for p=1:P
        if(Z(p)>=0 && Z(p)<=0.004)

                T_ev(p,1)=(T_ex/2.627)*(2.627 - 246.0974*Z(p));
                Rho(p,1)=(Rho_ex/8.601)*(8.601 - 320.2329*Z(p));
                P_MPa(p,1)=(P_ex/386)*(386 - 46320*Z(p));
                Vp(p,1)=(V_ex/6160)*(6160 + 524633.51*Z(p));
                Ma(p,1)=(Ma_ex/0.5397)*(0.5397+76.908*Z(p));

        elseif(Z(p)>0.004 && Z(p)<=0.15)

                 T_ev(p,1)=(T_ex/2.627)*0.0014*Z(p)^-0.802;
                 Rho(p,1)=(Rho_ex/8.601)*0.60207*Z(p)^-0.273;
                 P_MPa(p,1)=(P_ex/386)*0.01383*Z(p)^-1.089;
                 Vp(p,1)=(V_ex/6160)*11773*Z(p)^0.0024;
                 Ma(p,1)=45.317*Z(p)^0.4038;

        elseif(Z(p)>0.15 && Z(p)<=(0.15+Z_sp))
                T_DE=T_ev(N+M-1,1);
                m_T=(T_s1-T_DE)/Z_sp;
                T_ev(p,1)=m_T*(Z(p)-0.15)+T_DE;

                Rho_DE=Rho(N+M-1,1);
                m_Rho=(Rho_s1-Rho_DE)/Z_sp;
                Rho(p,1)=m_Rho*(Z(p)-0.15)+Rho_DE;

                P_DE=P_MPa(N+M-1,1);
                m_P=(P_s1-P_DE)/Z_sp;
                P_MPa(p,1)=m_P*(Z(p)-0.15)+P_DE;
                V_DE=Vp(N+M-1,1);
                m_V=(V_s1-V_DE)/Z_sp;
                Vp(p,1)=m_V*(Z(p)-0.15)+V_DE;

                Ma_DE=Ma(N+M-1,1);
                m_Ma=(Ma_s1-Ma_DE)/Z_sp;
                Ma(p,1)=m_Ma*(Z(p)-0.15)+Ma_DE;

        elseif(Z(p)>(0.15+Z_sp) && Z(p)<=(0.15+2*Z_sp))

           A_T=(T_s2-2*T_s1+T_DE)/(2*Z_sp^2);
B_T=(2*Z_sp*(T_s2-T_s1)-(T_s2-2*T_s1+T_DE)*(0.3+3*Z_sp))/(2*Z_sp^2);
           C_T=T_DE-0.0225*A_T-0.15*B_T;
           T_ev(p,1)=A_T*Z(p)^2+B_T*Z(p)+C_T;
```

```
          A_P=(P_s2-2*P_s1+P_DE)/(2*Z_sp^2);
B_P=(2*Z_sp*(P_s2-P_s1)-(P_s2-2*P_s1+P_DE)*(0.3+3*Z_sp))/(2*Z_sp^2);
          C_P=P_DE-0.0225*A_P-0.15*B_P;
          P_MPa(p,1)=A_P*Z(p)^2+B_P*Z(p)+C_P;

          A_Rho=(Rho_s2-2*Rho_s1+Rho_DE)/(2*Z_sp^2);
B_Rho=(2*Z_sp*(Rho_s2-Rho_s1)-(Rho_s2-2*Rho_s1+Rho_DE)*(0.3+3*Z_sp))
/(2*Z_sp^2);
          C_Rho=Rho_DE-0.0225*A_Rho-0.15*B_Rho;
          Rho(p,1)=A_Rho*Z(p)^2+B_Rho*Z(p)+C_Rho;

          A_V=(V_s2-2*V_s1+V_DE)/(2*Z_sp^2);
   B_V=(2*Z_sp*(V_s2-V_s1)-(V_s2-2*V_s1+V_DE)*(0.3+3*Z_sp))/(2*Z_sp^2);
          C_V=V_DE-0.0225*A_V-0.15*B_V;
          Vp(p,1)=A_V*Z(p)^2+B_V*Z(p)+C_V;


          A_Ma=0;
          B_Ma=(Ma_s2-Ma_s1)/Z_sp;
          C_Ma=Ma_s1-(0.15+Z_sp)*B_Ma;
          Ma(p,1)=A_Ma*Z(p)^2+B_Ma*Z(p)+C_Ma;

       elseif(Z(p)>(0.15+2*Z_sp))
           T_ev(p,1)=T_s2;
           P_MPa(p,1)=P_s2;
           Rho(p,1)=Rho_s2;
           Vp(p,1)=V_s2;
           Ma(p,1)=Ma_s2;
       end

end

 %% RADIAL CORRECTION %%
%%********************%%
for p=1:P
    for k=2:K
          if(Z(p)>=0 && Z(p)<=Z_Chamber(C))
            if(R(p,k)>=f)
               T_ev(p,k)=T_ev(p,1);
               Rho(p,k)= Rho(p,1);
               P_MPa(p,k)=P_MPa(p,1);
               Vp(p,k)=Vp(p,1);
               Ma(p,k)=Ma(p,1);
           elseif(R(p,k)<f)
               a_T=-fact_T;
               b_T=2*fact_T;
               c_T=(1-fact_T);
               T_ev(p,k)=(a_T*R(p,k)^2+ b_T*R(p,k)+ c_T)*T_ev(p,1);

               a_rho=-fact_rho;
               b_rho=2*fact_rho;
               c_rho=(1-fact_rho);
```

```
                Rho(p,k)=(a_rho*R(p,k)^2+ b_rho*R(p,k)+ c_rho)*Rho(p,1);

                a_P=-fact_P;
                b_P=2*fact_P;
                c_P=(1-fact_P);
                P_MPa(p,k)=(a_P*R(p,k)^2+ b_P*R(p,k)+ c_P)* P_MPa(p,1);

                a_V=-fact_V;
                b_V=2*fact_V;
                c_V=(1-fact_V);
                Vp(p,k)=(a_V*R(p,k)^2+ b_V*R(p,k)+ c_V)*Vp(p,1);


                Ma(p,k)=Ma(p,1);
            end

        end
    end
end

%% DATA WRITING To EXCEL FILE %%
%%*****************************%%
% xlswrite('Parabolic_2D.xlsx',Ma(1:P,1:K),'Sheet1')
% xlswrite('Parabolic_2D.xlsx',P_MPa(1:P,1:K),'Sheet2')
% xlswrite('Parabolic_2D.xlsx',T_ev(1:P,1:K),'Sheet3')
% xlswrite('Parabolic_2D.xlsx',Rho(1:P,1:K),'Sheet4')
% xlswrite('Parabolic_2D.xlsx',Vp(1:P,1:K),'Sheet5')
% xlswrite('Parabolic_2D.xlsx',r_dyn(1:P,1:K),'Sheet6')
% xlswrite('Parabolic_2D.xlsx',R(1:P,1:K),'Sheet7')
%% PLOTS %%
%%*******%%
% figure(1)
% plot3(Z(1:P),r_dyn(1:P,1:K),T_ev(1:P,1:K))
% figure(2)
% plot3(Z(1:P),r_dyn(1:P,1:K),Rho(1:P,1:K))
% figure(3)
% plot3(Z(1:P),r_dyn(1:P,1:K),P_MPa(1:P,1:K))
% figure(4)
% plot3(Z(1:P),r_dyn(1:P,1:K),Vp(1:P,1:K))
% figure(5)
% plot3(Z(1:P),r_dyn(1:P,1:K),Ma(1:P,1:K))

figure(1)
plot3(Z(1:P),R(1:P,1:K),T_ev(1:P,1:K))
figure(2)
plot3(Z(1:P),R(1:P,1:K),Rho(1:P,1:K))
figure(3)
plot3(Z(1:P),R(1:P,1:K),P_MPa(1:P,1:K))
figure(4)
plot3(Z(1:P),R(1:P,1:K),Vp(1:P,1:K))
figure(5)
plot3(Z(1:P),R(1:P,1:K),Ma(1:P,1:K))

% figure(1)
```

```
% plot(R(I,1:K),T_ev(I,1:K),'r')
% hold on
% figure(2)
% plot(R(I,1:K),Rho(I,1:K),'b')
% hold on
% figure(3)
% plot(R(I,1:K),P_MPa(I,1:K),'k')
% hold on
% figure(4)
% plot(R(I,1:K),Vp(I,1:K),'m')
% hold on
% figure(5)
% plot(R(I,1:K),Ma(I,1:K),'g')
% hold on
```